Interacting Neutral Atoms in a Scalable Platform of Optical Tweezers for Quantum Computation and Sensing

Wechselwirkende neutrale Atome in einer skalierbaren Plattform aus optischen Pinzetten für Quanteninformationsverarbeitung und Quantensensorik

Zur Erlangung des Grades eines Doktors der Naturwissenschaften (Dr. rer. nat.)
Genehmigte Dissertation von Dominik Schäffner aus Worms
Tag der Einreichung: 11. Mai 2021, Tag der Prüfung: 31. Mai 2021

1. Gutachten: Prof. Dr. Gerhard Birkl
2. Gutachten: Prof. Dr. Thomas Walther
Darmstadt – D 17

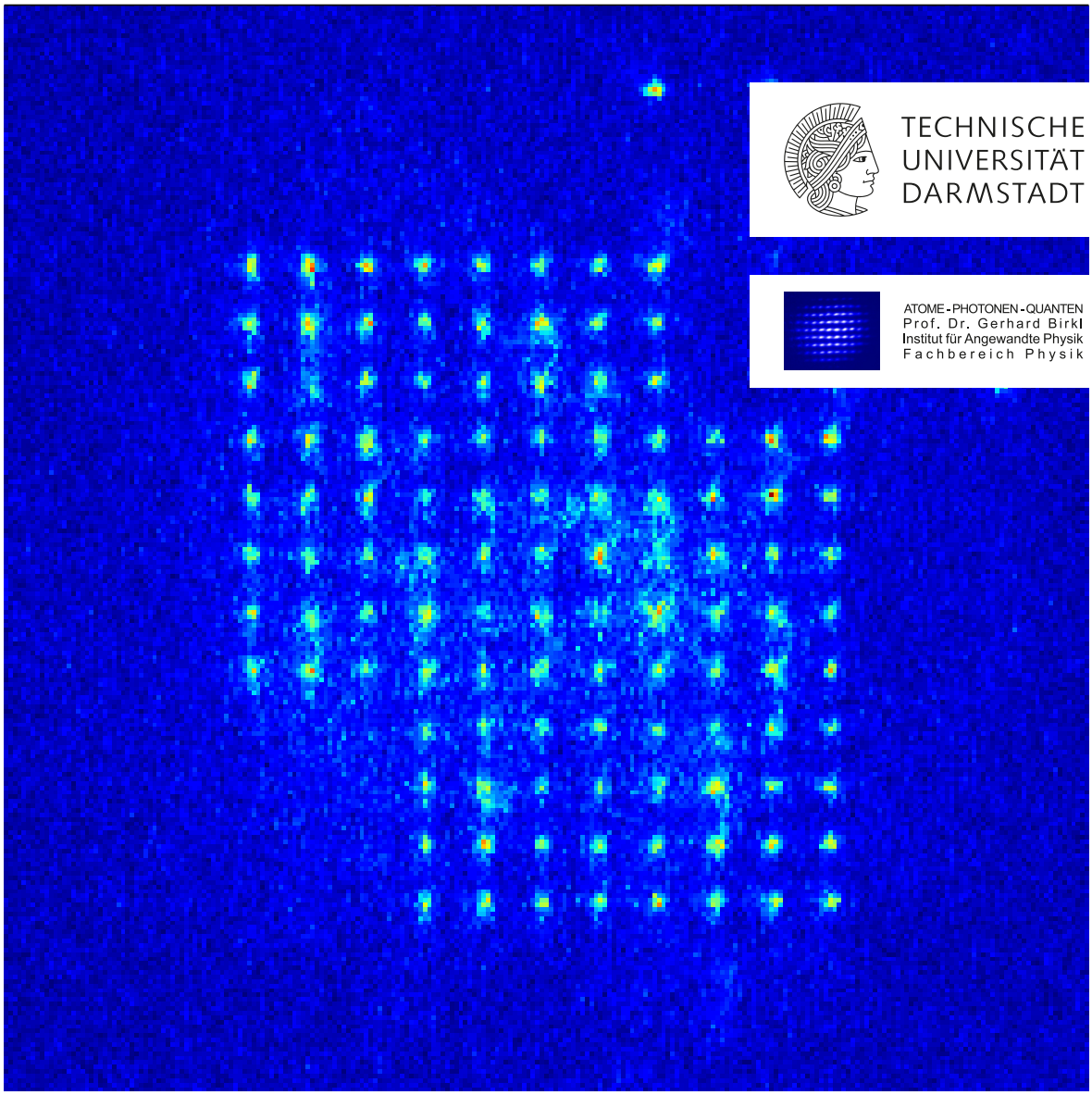

Interacting Neutral Atoms in a Scalable Platform of Optical Tweezers for Quantum Computation and Sensing
Wechselwirkende neutrale Atome in einer skalierbaren Plattform aus optischen Pinzetten für Quanteninformationsverarbeitung und Quantensensorik

Accepted doctoral thesis by Dominik Schäffner

1. Review: Prof. Dr. Gerhard Birkl
2. Review: Prof. Dr. Thomas Walther

Date of submission: 11 May 2021
Date of thesis defense: 31 May 2021

Darmstadt – D 17

Cover picture:
Fluorescence image of 111 individual rubidium atoms arranged in a predefined defect-free configuration within the two-dimensional tweezer array presented in this thesis.

Bitte zitieren Sie dieses Dokument als:
URN: urn:nbn:de:tuda-tuprints-203442
URL: http://tuprints.ulb.tu-darmstadt.de/20344

Dieses Dokument wird bereitgestellt von tuprints,
E-Publishing-Service der TU Darmstadt
http://tuprints.ulb.tu-darmstadt.de
tuprints@ulb.tu-darmstadt.de

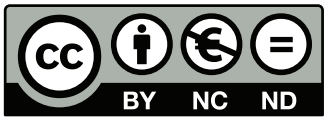

Abstract

Arrays of optical tweezers provide a versatile environment to store neutral-atom quantum systems with precise control over their internal and external degrees of freedom. These configurations offer a wide range of applications in a variety of research fields including quantum computation and simulation, quantum many-body physics, and quantum sensing. The micro-optical platform presented in this work provides a large-scale tweezer array comprising hundreds of focused-beam dipole potentials with diffraction-limited waists of $1.45(10)\,\mu\text{m}$. Exploiting light-assisted collisions allows for preparation of $191(17)$ individual laser-cooled rubidium atoms into a typical number of 361 sites of a quadratic-grid array with trap depths corresponding to temperatures in the millikelvin regime.
In the context of this thesis, a technique was implemented to transform an arbitrary distribution of atoms within the array into a predefined pattern via sequential transport between sites. Surpassing the stochastic loading process, this allows to commence experiments from a well-defined initial configuration, compensate for atom loss during an experimental cycle, and decrease the necessary number of time-consuming laser cooling phases. Based on this approach, defect-free configurations consisting of up to 111 atoms could be demonstrated. This paved the way to conduct experiments which have been impossible to carry out before within a reasonable amount of time.
Significant progress has been made towards the realization of two-qubit operations in this experimental platform. Site-selective coherent coupling from the $5S_{1/2}$ ground to a $82S_{1/2}$ Rydberg state via a two-photon process was implemented yielding Rabi frequencies of up to $2\pi \cdot 0.78(5)\,\text{MHz}$. Following this, Rydberg-blockade between atoms at neighboring array sites separated by $7.0(2)\,\mu\text{m}$ was achieved using a sequential addressing scheme.
Additional advances were made regarding the coherent coupling between the hyperfine ground states which led to sub-microsecond π-pulse durations in the large-scale array. On that basis, the tweezer platform was turned into a two-dimensional site-resolved sensor array for magnetic fields. Using a total of 270 individual-atom sensors covering an area of $119\,\mu\text{m} \times 98\,\mu\text{m}$ allows for parallelized detection of external magnetic fields with a sensitivity of $100\,\text{nT}$ and a spatial resolution of $7\,\mu\text{m}$. Utilizing a single-atom probe in a movable optical tweezer, significantly enhanced the spatial resolution while the sensitivity stayed in agreement with the result obtained via parallelized detection.
Furthermore, novel concepts to extend the available tweezer configurations of the present quantum platform have been evaluated. This includes the implementation of spatial light modulation with digital micromirror devices (DMD) as well as 3D-printed microlens arrays. Applying DMD-based addressing of microlenses, dynamic reconfiguration of tweezer geometries could be demonstrated with individual-site control. In addition, 3D printing was found to offer even further flexibility in the configuration of the microlens array itself. This led to the development of a hybrid tweezer setup combining the stability involved with microlens-based platforms, the short-term modification of the fundamental lens arrangement based on rapid prototyping of user-definable microlens arrays, and the DMD-based reconfigurability with real-time control for the creation of versatile tweezer geometries.

Zusammenfassung

Register aus optischen Pinzetten bieten eine vielseitige Umgebung für die präzise Kontrolle der internen und externen Freiheitsgrade von Quantensystemen aus neutralen Atomen. Dabei ergibt sich eine Fülle von Anwendungsmöglichkeiten in einer Vielzahl an Forschungsfeldern einschließlich Quanteninformationsverarbeitung und -simulation, Vielteilchenphysik sowie Quantensensorik. Die mikrooptische Plattform, welche in dieser Arbeit vorgestellt wird, resultiert in einem großflächigen Dipolfallenregister, das durch einzeln fokussierte Laserstrahlen mit einer Strahltaille von $1.45(10)$ µm erzeugt wird. Unter Ausnutzung lichtinduzierter Stöße werden in einem typischen Arbeitsbereich von 361 Fallenplätzen $191(17)$ lasergekühlte Atome räumlich getrennt voneinander bei Fallentiefen im Bereich von $k_\mathrm{B}\cdot$ Millikelvin präpariert.
Im Rahmen dieser Arbeit wurde eine Technik implementiert, welche den Transport von Atomen zwischen Fallen erlaubt, womit eine stochastisch gegebene Anfangsverteilung in eine vorgegebene Zielstruktur überführt werden kann. Dies erlaubt nicht nur die Durchführung von Experimenten ausgehend von einem wohldefinierten Anfangszustand, sondern auch die Kompensation von Atomverlusten innerhalb eines Messzyklus und damit die Reduktion der Notwendigkeit von zeitaufwendigen Phasen der Laserkühlung. Basierend auf diesem Ansatz konnten fehlstellenfreie Strukturen aus bis zu 111 Atomen erzeugt und der Weg für Experimente bereitet werden, welche vorher nicht in sinnvoller Zeitdauer durchführbar waren.
Entscheidende Fortschritte wurden hinsichtlich der Realisierung von Zwei-Qubit-Operationen in dieser experimentellen Plattform gemacht. Über einen Zwei-Photonen-Prozess wurde die kohärente Kopplung zwischen einem Hyperfein-Grundzustand des $5S_{1/2}$-Grundzustandes und einem $82S_{1/2}$- Rydbergzustand unter Einzelplatzauflösung mit Rabifrequenzen von $2\pi \cdot 0.78(5)$ MHz realisiert. Dies ermöglichte den Nachweis der Rydberg-Blockade zwischen Atomen benachbarter Fallenplätze in einem Abstand von 7.0(2) µm unter sequentieller Adressierung.
Hinsichtlich der kohärenten Kopplung innerhalb von Hyperfein-Grundzuständen konnten π-Pulszeiten unterhalb von einer Mikrosekunde realisiert werden. Daran anknüpfend wurde die vorliegende Plattform als zweidimensionaler Magnetfeldsensor genutzt. Dieser bietet 270 Einzelatom-Sensoren für parallelisierte Detektion, welche bei einer Sensitivität von 100 nT eine Fläche von 119 µm $\times$ 98 µm mit einer räumlichen Auflösung von 7 µm abdecken. Weiterhin konnte die Detektion mit einem unabhängigen Einzelatom-Sensor in einer beweglichen optischen Pinzette gezeigt werden, welche die Erhöhung der räumlichen Auflösung ermöglicht und ein zur parallelisierten Messung übereinstimmendes Ergebnis liefert.
Schlussendlich wurden neuartige Konzepte entwickelt, welche einen erheblich höheren Grad an Flexibilität hinsichtlich der im Experiment konfigurierbaren Fallengeometrien bieten. Diese beinhalten räumliche Intensitätsmodulation mit digitalen Mikrospiegeleinheiten (DMD) ebenso wie 3D-gedruckte Mikrolinsenregister. DMD-basierte Adressierung von Mikrolinsen erlaubte die dynamische Anpassung von Fallengeometrien mit Einzelplatzkontrolle. Außerdem erwies sich 3D-Druck als weitere Möglichkeit zur flexiblen Konfiguration von Mikrolinsenregistern. Damit konnte ein hybrider Aufbau optischer Pinzetten entwickelt werden, welcher die Stabilität einer Mikrolinsen-basierten Plattform mit kurzfristiger Anpassbarkeit der Linsengeometrie beruhend auf schneller Prototypenentwicklung von benutzerdefinierten Registern und Echtzeitkontrolle für vielseitige Fallengeometrien kombiniert.

Contents

1. Introduction

With the words *"For those who are not shocked when they first come across quantum theory cannot possibly have understood it. Probably I spoke so badly that no one knew what I was talking about."* Niels Bohr recapitulates the impressions after an introduction to quantum mechanics he has given at a conference meeting wondering why no one *"raised any objections or asked any embarrassing questions"* [1]. Raising the right question can not only yield astonishing insights on the road to an answer but also has the potential for ground-breaking inventions to shift whole industries albeit possibly many decades later.
More than 100 years after the emergence of quantum theory at the beginning of the last century [2] the list of open questions in this field of research is still long. In contrast, solutions to quantum theory related problems are immanent in today's technologies which heavily rely on a profound understanding of light and matter on a single-quantum level. From the experimental point of view that requires precise control over the internal and external degrees of freedom of a well-isolated system under test [3, 4] while otherwise decoherence can obscure the quantum properties [5]. In the last decades, tremendous progress has been made with respect to control quantum systems. Based on laser cooling techniques [6–8] clouds of neutral atoms approaching the point of absolute zero temperature have been realized which allowed to accomplish quantum phase transitions and investigate theoretical models from condensed matter physics [9, 10]. These systems are closely related to the highly topical phenomenon of superconductivity and can be tuned with experimental parameters to reproduce the transition from conducting to insulating solids [11]. The principal idea connected to this is the integration of properties of one quantum system within another and goes back to a proposal for quantum simulators by Richard Feynman [12] from 1982. This approach is especially vital if a theoretical model of the original object is available which would in principle allow for a classical computer-based simulation in order to compare theoretical predictions with the outcome of a factual experiment but a realization is infeasible due to limited computational resources facing the high complexity of the involved dynamics or system size.
Three years later this is taken up by D. Deutsch who presents the concept of a universal quantum computer which relies on qubits instead of conventional bits as the fundamental unit of information and exhibits the capability to perform certain probabilistic tasks faster than its classical pendent due to exploitation of quantum parallelism [13]. In this context, the algorithm by Grover for inverse search within an unsorted database [14] and Shor's protocol for prime factorization in polynomial run time [15] are prominent examples while the latter questions the security of typical public-key cryptography algorithms used today. Moreover, these devices could also act as a universal quantum simulator [16] while simulating a different system would correspond to executing an adapted algorithm without the necessity to modify the underlying platform. First algorithms have already been successfully implemented in nuclear magnetic resonance (NMR) setups more than twenty years ago [17, 18] and a large variety of candidates, among them trapped-ion platforms [19, 20], superconducting circuits [21–23] and ultracold quantum gases [24, 25] are currently evaluated. However, there is still a long way to achieve a truly universal system [26] which eventually outperforms its classical counterpart. Present approaches have either restricted applicability or are tailor-made to solve

specific problems while crucial challenges are scalability and error correction [27].
Platforms based on individually trapped neutral atoms provide well-isolated quantum systems which are extendable from one [28] to two [29–32] and three dimensions [33–35] with tunable interactions [36, 37] that allow for creation of entanglement [38–40] and the implementation of high fidelity two [41, 42] and three [42] qubit gates. This makes them ideally suited to work in the intersection between quantum simulation, quantum computation and quantum metrology in a versatile manner. As a consequence, progress in a specific platform working in one of these fields, for instance with respect to quantum control, has a high chance to incorporate direct benefit if applied to the others. This continuously triggers progress and results in a rapidly evolving field.
Especially, utilizing excitation into Rydberg states which is applied in a variety of different setups providing sensitive on demand coupling to external fields or among otherwise isolated atoms [3, 43–45] can be adapted to these platforms with well-defined spatial separation of atoms [46]. In this fashion, simulations on quantum magnetism using the XY-spin Hamiltonian model [47] and Ising-type interactions [48–50] as well as topological phases of matter have been conducted [51]. The latter ones are highly topical in view of topological quantum computation as proposed by A. Kitaev [52] in 1997 as a possible scheme to implement error correction.
Scalability to large systems of neutral atom configurations with still well-defined initialization, individually addressable qubits, and flexibility in their alignment for precise interaction control is essential in propelling this field to the next major breakthrough.
The micro-optical platform presented in this thesis and the related concepts are designed to tackle exactly these challenges. Single focused beam tweezers are created in the spirit of the idea realized by A. Ashkin [53], yet in a massively parallelized fashion. This results in configurations which are intrinsically highly scalable in a straightforward way while allowing for site-selective addressability to execute coherent operations [54] and parallelized coherence-preserving transport [55]. Providing individual neutral atoms in a well-defined spatial separation [31] the experimental setup allows for controlled Rydberg-mediated interactions with parallelized excitation into Rydberg states [56].
In the course of this thesis, significant progress with respect to scaling up the system size and preparation of a well-defined initial situation for experiments has been made. Furthermore, the control over Rydberg interactions has been enhanced which now allows for individual qubit access. Moreover, the applicability of the neutral atom platform could extended to the field of quantum metrology providing further evidence of its versatility. In order to find still untapped optimization possibilities of the experimental apparatus emerging technologies have been evaluated with respect to their applicability in the setup. All of these topics will be detailed in this thesis and a separate chapter is dedicated to each one.
In **Chapter 2** the experimental apparatus is presented and its relevant fundamental aspects are covered. It will be outlined how laser cooling techniques allow for preparation of individual atoms in the tweezer array at random positions using a stochastic loading mechanism. Furthermore, the concept for implementation of interatomic coupling in the setup will be discussed.
Chapter 3 directly connects to this stage and deals with a new implementation of an extended tweezer setup with the capability to turn the initial stochastic occupation in the array into defect-free clusters of more than 100 atoms. This work has been conducted in close cooperation with D. Ohl de Mello and is discussed in detail also in [57] and in our related publication [31]. Consequently, this chapter will focus on the essential characteristics and achievements of the setup.
Chapter 4 demonstrates an extension to the experimental apparatus which enables site-selective

coherent Rydberg excitations as well as site-selective Rydberg blockade. This is an essential step for implementation of Rydberg-mediated interactions with individual-atom control and the realization of two-qubit gates in the experimental setup.
Chapter 5 depicts an unprecedented quantum metrological application for the tweezer platform. Turning the atom array into a magnetic-field sensitive two-dimensional plane allows for gradient-field sensing with single-site resolution. As a test case this will be used to map the field gradient of the magneto-optical trap.
Chapter 6 discusses concepts for further extensions of the experimental platform using state-of-the-art technologies such as 3D-printed micro-optics and digital micromirror devices (DMD). Additionally, DMD-based microlens array addressing will be introduced which allows for fast on-demand modification of fundamental trap geometry given by the lens pattern. Moreover, both technologies will be finally combined to enable even more flexibility.
Chapter 7 compiles the key results and prospects for possible future work are outlined.

2. Scalable quantum platform based on micro-fabricated optical elements

2.1. Large-scale optical tweezer arrays of focused laser beam traps

2.1.1. Trapping atoms with light

The use of light to control the external degrees of particles reaches back to the first experiments by A. Ashkin[1] in 1970s [53, 58, 59] and has developed into an indispensable tool in a plethora of research fields, including physics, chemistry, biology, and medical research [59–62]. Thanks to the high level of dynamic range in the interaction strength between light and matter, optical tweezers are extremely versatile and can be used in order to monitor and control the external degrees of freedom of a large variety of target objects ranging from single atoms to living organisms.
With regard to trapping of atomic particles as well as atom-light interaction in general, there exists a profound theoretical basis which is comprehensively discussed in literature [63, 64]. The theoretical treatment of that topic in this chapter follows the detailed derivations presented in [64].
The Hamilton operator of the system comprising an atom interacting with a light field is given by

$$\hat{H} = \hat{H}_\mathrm{A} + \hat{H}_\mathrm{L} + \hat{H}_\mathrm{I} \tag{2.1}$$

where $\hat{H}_\mathrm{A}$ denotes the Hamilton operator of the atom, $\hat{H}_\mathrm{L}$ the Hamiltonian of the light field, and $\hat{H}_\mathrm{I}$ covers the interaction between both.
The analysis can be simplified significantly by assuming that the atom does only exhibit two energy levels, a ground state $|g\rangle$ and an excited state $|e\rangle$, separated by an energy $\hbar\omega_0$ as indicated in Fig. 2.1 (a). Even though this is a considerable simplification it provides strong insight and serves as a good approximation as long as the interaction is dominated by coupling to one atomic transition. Then, the Hamilton operator of a two-level atom can be written in terms of the resonance frequency ω_0 and the atomic lowering operator $\sigma = |g\rangle\langle e|$ as

$$\hat{H}_\mathrm{A} = \hbar\omega_0\sigma^\dagger\sigma. \tag{2.2}$$

Similarly the Hamiltonian of a monochromatic light field of frequency ω_L can be written using the ladder operators $a^\dagger$ and a, respectively, as

$$\hat{H}_\mathrm{L} = \hbar\omega_\mathrm{L}\left(a^\dagger a + \frac{1}{2}\right). \tag{2.3}$$

In a semiclassical approach using a classical electric field with amplitude $\boldsymbol{E}$ the interaction Hamilton operator in the dipole approximation is given by

$$\hat{H}_\mathrm{I} = -\hat{\boldsymbol{d}}\boldsymbol{E} \tag{2.4}$$

where $\hat{\boldsymbol{d}} = -e\hat{\boldsymbol{r}}_\mathrm{e}$ denotes the dipole operator for an atom having a single electron[2] at the

[1] Nobel Prize in Physics 2018 "for the optical tweezers and their application to biological systems."
[2] For alkali atoms with only one electron in the outer shell this assumption is reasonable.

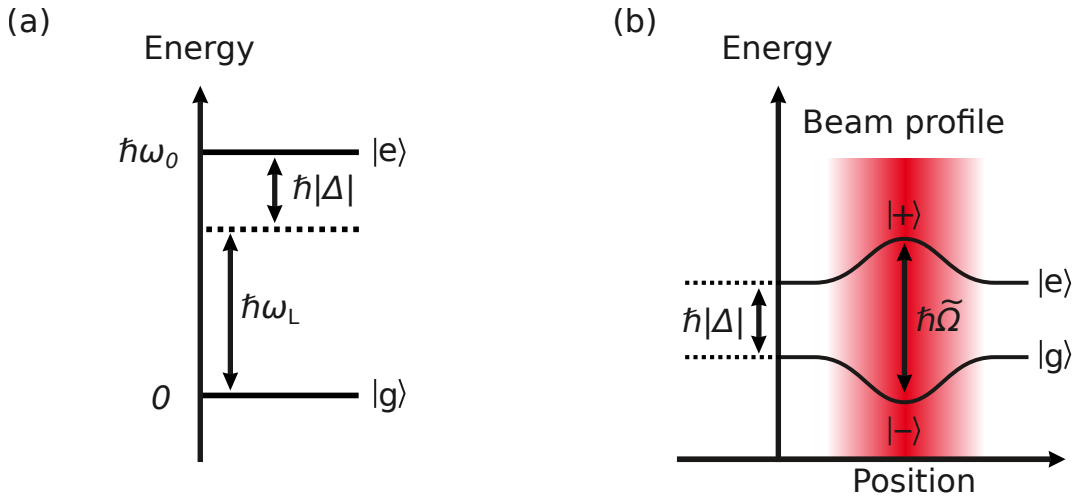

Figure 2.1.: Dipole potential in the dressed states picture. (a) In an idealized two-level system a light field detuned by $\Delta < 0$ couples with the bare atomic states. (b) This leads to new eigenstates with intensity-dependent energy eigenvalues.

position $\hat{\boldsymbol{r}}_\mathrm{e}$.
Under the long-wavelength approximation[3] an incident light field with a frequency ω_L can be written as

$$\begin{aligned}\boldsymbol{E}(t) &= \boldsymbol{\epsilon} E_0 \cos(\omega_\mathrm{L} t) \\ &= \boldsymbol{E}^{(+)}(t) + \boldsymbol{E}^{(-)}(t)\end{aligned} \tag{2.5}$$

where the field is decomposed into positive- and negative-rotating components $\boldsymbol{E}^{(\pm)}(t) \propto e^{-i(\mp\omega_\mathrm{L})t}$.
Similarly, this can be done for the dipole operator

$$\begin{aligned}\hat{\boldsymbol{d}} &= -e\hat{\boldsymbol{r}}_\mathrm{e} \\ &= \langle g|\,\hat{\boldsymbol{d}}\,|e\rangle \left(\sigma + \sigma^\dagger\right) \\ &= \hat{\boldsymbol{d}}^{(+)} + \hat{\boldsymbol{d}}^{(-)}\end{aligned} \tag{2.6}$$

defining positive- and negative rotation components $\hat{\boldsymbol{d}}^{(\pm)} \propto e^{-i(\mp\omega_\mathrm{L})t}$.
Discarding the fast rotating terms[4] under the assumption $|\omega_\mathrm{L} - \omega_0| << \omega_\mathrm{L} + \omega_0$ and using the expressions for $\boldsymbol{E}$ and $\hat{\boldsymbol{d}}$ the interaction Hamilton operator can be written as

$$\begin{aligned}\hat{H}_\mathrm{I} &= -\hat{\boldsymbol{d}}^{(+)}\boldsymbol{E}^{(-)} - \hat{\boldsymbol{d}}^{(-)}\boldsymbol{E}^{(+)} \\ &= \frac{\hbar\Omega_0}{2}\left(\sigma e^{i\omega_\mathrm{L}t} + \sigma^\dagger e^{-i\omega_\mathrm{L}t}\right)\end{aligned} \tag{2.7}$$

with the Rabi frequency

$$\Omega_0 = -\frac{\langle g|\,\boldsymbol{\epsilon}\hat{\boldsymbol{d}}\,|e\rangle}{\hbar} E_0. \tag{2.8}$$

[3] This neglects the spatial dependence of the electric field amplitude. However, as optical wavelengths are on the order of several hundreds of nm compared to the single Å scale of atoms the assumption can be justified.
[4] This is known as the rotating-wave approximation (RWA).

Transforming into the rotating frame of the laser field simplifies the expressions for the atom $\hat{H}_{\mathrm{A}}^{\prime} = -\hbar\Delta\sigma^{\dagger}\sigma$ and the interaction Hamilton operator $\hat{H}_{\mathrm{I}}^{\prime} = \frac{\hbar\Omega_0}{2}\left(\sigma + \sigma^{\dagger}\right)$ further. Here, Δ denotes the detuning $\Delta = \omega_{\mathrm{L}} - \omega_0$ of the laser frequency to the resonance. This renders the full Hamilton operator time independent. As the effect of stimulated absorption and emission of single photons on a classical light field can be neglected $\hat{H}_{\mathrm{L}}$ is not considered any further. Diagonalization of the rotating-frame Hamilton operator $\hat{H}^{\prime}$ with

$$\hat{H}^{\prime} = \hat{H}_{\mathrm{A}}^{\prime} + \hat{H}_{\mathrm{I}}^{\prime} = \hbar \begin{pmatrix} -\Delta & \Omega_0/2 \\ \Omega_0/2 & 0 \end{pmatrix} \tag{2.9}$$

in the uncoupled energy basis yields the new eigenvectors $|+\rangle$ and $|-\rangle$ while it turns out that they can be expressed through rotation of the uncoupled states

$$\begin{aligned} |+\rangle &= \sin\theta\,|g\rangle + \cos\theta\,|e\rangle \\ |-\rangle &= \cos\theta\,|g\rangle - \sin\theta\,|e\rangle \end{aligned} \tag{2.10}$$

when defining the Stückelberg angle θ as:

$$\tan 2\theta = -\frac{\Omega_0}{\Delta} \quad \left(0 \leq \theta \leq \frac{\pi}{2}\right) \tag{2.11}$$

The corresponding eigenvalues evaluate to

$$E_{\pm} = -\frac{\hbar\Delta}{2} \pm \frac{\hbar\tilde{\Omega}}{2} \tag{2.12}$$

using the generalized Rabi frequency $\tilde{\Omega} = \sqrt{\Omega_0^2 + \Delta^2}$. The alternation of the eigenenergies due to the light field is called the ac Stark shift. This leads to a spatially dependent potential in case of a spatial variation of the intensity of the light field $I(\boldsymbol{r}) = \frac{1}{2}c\epsilon_0\left|E_0(\boldsymbol{r})\right|^2 \propto \left|\Omega_0(\boldsymbol{r})\right|^2$ and is illustrated in Figure 2.1 (b) for the case of red-detuned light, i.e. $\Delta < 0$. As the parameters of dipole traps are typically chosen in a way that the atoms are predominantly in the ground state this configuration acts as an attractive potential. Finally, expanding equation 2.12 to the lowest order in $\frac{\Omega_0}{\Delta}$ yields the expression for the dipole potential

$$U_{\mathrm{D}} \approx \frac{\hbar\left|\Omega_0\right|^2}{4\Delta} = \frac{3\pi c^2}{2\omega_0^3}\frac{\Gamma}{\Delta}I(r). \tag{2.13}$$

Complementarily, the spontaneous emission rate

$$\Gamma = \frac{\omega_0^3}{3\pi\epsilon_0\hbar c^3}\left|\langle g|\,\hat{\boldsymbol{d}}\,|e\rangle\right|^2 \tag{2.14}$$

describes the coupling of the excited level to the vacuum field according to the approach by Weisskopf and Wigner [65]. The expansion in equation 2.12 is appropriate as for the dipole traps the detunings are typically kept large, i.e. $|\Delta| >> \Gamma, \Omega_0$. The reason for this becomes obvious when treating the evolution of states in the formalism of density operators which includes spontaneous emission using the optical Bloch equations yielding a rate for incoherent scattering processes of

$$\Gamma_{\mathrm{SC}} = \frac{3\pi c^2}{2\hbar\omega_0^3}\left(\frac{\Gamma}{\Delta}\right)^2 I(\boldsymbol{r}). \tag{2.15}$$

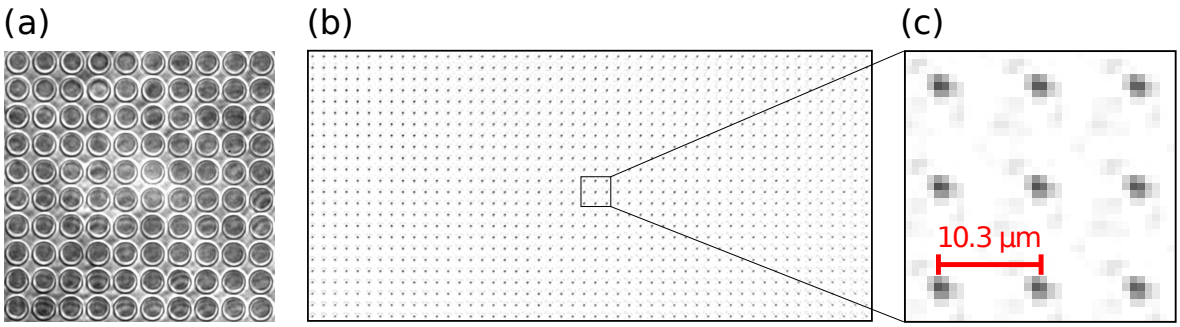

Figure 2.2.: Using microlens arrays to create large arrays of dipole potentials. (a) Microscope image of a 10 × 10 subsection of a refractive microlens array with a pitch of 30 µm. (b) Reimaged focal plane of a microlens array with a pitch of 110 µm. More than 1000 traps are shown out of a region comprising more than 2500 spots each separated by 10.3(3) µm due to the magnification of $M = 0.094(3)$.

Due to the scaling of $U_\mathrm{D} \propto I/\Delta$ and $\Gamma_\mathrm{SC} \propto I/\Delta^2$ it is vital to work at the highest possible detuning permitted by the available intensity in order to minimize the rate of scattering processes which lead to loss of coherence and reduce the lifetime of the atoms in the trap due to heating.

Even though the analysis above provides a qualitative insight into the aspects relevant for trapping neutral ^{85}Rb atoms by light it does not cover two crucial aspects: the polarization of the laser light and the factual multilevel character of the atom (see Fig. A.1). As discussed in [66] a more comprehensive treatment yields the dipole potential for an atom in the hyperfine ground state with a magnetic quantum number m_F coupling to both D-transitions in a far detuned laser field

$$U_\mathrm{D} = \frac{\pi c^2 \Gamma}{2\omega_0^3} \left(\frac{2 + \mathcal{P} g_\mathrm{F} m_\mathrm{F}}{\Delta_2} + \frac{1 - \mathcal{P} g_\mathrm{F} m_\mathrm{F}}{\Delta_1} I(r) \right) \tag{2.16}$$

while $\mathcal{P}$ accounts for the polarization of the laser field being $\mathcal{P} = \pm 1$ for circular polarized light ($\sigma^\pm$) and $\mathcal{P} = 0$ for linear polarization (π) and Δ_1 and Δ_2 cover the detuning to D_1 and D_2 line, respectively. This shows that for circular polarized light the dipole potential becomes dependent on m_F raising additional complications. This effect is not intended for the experiments conducted during this work and a linear polarization is chosen in the experimental implementation. Further analysis on this topic with special regard to the present setup can be found in [67].

The large detuning that is desired in face of equation 2.15 which in turn demands highly intense light fields for sufficiently deep traps can be accomplished by creating tightly focused laser beams, a concept, which will be covered in the subsequent section.

2.1.2. Scalable arrays of focused beam traps

Single-beam optical dipole trap

According to equation 2.13, red-detuned light leads to an attractive potential for ground state atoms $U_\mathrm{D}(\boldsymbol{r}) \propto I(\boldsymbol{r})$. Consequently, a laser beam focused through a lens with focal length f can serve as a three-dimensional trapping potential which is commonly treated in the approximation of a Gaussian beam. Using cylindrical coordinates (r, z) the intensity distribution of a beam

with power P propagating along the z-axis is given by

$$I(r,z) = \frac{2P}{\pi w^2(z)} e^{-\frac{2r^2}{w^2(z)}} \tag{2.17}$$

where the coordinate system is defined such that the focus is at (0,0). Here,

$$w(z) = w_0 \sqrt{1 + \frac{z^2}{z_\mathrm{R}^2}} \tag{2.18}$$

is the z-dependent $1/e^2$-radius, i.e. the radial distance until the intensity is reduced to $1/e^2$ of the value for $r = 0$ for a given axial position z. The dependence of $w(z)$ on z is governed by the Rayleigh range

$$z_\mathrm{R} = \frac{\pi}{\lambda} w_0^2. \tag{2.19}$$

The minimal radius, i.e. the waist

$$w_0 = \frac{\lambda f}{\pi w(f)} \tag{2.20}$$

is obtained in the focus of a lens with a focal length f while z_R denotes the axial distance until the radius of a beam with a wavelength λ has increased by a factor $\sqrt{2}$.
With respect to trapping of laser cooled neutral ground state atoms the resulting potential can be approximated harmonically due to the fact that the wave function of an atom with mass m is small compared to the spatial dimensions of the trapping potential along w_0 and z_R, respectively. This yields the radial

$$2\pi\nu_\mathrm{r} = \sqrt{\frac{4U_0}{m w_0^2}} \tag{2.21}$$

and axial

$$2\pi\nu_\mathrm{z} = \sqrt{\frac{2U_0}{m z_\mathrm{R}^2}} \tag{2.22}$$

trap frequencies for a potential depth of $U_0 \propto I(0,0)$. As elaborated in [55] the intensity distribution of a plane wave focused by a lens having a limited circular aperture can also be approximated by a Gaussian intensity distribution in the focal plane. For an aperture radius a this yields

$$w_0 = \frac{\sqrt{2}\lambda f}{\pi a} = \frac{\sqrt{2}\lambda}{\pi NA} \tag{2.23}$$

with the numerical aperture $NA = a/f$. This is of special relevance in this work due to the fact how the dipole trap array is generated.

Large-scale parallelized dipole trap generation

Inspired by the idea to create trapping potentials via focusing a laser beam this concept is massively parallelized using a microlens array illuminated by a laser beam with a radius w much larger then the diameter of each microlens. The microscope image in Fig. 2.2 (a) shows a 10×10 section of a microlens array with a pitch of $d = 30\,\mu\mathrm{m}$. Each lens is clearly visible and illuminated with a large beam produces a corresponding focus in the focal plane of the

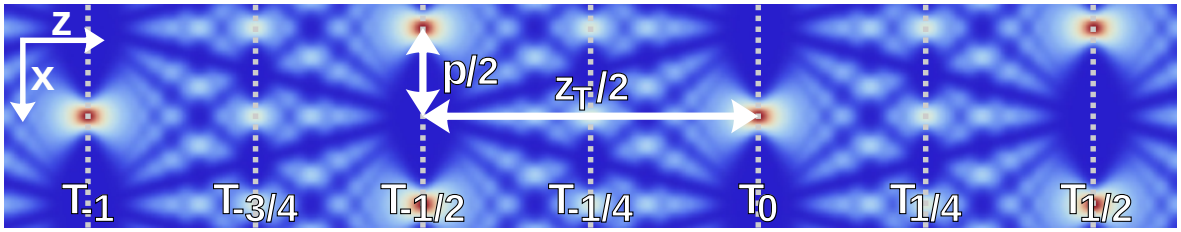

Figure 2.3.: Talbot carpet simulation for a reimaged focal plane of a microlens array with a characteristic tweezer pitch of 14.1 µm. Microlens array based setups create intrinsically three-dimensional trapping potentials due to the self-imaging properties when illuminated with coherent laser light. This leads to additional planes at distance $z_\mathrm{T}^\star = \frac{z_\mathrm{T}}{2}$ exhibiting the same trap pitch as the focal plane. Taken from [68].

array. However, the available array size is by no means limited to the order of hundred lenslets. In contrast, due to the lithographic production process the structures are heavily scalable and arrays comprising a million lenses have already been produced. Using additional optics the focal plane of a microlens array can be reimaged which allows for flexible rescaling of the spot pattern. Figure 2.2 (b) shows the reimaged focal plane of a 110 µm-pitch array yielding well-defined spots with a separation of $p = 10.3(3)$ µm as indicated in the detail (Fig. 2.2 (c)). This demonstrates the excellent scalability of the approach of microlens array based focused beam dipole trap arrays.
The experiments in this work rely on a set of different commercially available and a custom-made microlens array. While the latter is comprehensively characterized in Chapter 6 the specifications of the former are given in Table 2.1. Due to large variety of commercially available microlens arrays one can easily adapt the tweezer parameters via selection the array and appropriate reimaging optics. This allows for instance to easily reduce the tweezer pitch simply via replacement of MLA1 with MLA2. As illustrated in the example of MLA3 this is not necessarily restricted to a quadratic grid. Chapter 6 will demonstrate that hexgonal-grid microlens arrays can be used in the same way to create large-scale optical tweezer arrays.

Talbot effect

As illustrated in Fig. 2.3 and analyzed in detail in [67, 68], these systems are intrinsically three-dimensional. Using coherent light for illumination of the microlens array leads to additional planes along the optical axis (z) which can be used as trapping potentials for atoms. This self-imaging feature is called the Talbot effect and the Talbot length z_T is the distance between two Talbot planes. In addition there exist intermediate planes which exhibit the same distance of the trapping potentials p with comparable depth while they appear laterally displaced by $p/2$ in both dimensions and intermediate planes with different parameters. Considering only the ones which have the same characteristics as the focal plane the axial distance $z_\mathrm{T}^\star$ between layers is given by

$$z_\mathrm{T}^\star = \frac{z_\mathrm{T}}{2} = \frac{p^2}{\lambda}. \tag{2.24}$$

For instance, using a dipole trap array pitch of $p = 10.3$ µm as for the configuration shown in Fig. 2.2 (b, c) this amounts to $z_\mathrm{T}^\star = 133$ µm. Further analysis and a detailed theoretical treatment of the Talbot effect can be found in [69].

Label	Serial number	Type	R_c	d	NA	p
MLA1	11-1401-101-111	quad	0.86 mm	110 µm	0.03	10.3(3) µm
MLA2	19-00021	quad	500 µm	75 µm	0.03	7.0(2) µm
MLA3	APH-Q-P161.5-R2.05	hex	2.05 mm	161.5 µm	0.02*	7.4(2) µm

Table 2.1.: Overview of the commercially available microlens arrays used in the context of this thesis. R_c denotes the microlens radius of curvature, d the microlens pitch and NA the numerical aperture. (*) The value for MLA3 is a calculated approximation from the clear aperture due to the non-circular lens pattern. Each microlens array is used in combination with reimaging optics leading to a demagnified tweezer pitch p.

2.2. Laser systems

The experiments presented in this thesis rely on optical techniques and lasers play a central role for cooling, trapping and fluorescence imaging of atoms as well as state preparation, detection, and coherent control to name only a few applications. For these purposes, a double-digit number of individual laser systems need to be precisely stabilized with respect to frequency but also concerning intensity [70]. Therefore, in general each laser system that provides light which is directed to the experimental apparatus is fiber-coupled and intensity stabilized via a feedback-loop controlling an acousto-optic modulator (AOM) before the fiber. For frequency stabilization at $\lambda = 780$ nm a master laser which is locked via modulation transfer spectroscopy (MTS) serves as a reference [71, 72]. Relative to this laser other systems that are running at the D_2-line can be stabilized via a beat frequency measurement using an offset locking technique. Concerning the D_1-transition a similar configuration is available [73]. All lasers except for the one proving the light for the optical tweezers and the blue Rydberg laser system are external-cavity diode lasers (ECDL). When stabilized they exhibit a long-term linewidth which is typically below 0.5 MHz and an output power of up to 100 mW. The light for the tweezers is supplied by a Ti:sapphire laser (899-01, Coherent) which is pumped by a frequency-doubled Nd:YVO_4 laser (Verdi V18, Coherent) at a wavelength of 532 nm. This system can be tuned within a range of 760 nm and 850 nm, though for the measurements conducted in the course of this thesis it is used at about 797 nm where it provides typically about 2.5 W output power. The specifics of the Rydberg laser system will become relevant in Chapter 4 and be detailed in that context.

2.3. Vacuum apparatus

In order to create a well isolated environment where quantum dynamics of individual atoms can be analyzed an ultra-high vacuum apparatus is used that has been built and put into operation during the work of [74] while a detailed description is also available in [75]. Figure 2.4 shows a computer-generated image of the chamber which has a spherical basic shape but is flattened on the front and back side. This allows for large optical view ports and access by high numerical aperture optics. These windows as well as the additional eight ports on the spherical surface are coated with double-sided anti-reflection layers for light between 700 nm and 1100 nm within an acceptance angle of up to about 45°. The horizontal side ports are also used as ports for the delivery of rubidium into the chamber via dispensers located in the

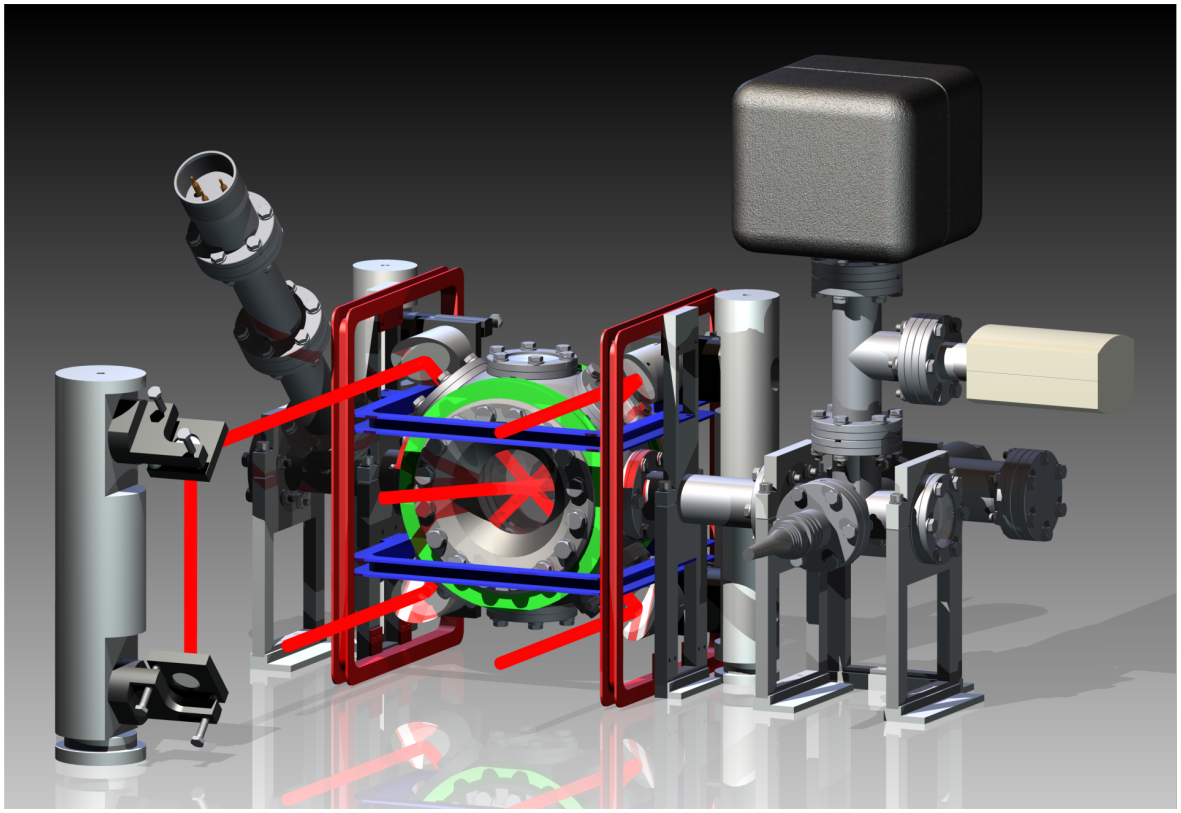

Figure 2.4.: Rendered image showing the vacuum apparatus. The computer generated image depicts the central section of the experimental setup where the experiments with laser cooled rubidium atoms are conducted. The laser beams for the MOT are indicated as well as the coils which are used for compensation of the earth's magnetic field and allow the application of homogeneous fields at the location of the trapped atoms. The anti-Helmholtz coils of the MOT gradient field are invisible within the plane of the green-colored coils. The image is taken from [67].

right tube and as ports to the vacuum pumps. The vacuum which typically measures below 3×10^{-9} mbar is permanently maintained by an ion getter pump (Starcell, Varian) (right connector) and can be additionally optimized using an Titanium sublimation pump (SB-1020, Hositrad) (left connector). As the coupling of neutral atoms to magnetic fields has significant impact on their energy level structure there exists the necessity for precise control not only for state-of-the-art laser cooling techniques but also through the subsequent experimental phase. Therefore, three pairs of coils are attached to the apparatus (mountings indicated in red, blue and green, respectively) which enable compensation of the earth's magnetic field as well as the application of homogeneous fields to create a well-defined quantization axis. Regarding the compensation a residual magnetic field of $|B_{\mathrm{res}}| = 2.1(1)\,\mu\mathrm{T}$ has been spectroscopically measured in [76] while quantization fields of typically $B_{\mathrm{x,q}} = 283(1)\,\mu\mathrm{T}$ are applied in the work detailed in this thesis. Moreover, another pair of coils lies within the fixtures for the front and back window that are used in anti-Helmholtz configuration for generation of a magnetic gradient field during laser cooling using a magneto-optical trap (MOT) which is the basic starting point for each experimental cycle and will be discussed in the following section.

2.4. Magneto-optical trap and optical molasses

Since the ground-breaking experiments and theoretical analysis documented in [6–8] laser cooling has become an indispensable tool for cold and ultracold neutral atom experiments. A magneto-optical trap (MOT) relies on this concept and allows for cooling and trapping of an atom cloud which can be used in a subsequent experimental stage. Utilizing laser light red-detuned to an atomic transition leads to a velocity dependent force on the atoms due to photon scattering resulting in a deceleration, and consequently, reduction of temperature. In order to account for all atomic degrees of freedom crossed laser beams are typically used as indicated in Fig. 2.4. Additionally, a magnetic gradient field adds a spatial dependence and prevents diffusion of atoms from the trap region. Based on a simplified model of two-level atoms being in a steady state of absorbing and emitting photons the minimum temperature achievable amounts to the so-called Doppler temperature

$$T_{\mathrm{D}} = \frac{\hbar\Gamma}{2k_{\mathrm{B}}}. \tag{2.25}$$

In the present setup, laser cooling of rubidium atoms is done via the hyperfine transition $|5\mathrm{S}_{1/2}, F = 3\rangle \rightarrow |5\mathrm{P}_{3/2}, F = 4\rangle$. The natural linewidth of the excited state $\Gamma = 2\pi \cdot 6.067\,\mathrm{MHz}$ yields $T_{\mathrm{D}} = 146\,\mu\mathrm{K}$. However, already in [77] it was observed that the actual temperature of an laser-cooled ensemble can fall short of the Doppler limit and the polarization of the light has to be taken into account as well as the existence of Zeeman sublevels. This brings up a new limitation, the recoil temperature T_{R} which is defined as the temperature of an ensemble that exhibits a one-dimensional rms-momentum of $\hbar k$, i.e. one photon recoil:

$$T_{\mathrm{R}} = \frac{\hbar^2 k^2}{m k_{\mathrm{B}}} \tag{2.26}$$

Using the absolute value of the wavevector $k = |\boldsymbol{k}| = \frac{2\pi}{\lambda}$ and the atomic mass $m = 85\,\mathrm{u}$ of $^{85}\mathrm{Rb}$ this amounts to $T_{\mathrm{R}} = 370\,\mathrm{nK}$. In this experiment, typical temperatures of the atom ensemble after MOT and molasses lie on the order of 5 µK. Applying sophisticated laser cooling schemes this limitation can be surpassed, too, which is however beyond the scope of this thesis [78].
The fact that the assumption of a two-level system is only an approximation has certainly an important second consequence: As atoms can escape the cooling cycle via excitation to $|5\mathrm{P}_{3/2}, F = 3\rangle$ and a subsequent spontaneous emission process into $|5\mathrm{S}_{1/2}, F = 2\rangle$ an additional repump laser is necessary that provides near resonant light to $|5\mathrm{S}_{1/2}, F = 2\rangle \rightarrow |5\mathrm{P}_{3/2}, F = 3\rangle$ which successively transfers these atoms back to $|5\mathrm{S}_{1/2}, F = 3\rangle$. The specifics about the implementation of the MOT in the experimental apparatus will be treated at the beginning of the following section which deals with the preparation of individual laser-cooled atoms in the dipole trap array.

2.5. Loading and trapping of single Rb atoms in dipole trap arrays

Figure 2.5 outlines the concept for preparation of the neutral-atom quantum array and the specific implementation used in this work. As indicated in the fluorescence images in Fig. 2.5 (a) atoms from the laser cooled cloud (left) shall be loaded into the two-dimensional trap pattern generated by a microlens array (right). Figure 2.5 (b) shows a simplified on-top-view of the optical setup essential for laser cooling, loading, and trapping of individual atoms in a two-dimensional dipole trap array as well as their detection while Fig. 2.5 (c) provides the front

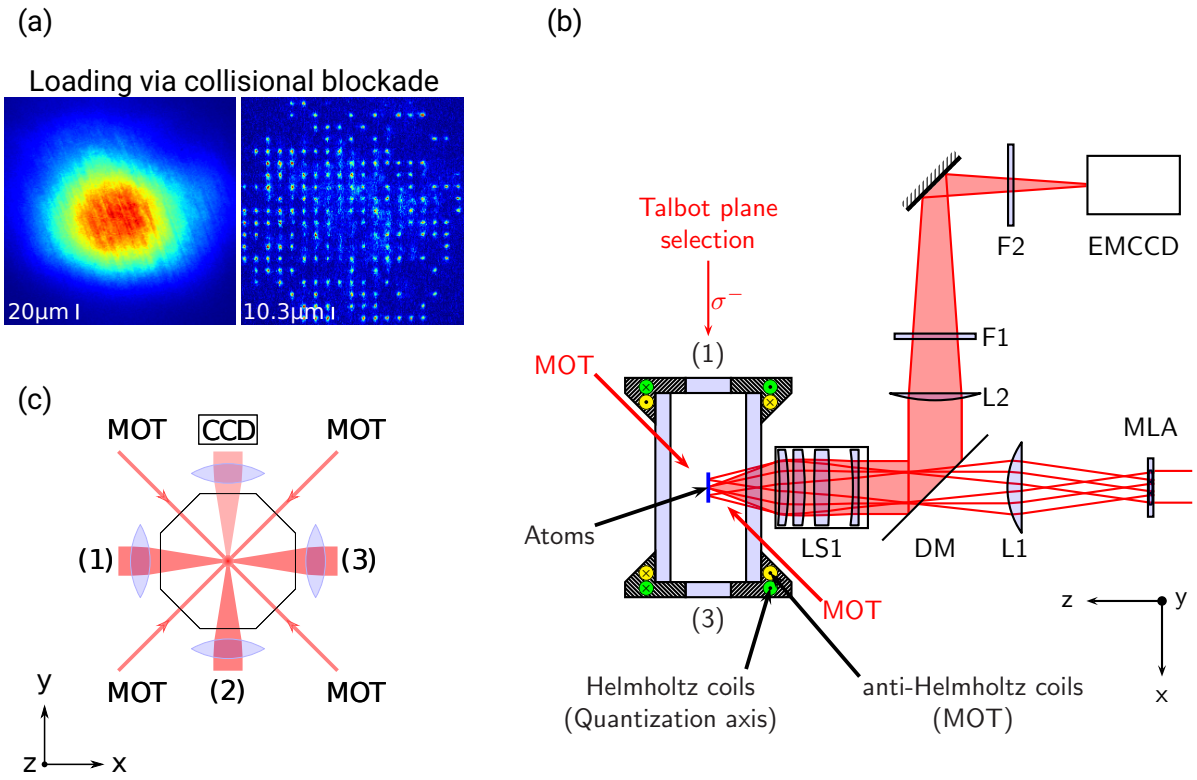

Figure 2.5.: Laser cooling, preparation and detection of individual atoms in the tweezer array. (a) At the beginning of each experimental cycle is a loading phase in which atoms from the laser cooled cloud (left) are loaded into the tweezer array and detected via fluorescence imaging (right). (b) The tweezer array is created using a microlens array (MLA) illuminated with a collimated laser beam whose focal plane is demagnified and reimaged into the vacuum chamber using an achromatic doublet (L1) and a microscope objective (LS1). Fluorescence detection is possible using the light at a wavelength of 780 nm which passes (LS1) in the inverse direction and is deflected off a dichroic mirror (DM) using an achromatic doublet (L2) for mapping the atom plane on the sensor of the EMCCD camera. The optical filters F1 and F2 are used to block disturbing light from other sources. (c) In the front perspective the other four MOT beams are indicated. An additional CCD camera is used for permanent monitoring of the laser cooled cloud. The ports (1)...(3) allow for additional incident beams. For the sake of clarity, only the pair of coils creating the MOT field with the coil axis along the z-direction and the pair of coils necessary for creation of the quantization axis along the x-direction are indicated.

perspective, respectively.
In order to prepare atoms that are sufficiently cold to be loaded into dipole traps each experimental cycle starts with a MOT phase in which the six pairwise orthogonally circular polarized beams indicated in Fig. 2.5 as ”MOT” are turned on together with the gradient field. The two pairs of counterpropagating beams within the x-y-plane cross orthogonally and are composed of cooling and repumping light while the two beams parallel to the x-z-plane consist

of cooling light only. The latter have an incident angle with respect to the z-axis of about 42°. During this phase of typically one to a few seconds the detuning of the cooling laser is chosen to be $\Delta = 2\pi \cdot (-9.6\,\mathrm{MHz})$. Thereafter, the magnetic field is turned off which leads to the expansion of the atom cloud and further cooling below the Doppler limit due to the effect of polarization gradients during a time of about 20 ms. In this period, the detuning is increased to $\Delta = 2\pi \cdot (-52\,\mathrm{MHz})$ which is the experimentally determined optimum leading to a temperature of the atomic ensemble after the optical molasses of typically 5 µK [67]. This is sufficiently low to initiate the loading process into the dipole traps.
As indicated in Fig. 2.5 the trap array is created by a laser beam illuminating the microlens array whose focal plane is reimaged into the vacuum chamber onto the position of the atom cloud using an achromatic doublet L1 and a microscope objective LS1. Due to the high density of the thermal atom cloud the dipole force continuously attracts atoms into the traps. As comprehensively discussed in [67] light-induced collisions can be exploited in the present experimental setup leading to sub-poissonian occupation statistics due to collisional blockade [79, 80]. In this case, loading of more than one atom per site is suppressed. With the MOT laser field still turned on the number of atoms N in one dipole trap during the loading phase is guided by the differential equation

$$\frac{d}{dt}N = R - \gamma N - \beta_1' \frac{N(N-1)}{2} - 2\beta_2' \frac{N(N-1)}{2} \tag{2.27}$$

as detailed in [81]. Assuming a loading rate of R and a loss rate of γ due to photon scattering and scattering of atoms with the background gas this equation also considers losses due to light assisted collisions of one (β_1') or both (β_2') atoms. Following the analysis in [82] the volume of the effective trap potential

$$V_{\mathrm{eff}} = \pi w_0^2 z_{\mathrm{R}} \ln\left(\frac{1}{1-\eta}\right)\sqrt{\frac{\eta}{1-\eta}} = \frac{\pi^2}{\lambda} w_0^4 \ln\left(\frac{1}{1-\eta}\right)\sqrt{\frac{\eta}{1-\eta}} \tag{2.28}$$

can be approximated via an cylindrical shape having the radius of one beam waist w_0 and a width of the Rayleigh range z_{R} while $\eta = \frac{k_{\mathrm{B}}T}{|U_0|}$ denotes the ratio between atom temperature and trap depth. According to [80, 82] the total atom loss rate $\beta' = \beta_1' + \beta_2'$ scales as $\beta' \propto 1/V_{\mathrm{eff}} \propto 1/w_0^4$. Monte Carlo simulations of the dynamics described by equation 2.27 can be used to show that high values of β' are key in reaching the limit of collisional blockade [67, 80] where finally either one or no atom remains in the dipole trap after the loading process. In the present setup with a wavelength of the trapping laser $\lambda = 797\,\mathrm{nm}$ and a typical trap waist $w_0 = 1.45\,\mu\mathrm{m}$ the two-body loss rate of $\beta_2' \approx 610\,\mathrm{s}^{-1}$ can be calculated leading to β' being well within the loading regime governed by collisional blockade [57, 67].
In the interest of obtaining these waists on the order of a single micrometer within the chamber the microscope objective (LS) has a high numerical aperture of $NA = 0.25(2)$ and an effective focal length of $f_{\mathrm{LS1}} = 37.5(10)\,\mathrm{mm}$. Together with the effective focal length $f_{\mathrm{L1}} = 400\,\mathrm{mm}$ of the achromatic doublet (L1) this results in a magnification of the focal plane of the microlens array by $M = f_{\mathrm{LS1}}/f_{\mathrm{L1}} = 0.094(3)$.

Talbot-plane selection

As discussed in Section 2.1.2 the periodic alignment of commercially available standard microlens arrays leads to the formation of a Talbot carpet due to interference when using coherent light for illumination. The self-acting loading of atoms in more than one plane in this multi-layer

structure is beneficial when aiming for creation of three-dimensional trapping geometries but is a source of disturbing light during fluorescence detection without a proper plane-selective implementation. This work focuses on large-scale two-dimensional configurations and, as a consequence, makes use of a mechanism for plane selection which discards atoms loaded in unused trap layers. That is why the loading sequence is succeeded by a laser pulse of roughly 1 ms resonant to the cooling transition $|5S_{1/2}, F = 3\rangle \rightarrow |5P_{3/2}, F = 4\rangle$ as indicated in Fig. 2.5 (b). In order to prevent heating and subsequent loss of atoms in the layer selected to work with that one is covered by a shadow from a thin wire within the beam that is mapped into the respective plane. In order to include atoms in the $|5S_{1/2}, F = 2\rangle$ ground state into the selection process the repumping light at $|5S_{1/2}, F = 2\rangle \rightarrow |5P_{3/2}, F = 3\rangle$ is illuminated synchronously.

Fluorescence detection of individual atoms

In addition to producing tightly focused dipole traps the high numerical aperture of LS1 also enables site-resolved detection of single-atom fluorescence. In the same fashion as LS1 and L1 reimage the focal plane of the microlens array into the vacuum chamber LS1 an achromatic doublet (L2) with an effective focal length of $f_{\mathrm{L2}} = 750\,\mathrm{mm}$ maps the array plane onto the sensor of an EMCCD camera (iXon DV887DCS-BV, Andor). Considering the solid angle covered by the numerical aperture of the microscope objective about 2 % of the light emitted isotropically by the atoms during fluorescence detection is collected. As depicted in Fig. 2.5 (b), a dichroic mirror (DM) (FDi03-R785, Semrock) is utilized which reflects fluorescence light at 780 nm to more than 95 % while being transmissive for counterpropagating dipole trap light at 797 nm. Additional filters (F1 and F2) account for the suppression of light that differs from the detection wavelength. While fluorescence is continuously created during the MOT phase (Fig. 2.5 (a, left)) the same laser beams are switched on for a typical exposure time of 50 ms to 75 ms in order to obtain a site-resolved image as Fig. 2.5 (a, right) with a detection fidelity better than 99 %.

State preparation

Dependent on the specific experiment different basis states for quantum operations are involved in the measurements presented in this thesis. In order to reach a profound starting point optical pumping can be utilized to prepare the atoms in a well-defined initial state. A level scheme which gives an overview of the involved hyperfine states is depicted in Fig. A.1. Initialization into $|5S_{1/2}, F = 2\rangle$ can be achieved by using the cooling laser which successively excites atoms in the $|5S_{1/2}, F = 3\rangle$-level to provoke spontaneous emission into $|5S_{1/2}, F = 2\rangle$. In turn, preparation into $|5S_{1/2}, F = 3\rangle$ results from illumination by the repumping light. Utilizing appropriately polarized light initialization to different Zeeman sublevels is also at hand. In combination with the repumping light circular polarization ($\sigma^{\pm}$) resonant to $|5S_{1/2}, F = 3\rangle \rightarrow |5P_{3/2}, F = 3\rangle$ leads to occupation of $|5S_{1/2}, F = 3, m_F = \pm 3\rangle$ while linearly polarized (π) light populates $|5S_{1/2}, F = 3, m_F = 0\rangle$ due to the selection rule for dipole transitions.

State-selective detection

The detection of the internal atomic state is implemented via a state-selective removal scheme. For this purpose, a laser beam with resonant light to the $|5S_{1/2}, F = 3\rangle \rightarrow |5P_{3/2}, F = 4\rangle$ cooling transition from direction (3) in Fig. 2.5 (c) is utilized. This discards atoms in state $|5S_{1/2}, F = 3\rangle$

so that the remaining population in $|5S_{1/2}, F = 2\rangle$ can be determined in a subsequent fluorescence detection stage.

Quantization axis

For experiments relying on coherent operations, clearly-specified and energetically resolvable basis states are necessary in order to reach a profound initial situation. This requires a well-defined quantization axis which is provided in the present setup through coils in Helmholtz configuration as indicated in Fig. 2.5 (b). For a typical current of $I_\mathrm{q} = 2\,\mathrm{A}$ they create a field of $B_\mathrm{x} = 283\,\mu\mathrm{T}$ along the x-direction. This breaks the degeneracy of the Zeeman sublevels in the hyperfine structure due to the interaction of the interatomic spins with the external magnetic field. As discussed in [83], the Hamilton operator describing this effect can be written in terms of the electron spin $\hat{S}_x$, the electron orbital angular momentum $\hat{L}_x$, the spin of the nucleus $\hat{I}_x$ as well as the respective Landé factors (g_S, g_L, g_I) and is given by

$$\hat{H}_\mathrm{B} = \frac{\mu_\mathrm{B}}{\hbar}\left(g_\mathrm{S}\hat{S}_x + g_\mathrm{L}\hat{L}_x + g_\mathrm{I}\hat{I}_x\right) B_\mathrm{x} \tag{2.29}$$

for a magnetic field along the x-axis where μ_B denotes the Bohr magneton.
In case of a weak magnetic field B_x, i.e. $g_\mathrm{J}\mu_\mathrm{B}B_\mathrm{x} < A_\mathrm{J}$, the nuclear spin I and the electronic angular momentum J remain strongly coupled and the hyperfine splitting characterized by the magnetic hyperfine structure constant A_J is the dominant effect. In this regime, the energy shift ΔE_{m_F} of each Zeeman sublevel m_F due to the magnetic field can be well approximated [84] via

$$\Delta E_{m_\mathrm{F}} = g_\mathrm{F}\mu_\mathrm{B}m_\mathrm{F}B_\mathrm{x} \tag{2.30}$$

with the hyperfine Landé g-factor g_F that is easily calculated via

$$g_\mathrm{F} = g_\mathrm{J} \cdot \frac{F\cdot(F+1) - I\cdot(I+1) + J\cdot(J+1)}{2\cdot F\cdot(F+1)} \tag{2.31}$$

$$g_\mathrm{J} = \frac{3}{2} + \frac{(S+1)\cdot S - L\cdot(L+1)}{2J\cdot(J+1)} \tag{2.32}$$

using the approximation $g_\mathrm{S} \approx 2$ and $g_\mathrm{L} \approx 1$. For an intermediate field strength and higher accuracy, calculations are far more difficult except in the case $J = 1/2$ which applies to the hyperfine ground states $F = I \pm 1/2$. In this situation, the Breit-Rabi formula

$$\Delta E_{J=1/2,m_\mathrm{F}} = -\frac{\Delta E_\mathrm{hfs}}{2(2I+1)} + g_\mathrm{I}\mu_\mathrm{B}m_\mathrm{F}B_\mathrm{x} \pm \frac{\Delta E_\mathrm{hfs}}{2}\left(1 + \frac{4m_\mathrm{F}x}{2I+1} + x^2\right)^{1/2} \tag{2.33}$$

holds which also considers second-order corrections for the shift $\Delta E_{J=1/2,m_\mathrm{F}}$ of the hyperfine level m_F with respect to the fine structure [83, 85] using the sign, respectively, and x defined as

$$x = \frac{(g_\mathrm{J} - g_\mathrm{I})\mu_\mathrm{B}B_\mathrm{x}}{\Delta E_\mathrm{hfs}}. \tag{2.34}$$

The ground state energy splitting in zero magnetic field $\Delta E_\mathrm{hfs} = \hbar\Delta_\mathrm{hfs}$ can be taken from Table A.1 together with more accurate values for the Landé g-factors retrieved from measurements. For the typical quantization field strength of $B_\mathrm{x} = 283\,\mu\mathrm{T}$ equation 2.33 yields $-1.316\,\mathrm{MHz}\cdot h$ for $|5S_{1/2}, F = 3, m_F = -1\rangle$ and $5.2\,\mathrm{kHz}\cdot h$ for $|5S_{1/2}, F = 3, m_F = 0\rangle$ while for the latter equation 2.30 calculates to zero.

2.6. Rydberg interactions

Excitation into Rydberg states turns ground state alkali atoms which are typically on the order of subnanometer in size into comparably giant entities that can reach radii on the micrometer scale. In this case, the probability density of the valence electron is far off the positively charged core and the fully filled electron shells. Due to this drastic increase, Rydberg atoms obtain exaggerated state-dependent properties making them extraordinary interesting study objects and, at the same time, versatile tools in research. Additionally, simply via selection of the Rydberg state one has already a wide range of possible settings to tune the experimental parameters. This flexibility leads to many applications in the field of quantum information and quantum metrology.
With respect to quantum simulation and quantum computation, especially the strong interaction between Rydberg atoms is highly regarded [30, 46, 86–88]. They can be exploited in large ensembles comprising more than hundred atoms which form a single "superatom" [89] as well as on an individual atom level. In recent experiments on quantum magnetism it was already possible to study dynamics of up to 51 atoms in 1D [90] and 49 atoms in 2D using an Ising-type implementation in tweezer arrays which becomes infeasible to simulate on a classical computer [91]. In addition, this allows for analysis of antiferromagnetic interaction [49] and critical dynamics of quantum phase transitions [51].
Moreover, Rydberg interactions enable the implementation of two-qubit gates by now. This has been shown as a logical operation between two atomic qubits [41] but also in the realization of a photon-photon gate [92], recently, which finds its application in quantum communication and networking.
Another feature that is characteristic for Rydberg atoms is their large polarizability. This makes them strongly sensitive to external electric fields and can not only be exploited in order to tune the interaction strength [93] via applying a field on purpose but also allows for characterization of the field itself [94, 95]. It is natural that many more possible applications based on Rydberg atoms exist in quantum science. A detailed review on a multitude of topical ones is given in [45].
Rydberg physics and its basics are treated in great detail in literature and the reference work [96] provides a profound introduction. The following sections discuss the fundamental properties of Rydberg atoms and relates them to the topic of this work. It is inspired by [97] and [98] while the calculations of the Rydberg atom wavefunctions and interaction potentials use the ARC library which is freely accessible [99].

2.6.1. Properties of Rydberg atoms

As alkali atoms only have one electron in the outer-most shell they can be regarded hydrogen-like to good approximation. Therefore, the potential energy E_{nLJ} follows the same scaling with the principal quantum number n as for this easier accessible system

$$E_{nLJ} = -\frac{hcRy^*}{(n-\delta_{nLJ})^2}. \tag{2.35}$$

In order to account for the difference, however, necessitates the introduction of a modified Rydberg constant

$$Ry^* = \frac{Ry_\infty}{1 + m_\mathrm{e}/m_\mathrm{c}} \tag{2.36}$$

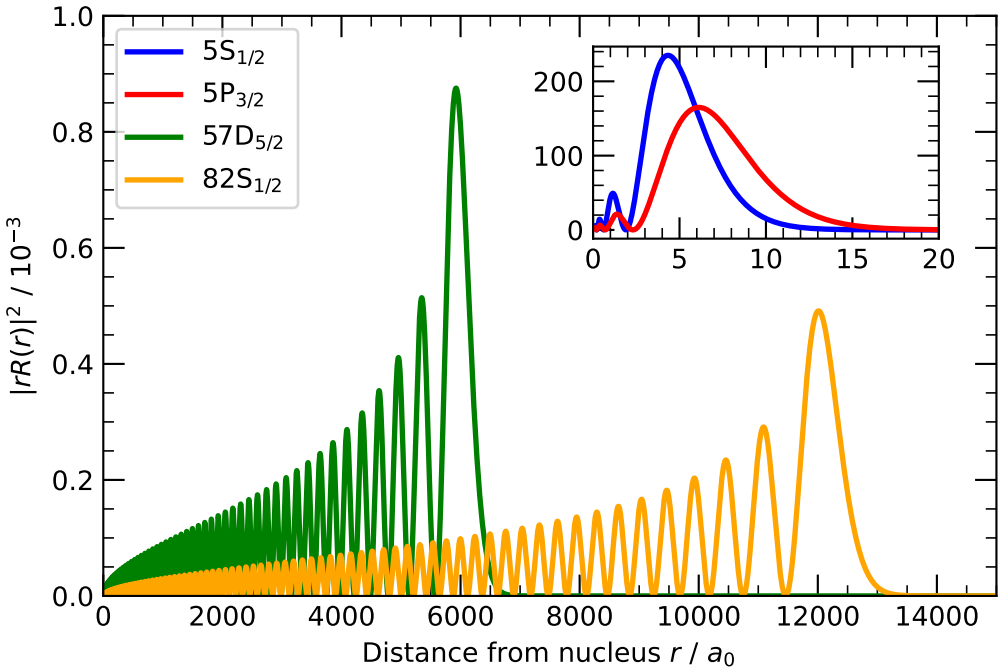

Figure 2.6.: Probability density of the valence electron in scaled units. The distribution for different states reflects typical quadratic scaling of the electron orbit radius with n and the enormous increase in size of Rydberg-excited atoms. While the excitation along the D2 line (inset) only has a small impact on the atomic size Rydberg-excited atoms are several orders of magnitude larger as shown in the example of $|57D_{5/2}\rangle$ and $|82S_{1/2}\rangle$.

which considers the electron-core mass ratio and a quantum defect

$$\delta_{nLJ} = \delta_0 + \frac{\delta_2}{(n-\delta_0)^2} + \frac{\delta_4}{(n-\delta_0)^4} + \frac{\delta_6}{(n-\delta_0)^6} + \dots \tag{2.37}$$

with experimentally obtained polynomial coefficients $\delta_{0,2,4...}$ compared to the standard Rydberg formula. These modifications regard the discrepancies between the Coulomb potential of a hydrogen-core and the factual field felt by the Rydberg electron that results from the interaction between the valence electron and all the other electrons closer to the core. This interaction has a minor effect for large angular momenta L, however, should be considered for the low angular momentum states $L \leq 3$ as used in the context of this work.
One of the characteristic properties Rydberg atoms inherit from the hydrogen atom is the quadratic scaling of the electron orbit radius. This results in a massively increasing atom size for large n leading to all the interesting properties which makes them attractive objects of study. This scaling is illustrated in Fig. 2.6 which depicts the electron probability density for a selection of Rydberg states covered in this thesis. The inset shows this distribution for the ground and excited state of the D_2 transition. While for the lower lying states the electron radius is constrained to a few Bohr radii a_0 this increases to several thousands for the Rydberg-excited electrons. The scalings of some other characteristics with n are given in Table 2.2. One

Property	Notation	Scaling
Binding energy	E_n	n^{-2}
Neighboring level spacing	$E_{n+1} - E_n$	n^{-3}
Electron orbit radius	$\langle r \rangle$	n^2
Radiative lifetime	τ	$n^3 \dots n^5$
Transition dipole matrix element	$\langle 5P \vert \hat{\boldsymbol{d}} \vert r \rangle$	$n^{-3/2}$
Polarizability	α	n^7
Resonant dipole-dipole interaction	C_3	n^4
van der Waals interaction coefficient	C_6	n^{11}

Table 2.2.: Scaling of selected properties of Rydberg atoms with the principal quantum number n.

of these quantities is the lifetime which will be discussed in the following section in more detail.

Lifetime of Rydberg-excited states

One of the many special properties of Rydberg atoms is the comparably long lifetime of the exited state. The main decay channels are spontaneous radiative decay and transitions induced by black-body radiation (BBR). Therefore, the effective lifetime τ_{eff} can be written in terms of both contributions:

$$\tau_{\text{eff}} = (\Gamma_0 + \Gamma_{\text{BBR}})^{-1} \tag{2.38}$$

with the rate for radiative decay Γ_0 to lower lying states and the black-body decay Γ_{BBR}. The former is given via

$$\Gamma_0 = \sum_{n'L', E_{n'L'} < E_{nL}} A(nL \to n'L') \tag{2.39}$$

with the Einstein-A coefficients $A(nL \to n'L')$ for transitions from a state with quantum numbers nL to an $n'L'$ state while the latter can be written similarly

$$\Gamma_{\text{BBR}} = \sum_{n'} A(nL \to n'L') \frac{1}{\exp(\omega_{nn'}/k_{\text{B}}T) - 1} \tag{2.40}$$

using the Planck temperature T for the mode at the transition frequency $\omega_{nn'}$. As the Einstein coefficients depend on the radial matrix elements of the electric dipole transition this reduces the lifetime calculation to the evaluation of these.
For the $82S_{1/2}$ state this calculation yields $\tau_{\text{eff}} = 217\,\mu\text{s}$ which is more than 8000 times the lifetime of the excited state $5P_{3/2}$ (see Table A.1) which is used for instance during the fluorescence imaging. This long lifetime is essential for the detection method used to determine Rydberg excitation in this thesis as will be discussed in Chapter 4. Further details on the calculation of the lifetime including values for other alkali-metal species can be found in [100].

2.6.2. Rydberg atom interactions

A key motivation to work with Rydberg states in the present experimental platform is their strong interactions at micrometer length scale where ground-state atoms can be seen as independent systems. Due to the large separation between the positively charged core and

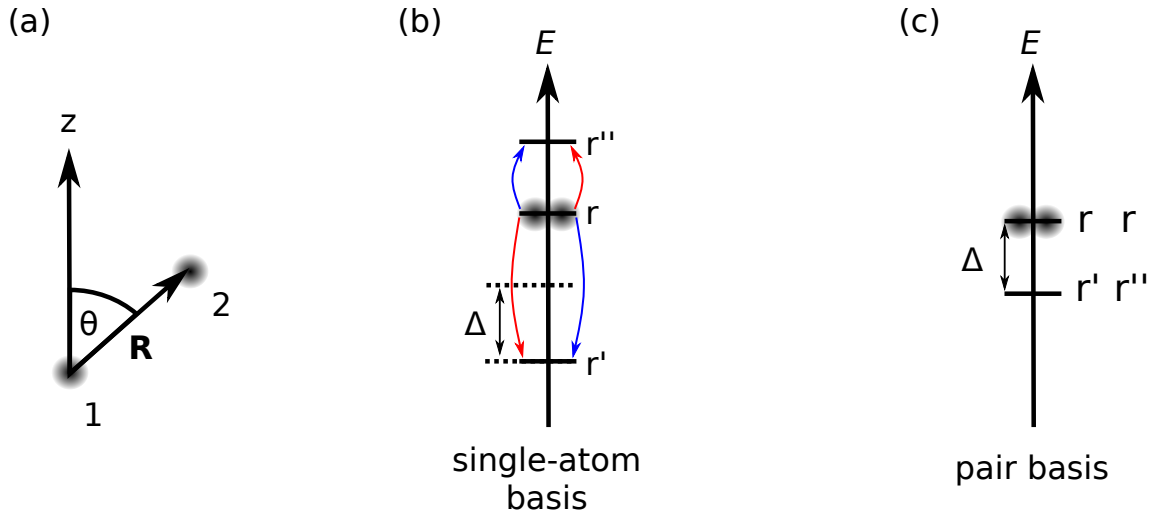

Figure 2.7.: Interacting Rydberg atoms via dipole-dipole coupling. (a) When two atoms separated by $\boldsymbol{R}$ in an angle θ relative to the quantization axis z (b) are excited into a Rydberg state $|r\rangle$ their states couple via dipole-dipole interaction with the state-dependent detuning Δ. (c) In the pair state basis one can easily identify the state which has the lowest energy difference to $|rr\rangle$ constituting the most significant coupling channel.

the single electron in the outer shell, a pair of Rydberg-excited atoms can be regarded as two interacting dipoles with an interaction potential given by

$$V_{\text{int}}(\boldsymbol{R}) = \frac{1}{4\pi\epsilon_0}\left(\frac{\hat{\boldsymbol{d}}_{\boldsymbol{1}}\cdot\hat{\boldsymbol{d}}_{\boldsymbol{2}}}{R^3} - \frac{3(\hat{\boldsymbol{d}}_{\boldsymbol{1}}\cdot\boldsymbol{R})(\hat{\boldsymbol{d}}_{\boldsymbol{2}}\cdot\boldsymbol{R})}{R^5}\right) \tag{2.41}$$

using the electric dipole moment operators $\hat{\boldsymbol{d}}_{\boldsymbol{1}}$ and $\hat{\boldsymbol{d}}_{\boldsymbol{2}}$ for both atoms and their distance vector $\boldsymbol{R}$ with length $R = |\boldsymbol{R}|$. This is illustrated in Fig. 2.7 (a) for two atoms separated by $\boldsymbol{R}$ in a configuration with the quantization axis defined along z. Assuming the two Rydberg atoms in the same initial state $|r\rangle$ as indicated in Fig. 2.7 (b) this situation can also be treated in the pair basis $|rr\rangle = |r\rangle \otimes |r\rangle$ (Fig. 2.7 (c)). In principle, all dipole-dipole coupled Rydberg states need to be included in a comprehensive treatment diagonalizing the full Hamilton operator of the system.
For a qualitative understanding one can consider a simplified situation with $\Theta = 0$ and where only a single transition channel to the level $|r'r''\rangle$ which is energetically closest with an energy difference of $\Delta = E_{r'} + E_{r''} - 2E_r$ to the pair state $|rr\rangle$ is taken into account. The interaction Hamilton operator in the basis $\{|rr\rangle, |r'r''\rangle\}$ can be written as

$$\hat{H} = \begin{pmatrix} 0 & C_3/R^3 \\ C_3/R^3 & \Delta \end{pmatrix} \tag{2.42}$$

with the interaction coefficient $C_3 \propto n^4$. Obtaining the eigenvalues

$$E_\pm = \frac{\Delta \pm \sqrt{\Delta^2 + 4C_3^2/R^6}}{2} \tag{2.43}$$

through diagonalization one finds the two different regimes resulting from the strong dependence on the interatomic distance R:

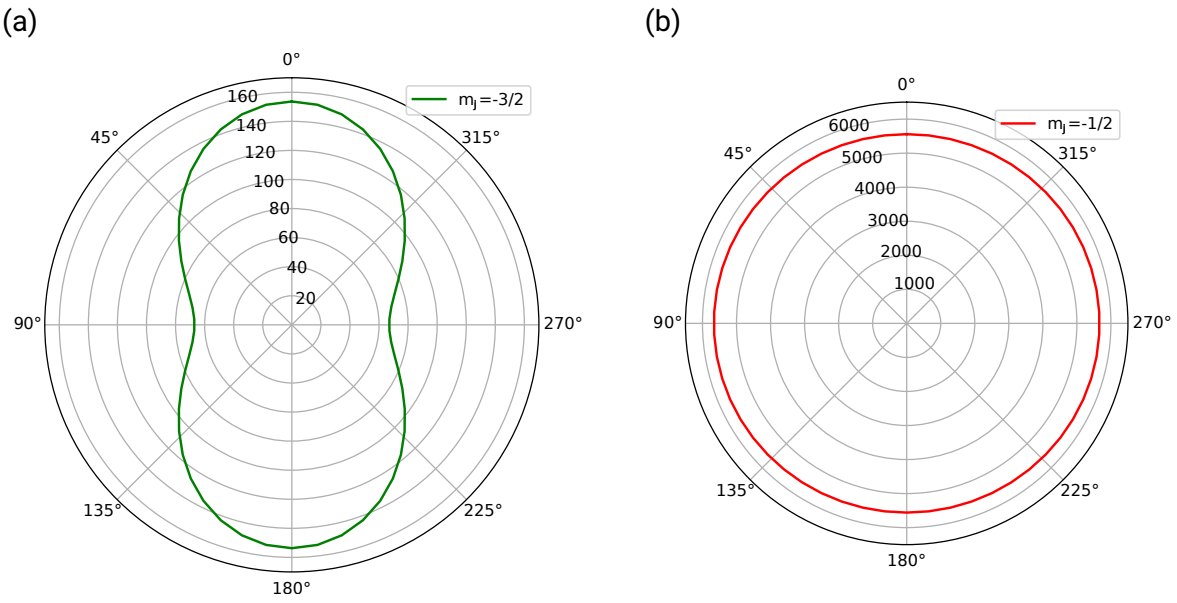

Figure 2.8.: Angular dependence of the van der Waals dispersion coefficient for two selected Rydberg states given in units of $h \cdot$ GHz µm^6. (a) While the $|57\mathrm{D}_{5/2}, m_\mathrm{J} = -3/2\rangle \otimes |57\mathrm{D}_{5/2}, m_\mathrm{J} = -3/2\rangle$ pair state shows a strong angular dependence on the angle Θ between $\boldsymbol{R}$ and the quantization axis (b) this is negligible for $|82\mathrm{S}_{1/2}, m_\mathrm{J} = -1/2\rangle \otimes |82\mathrm{S}_{1/2}, m_\mathrm{J} = -1/2\rangle$ with zero orbital angular momentum.

- **Resonant dipole-dipole interaction ($C_3/R^3 \gg \Delta$)**
  In case of Δ being negligible the eigenenergies scale as $E_\pm \propto \pm C_3/R^3$. This is typically the case for atoms which are close to each other but can also result from vanishing Δ at a Förster resonance [93, 101] or in the case of excitation transfer [47].

- **Van der Waals type interaction ($C_3/R^3 \ll \Delta$)**
  If Δ dominates, the interaction only accounts for a perturbation on the bare states and the eigenvalues in equation 2.43 exhibit a van der Waals type interaction potential $E_\pm \propto \pm C_6/R^6$ with the dispersion coefficient C_6 defined as $C_6 = C_3^2/\Delta$. This is characteristic for a situation of large interatomic distance R. As a result from the n^4-scaling of C_3 and the additional dependence of the energy difference between the states on the principal quantum number $\Delta \propto n^{-3}$, the dispersion coefficient shows the very strong scaling $C_6 \propto n^{11}$.

The transition point from van der Waals type to dipole-dipole interaction is defined as $R_\mathrm{vdW} = |C_6/\Delta|^{1/6}$.
For the long-range case where $R > R_\mathrm{vdW}$ one can use second-order perturbation theory to account for all dipole-coupled pair states and obtain an approximation for the dispersion coefficient $R > R_\mathrm{vdW}$ including the angular dependence on Θ [102]. This has the advantage that it can be calculated comparably fast in contrast to a diagonalization of the pair state interaction matrix. Figure 2.8 depicts calculations considering two pair states. Regarding states with $L > 0$ the interaction is highly anisotropic as illustrated in Figure 2.8 (a) for the example of $|57\mathrm{D}_{5/2}, m_\mathrm{J} = -3/2\rangle \otimes |57\mathrm{D}_{5/2}, m_\mathrm{J} = -3/2\rangle$ where C_6/h ranges from 154 GHz µm^6 for $\Theta = 0°, 180°$ to 67 GHz µm^6 for $\Theta = 90°, 270°$.

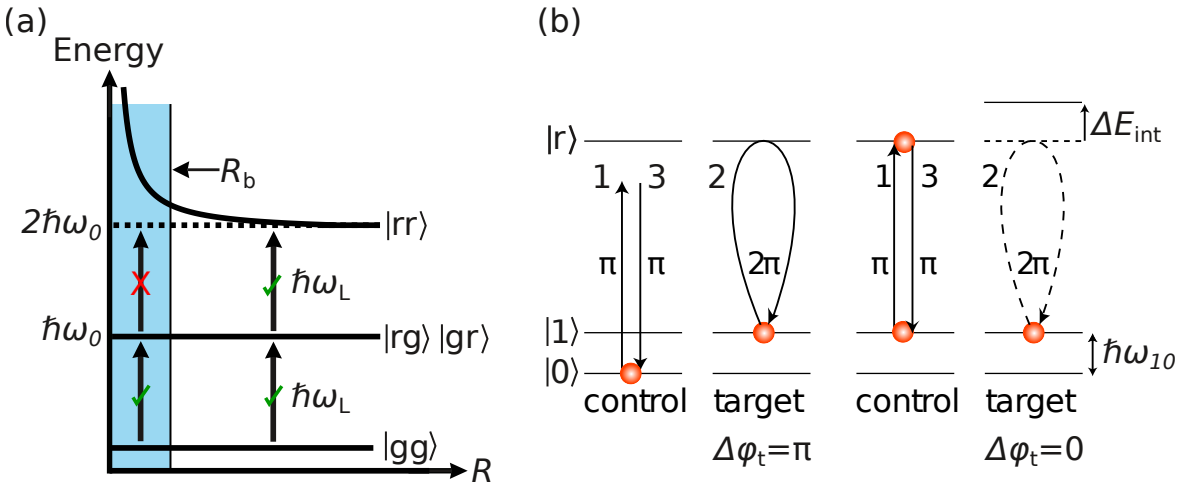

Figure 2.9.: Rydberg blockade and protocol for a controlled phase gate C_Z. (a) For large interatomic distance R, the double excited pair state energy equals the energy necessary to excite two atoms. (b) Illustration of a protocol for a phase gate which is taken from [46] with modifications. Depending on the internal state of the control atom the target atom accumulates a relative phase or not. This can be transferred into a CNOT gate using additional one quibit operations providing a full set of quantum gates.

In contrast, the pair state $|82S_{1/2}, m_J = -1/2\rangle \otimes |82S_{1/2}, m_J = -1/2\rangle$ with zero orbital angular momentum exhibits isotropic interaction to good approximation as shown in Fig. 2.8 (b). Moreover, due to the larger n the interaction potential ($C_6/h = 5559\,\text{GHz}\,\mu\text{m}^6$) is more than 30 times stronger compared to the $57D_{5/2}$ state. An alternative calculation via diagonalization of the pair-state Hamilton matrix which takes all pair states in the vicinity into consideration allows to determine $R_{\text{vdW}} = 5.2\,\mu\text{m}$ and yields $C_3/h = 63\,\text{GHz}\,\mu\text{m}^3$ and $C_6/h = 5283\,\text{GHz}\,\mu\text{m}^6$ for $\Theta = 0°$ which is slightly below the perturbative calculation for the dispersion coefficient $C_6/h = 5559\,\text{GHz}\,\mu\text{m}^6$.

Rydberg blockade

The interaction potential induced by the coupling between two atoms has interesting consequences when trying to excite two nearby atoms into the same Rydberg state $|r\rangle$ since the pair state energy depends on the interatomic distance R. This is illustrated in Fig. 2.9 together with one possible application exploiting this effect to implement a two-qubit gate. As shown in Fig. 2.9 (a) for two ground state atoms which are far apart, the same laser with frequency ω_L can excite both successively into the Rydberg state. On the contrary, if R falls below a distinct value, the shift of the double-excited state is too large in order to induce a second transition after one of the atoms has been excited. This characteristic distance is quantified by the blockade radius R_b which is defined as

$$R_b = \sqrt[6]{\frac{C_6}{\hbar\Omega}} \tag{2.44}$$

and depends on the transition Rabi frequency Ω. Assuming $\Omega = 2\pi \cdot 1\,\text{MHz}$ and $C_6/h = 5283\,\text{GHz}\,\mu\text{m}^6$ as calculated for the $82S_{1/2}$ pair state yields $R_b = 13.2\,\mu\text{m}$ which is significantly

above the tweezer pitch obtained for each of the microlens arrays used during this work. Consequently, all the presented setups allow for nearest neighbor blockaded interactions using this state.
As illustrated in Fig. 2.9 (b), the Rydberg blockade mechanism allows for implementation of a conditional logic consisting of three laser pulses with the light field coupling ground and Rydberg states. In this sequence, a control atom defines the outcome of an operation on a target atom. With respect to the present setup one can define the ^{85}Rb hyperfine ground states as qubit states $|0\rangle = |5S_{1/2}, F = 2\rangle$ and $|1\rangle = |5S_{1/2}, F = 3\rangle$ while both atoms carry one bit of information. If the control atom is in state $|0\rangle$ (left) it is not excited to the Rydberg state through the first pulse. As a result, the target atom accumulates a phase π during the execution of a full 2π rotation between $|1\rangle$ and $|r\rangle$ before the control atom is transferred back to the ground state. This state rotation is suppressed in case of blockade as the interaction energy ΔE shifts $|r\rangle$ out of resonance for the target (right). This represents a controlled phase gate and can be converted into a CNOT using additional one qubit operations. Consequently, this allows to implement a full set of quantum gates in the present setup.

2.7. Conclusion

In this chapter, an intrinsically scalable optical tweezer platform storing neutral rubidium atoms was presented and the key characteristics of the experimental apparatus were introduced. Based on the dipole force induced by appropriately far-detuned laser light, focused laser beams offer an ideal tool to trap atoms in an well-isolated environment.
Microlens arrays offer a straightforward way to adapt this approach in a greatly parallelized manner. Since arrays comprising hundreds of thousands of lenslets are already commercially available using lithographic fabrication, this technology is also highly scalable. Due to the fact that each tweezer spot is produced by focused light through a single lenslet this approach promises a high degree of stability. At the same time there is a large variety of adjustment possibilities providing short-term flexibility since all optics are outside the vacuum chamber and can be easily accessed. This allows for fast modification of the trap geometry via a replacement of the microlens array or adaption of the reimaging optics. That also includes fundamental changes in the symmetry of the tweezer pattern which is ultimately defined by the lenslet geometry and therefore provides the possibility to change for instance from quadratic to a hexagonal grid just via a replacement of the microlens array.
Using lasers which are precisely stabilized with respect to frequency as well as intensity enables laser cooling below the Doppler limit, loading of individual atoms in the tweezers using light assisted collisions, site-resolved fluorescence detection, initialization into a well-defined qubit state, and subsequent coherent operations. Thanks to the tweezer separation of typically a few micrometer, sites can be selectively addressed [54, 67] which is essential for implementation of quantum algorithms.
Essential for execution of computational logic as well as implementation of quantum simulations are controlled interactions. In the experiment, Rydberg excitations were chosen for this purpose as they provide extensive control over the coupling strength and long-range interactions. As detailed in [41], they are routinely used at interatomic distances of about 10 µm to reach Rydberg blockade. This regime is easily accessible by the present experimental platform and can be substantially undercut without considerable effort.

3. Preparation of defect-free clusters of more than 100 individually allocated atoms

Forefront experiments in quantum information, quantum simulation, or quantum metrology have the essential requirement to commence from a well-defined initial situation [26]. Naturally, this depends on the characteristics of the experimental platform which should provide precisely controlled ambient conditions with specific coupling to the environment when needed whilst ensuring optimal isolation from disturbing external influences. Additionally, this includes the preparation of the internal qubit states into a known status. Furthermore, one of the main factors is to provide a sufficiently large number of qubits at the location where they are needed whether it be for gate operations or location specific sensing. Figure 3.1 shows a typical fluorescence image obtained after loading of the array with individual atoms in this platform using light assisted collisions as discussed in Section 2.5. Due to the stochastic nature of this process the atoms are randomly distributed within the array. As a consequence, each realization yields a different initial situation for subsequent operations in every experimental cycle.

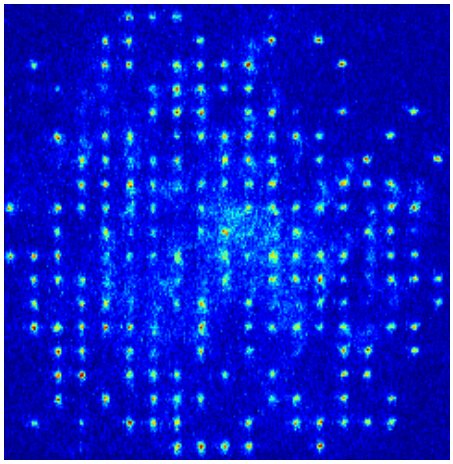

Figure 3.1.: Typical initial atom distribution after stochastic loading of the 19 × 19 workspace.

Regarding quantum computation experiments this variation is undesired in many respects. Algorithms, for instance, rely on the execution of quantum gates on a distinct set of qubits and they need to be available on demand. Additionally, using the Rydberg-blockade technique to realize a two-qubit gate requires that only the respective qubits are within the interaction region. Otherwise collective effects occur as shown in [56] which would be undefined due to cycle-by-cycle variations. The implementation of topological phases which is a promising route towards realization of a quantum error correction scheme [52, 103] in this setup also requires deterministic qubit supply. This approach creates a fault tolerant storage of information based on distribution of data within a certain group of atoms making the system immune to local disturbances. As a consequence, the atoms need to be allocated in a predefined shape within the array. That requirement also holds with respect to analog quantum simulators as they are designed to exactly mimic a specific system which is not as easy to access as the simulator. Consequently, the implementation needs to match the original in the best possible way.
Even for simple characterization and optimization measurements the possibility to allocate atoms in a specific pattern at a distinct location is highly beneficial. As each loading cycle into the array requires about 1 s this is clearly a bottleneck during data recording. Therefore, a technique which allows to allocate the atoms at a predefined area which is relevant for the current measurement and overcome the statistic loading presents a clear time benefit. That is why in the course of this thesis a technique has been realized to overcome the statistic loading [31].

Figure 3.2 illustrates schematically the implementation in the experimental platform and already shows some of the results. The principal concept of the experimental setup is depicted in Fig. 3.2 (a). After creating an array of focused-beam dipole traps from the focal spot pattern of the microlens array (MLA) the foci are reimaged into the vacuum chamber. Using an independent movable optical tweezer which is superimposed with the array beam utilizing a beam splitter allows for controlled rearrangement of the initial atom distribution created by loading from the MOT. This is realized via capturing an atom from a reservoir trap and relocate it to a different site. Repeated multiple times this transforms the initially random distribution into a predefined geometry.
In this way, assembling of arbitrary, defect-free patterns is possible as shown in Fig. 3.2 (b-d). The 10×10 cluster depicted in Fig. 3.2 (b) could eventually form one error-corrected logical qubit in a quantum-error corrected system while the ring pattern shown in Figure 3.2 (c) allows for realization of color-code schemes [104]. Based on the rearrangement of atoms, defect-free clusters comprising up to 111 atoms (Fig. 3.2 (c)) can be constructed in this setup.
In a similar way as for the present experimental platform the requirement for a deterministic qubit supply affects all neutral atom experiments working in the field of quantum information with individual atoms and there are different approaches to cope with imperfections. Therefore, the following section will first review the state of the art in preparing configurations of single atom quantum systems without defects before revealing the details of the experimental setup developed during this work. Then, the performance when synthesizing atomic clusters comprising different numbers of atoms is evaluated. As a next step, possibilities for more complex repositioning sequences are discussed before an extension to the tweezer system is presented. This makes use of the single-site addressability through the tweezer beam path and outlines options for site-selective fluorescence detection schemes. Finally, applications of the system within and beyond the scope of this thesis will be analyzed and possible improvements are outlined which can further scale up the available defect-free cluster size.

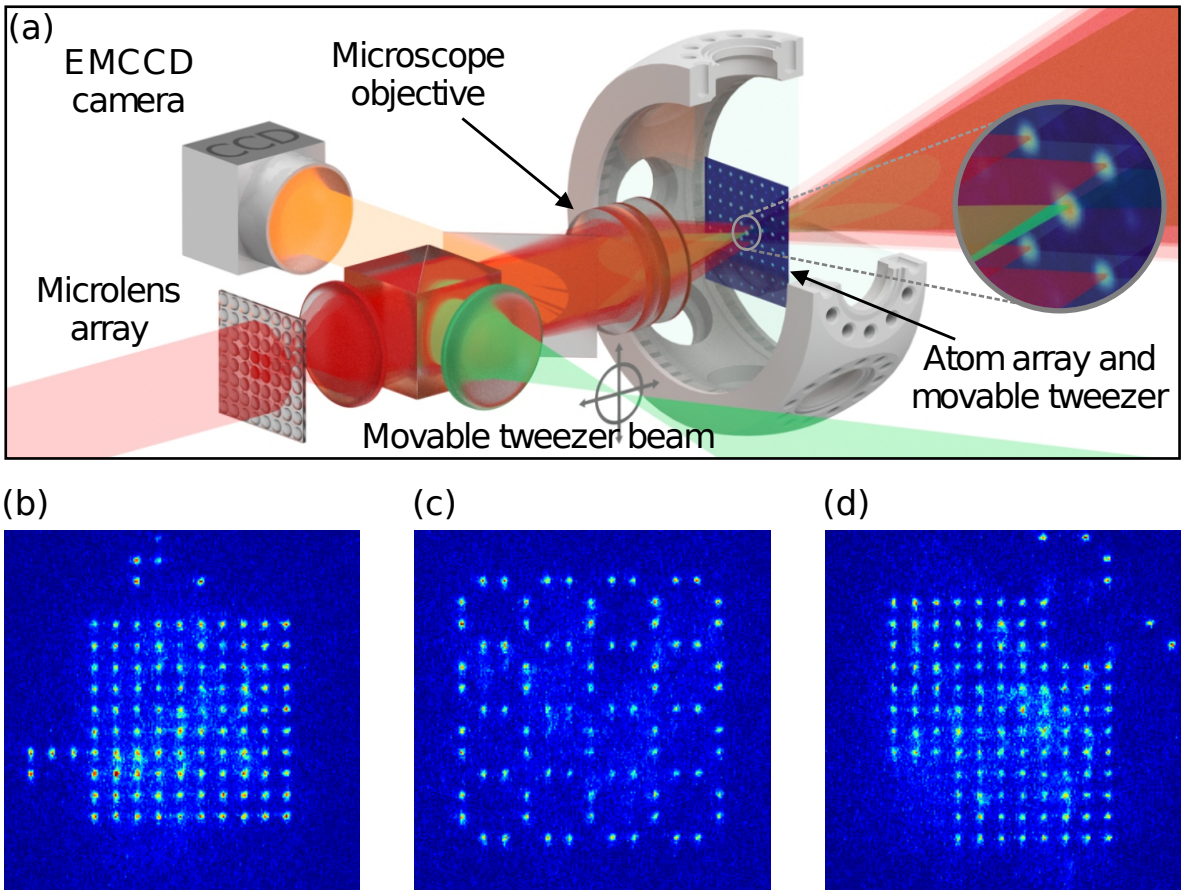

Figure 3.2.: Defect-free clusters of up to 111 atoms and experimental setup. (a) Simplified schematic of the experimental setup. Illuminating an microlens array with the trapping light and reimaging its focal plane into the vacuum chamber creates an array of optical dipole traps which is loaded with individual atoms from a MOT. An additional steerable laser beam is superposed with the light of the dipole traps on a beam splitter which creates a movable optical tweezer. The fluorescence light of trapped atoms at 780 nm which is collected with the microscope objective, separated with a dichroic mirror and imaged onto the EMCCD camera enables to determine the occupation of the trap array. From this the necessary sequence of rearrangement moves is calculated to reach the predefined pattern. This allows for construction of flexible geometries of large (b) quadratic or (c) ring-shaped patterns (d) consisting of up to 111 atoms.

3.1. State of the art in techniques to prepare defect-free configurations of individual atoms

Preparing single atoms in predefined large-scale configurations is a highly topical field of research. For setups with sub-micron spaced two-dimensional periodic potentials central areas with filling close to unity have been reported in quantum gas microscopes [30, 89, 105–109]. However, in these platforms single-site access remains challenging and rearranging of atoms has only been shown in a one-dimensional array with four atoms.
In setups with a pitch on the order of micrometers using focused laser beams for the creation of optical trapping potentials, tremendous progress in scaling the system size has been made since the first demonstration of sub-poissonian loading in an optical dipole trap at the beginning of this century [79]. Without advanced loading mechanisms the single-site preparation efficiency using light induced collisions remains typically at about 50 % [79, 80, 110–112]. In contrast, optimized schemes based on blue-detuned light during the loading sequence [32, 113, 114] reach up to 90 % filling. While this significantly raises the number of available atoms there is still demand for subsequent rearrangement in order to reach a perfectly defined initial situation for experiments.
Depending on the approach used for the generation of the tweezer arrays, this is realized in different ways: Either the successfully loaded traps are repositioned [28, 32, 35, 115] which then form the predefined pattern or an additional independent optical tweezer is used to reconfigure the distribution of the atoms within the array [29, 34].
At the point when the experiments documented in this chapter were performed (2019) the largest defect-free atom-by-atom assembled array consisted of 72 individual atoms within a two-dimensional geometry [34]. This limit could be significantly exceeded in the frame of this work which constitutes the subject of the following section.

3.2. Pathway from stochastic loading to unity filling in predefined geometries

3.2.1. Experimental setup

Figure 3.3 shows the details of the developed experimental setup. A collimated laser beam deployed by a single-mode optical fiber illuminates a microlens array with a pitch of 110 µm (MLA1, Table 2.1) whose focal plane is demagnified into the vacuum chamber using an achromatic doublet L1 with a focal length of $f_{\mathrm{L1}} = 400\,\mathrm{mm}$ and a microscope objective LS1 with an effective focal length of $f_{\mathrm{LS1}} = 37.5(10)\,\mathrm{mm}$ that has a numerical aperture of $NA = 0.25(2)$. This results in a $10.3(3)\,\mu\mathrm{m}$-pitch quadratic array of traps with beam waists of $1.45(10)\,\mu\mathrm{m}$. The trapping light is obtained from the Ti:Sa laser which is running at a wavelength of $\lambda = 797.3\,\mathrm{nm}$. This yields trap depths of $U_0/k_{\mathrm{B}} = 0.21(3)\,\mathrm{mK} \ldots 1.7(2)\,\mathrm{mK}$ within the area of a 361-site workspace of a 19×19 grid due to the Gaussian intensity profile of the beam illuminating the MLA.
The transport of atoms within the array is realized by the moving optical tweezer which is steered by a 2D acousto-optic deflector (AOD) (DTSXY-400-780.800, AA Opto Electronic). This light is slightly offset in frequency to avoid interference effects. An achromatic doublet L3 with a focal length of $f_{\mathrm{L3}} = 80\,\mathrm{mm}$ is used to focus the collimated laser beam while converting the angular deflection by the AOD into a displacement within the focal plane. This spot is reimaged

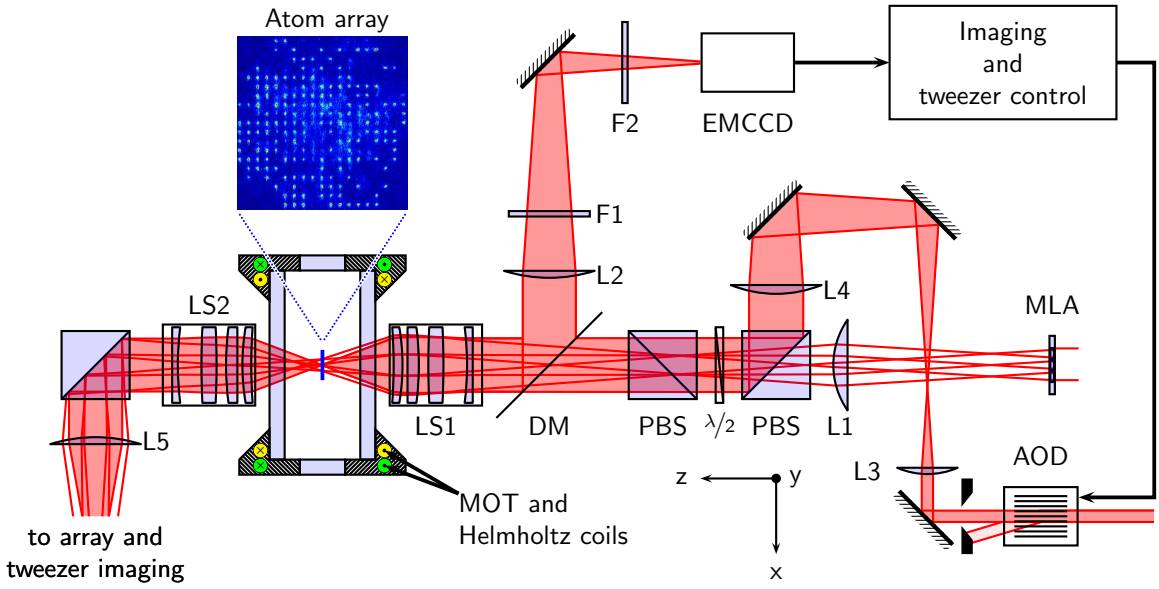

Figure 3.3.: Simplified optical setup for defect-free atom-assembly. The focal plane of a microlens array (MLA) is reimaged into the vacuum chamber using a combination of an achromatic doublet L1 and a microscope objective LS1. The initial atom distribution within the array after loading from the MOT is determined via fluorescence imaging employing LS1 and L2 which map the atom plane onto the EMCCD camera. On that basis, the tweezer control system calculates a sequence of moves to reach the target pattern. These are executed utilizing a 2D AOD to steer a laser beam which is overlapped with the array light on a polarizing beam sampler (PBS). A second microscope objective LS2 allows for monitoring the tweezer and array intensity distribution using a CCD camera.

using an achromatic doublet L4 with focal length $f_{L4} = 400\,\text{mm}$ and the same microscope objective as for the microlens generated foci after superposition with the array light via a polarizing beam sampler (PBS). The movable tweezer has a focal waist of $2.0(1)\,\mu\text{m}$ and can be overlapped with every dipole trap in the array simply by supplying the appropriate radio frequency (RF) to the deflector. The diffraction efficiency of the AOD was measured to be $> 60\,\%$ for a frequency span of about 40 MHz [116] which corresponds to an addressable region of $400\,\mu\text{m} \times 400\,\mu\text{m}$ covering more than 1500 sites in the 10.3 µm-pitch configuration. This is significantly larger than the currently addressed workspace and allows for straightforward expansion of the grid size which is limited by the available laser power at present.

Tweezer control system

The tweezer control system indicated in Fig. 3.3 consists of different soft- and hardware components which work hand in hand in order to enable the rearrangement of atoms within the array on a millisecond timescale. First of all, a camera software developed in the master thesis [116] allows for fast evaluation of the atom occupation in each trap of the array workspace. Additionally, the software provides a network interface which communicates this data to a controller server each time a rearrangement is requested.
In this case, the server program calculates the necessary moves that transfer the detected

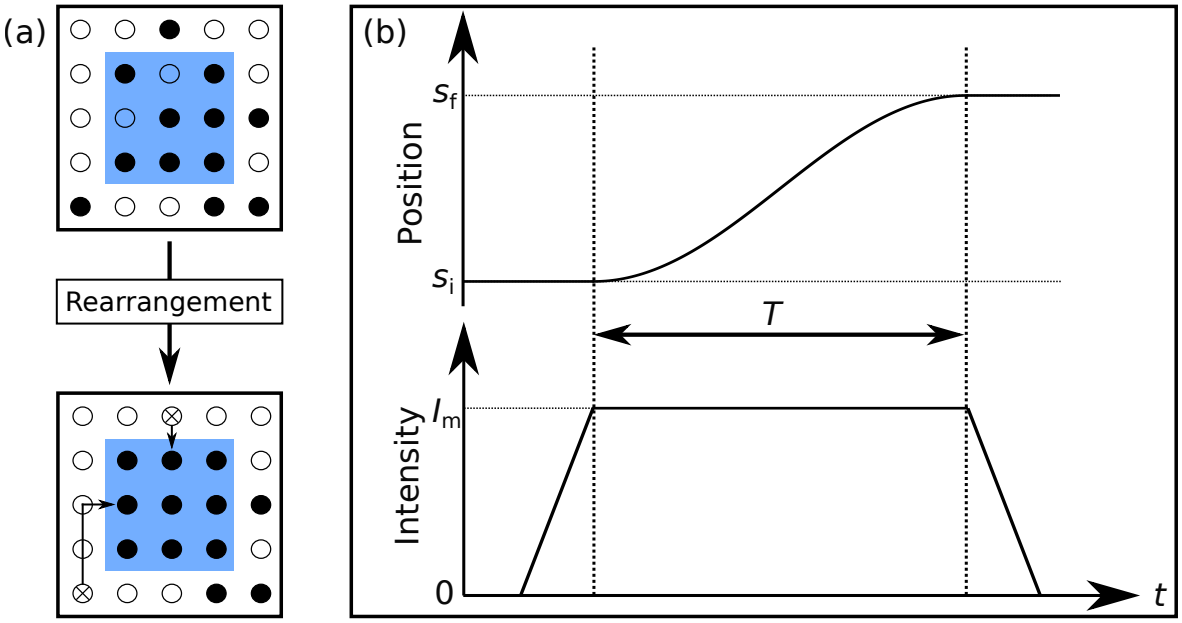

Figure 3.4.: Rearrangement sequence. (a) For each assembly cycle a target pattern (blue) is defined which shall be occupied with unity filling. The other sites serve as a reservoir with atoms to achieve this. The initial distribution of atoms in the workspace is analyzed (top) and from this a sequence of moves is calculated to fill the defects (bottom). (b) For the transport a sinusoidal position ramp is chosen to minimize heating of the atoms. Before and after each move, the intensity of the tweezer beam is linearly ramped to gently take the atom from the reservoir site and release it at the target site.

distribution of atoms into the predefined geometry. After that, this list is sent to an FPGA system (DE1-SoC, Terasic) via Ethernet. This module features general-purpose input/output ports (GPIO) which are connected to the parallel interface of two direct digital synthesis (DDS) evaluation boards (AD9915, Analog Devices) in order to set their output frequency. Each of these DDS allows to define the frequency via setting a 32-bit frequency tuning word (FTW) over the parallel port. Consequently, the FPGA system has direct control over the output frequency of the two DDS. As these provide the RF for the 2D AOD, the FPGA system can steer the tweezer beam and transport the atoms according to the calculated moves.

3.2.2. Creation of defect-free atom clusters

A typical experimental cycle starts with the MOT followed by the optical molasses phase from which individual ^{85}Rb atoms are stochastically loaded into the 361-site workspace grid utilizing collisional blockade [79, 114, 117, 118]. This provides an average number of $191(17)$ trapped individual atoms in every experimental run.
For each rearrangement cycle, the occupancy of the traps is determined by fluorescence imaging before a sequence of tweezer moves is calculated applying a heuristic algorithm to fill all vacant spots in a predefined target structure with reservoir atoms from the surrounding area. This is illustrated in Fig. 3.4 (a) in the example of a 3×3 target cluster (blue) within a 5×5 workspace. As discussed in detail in [116] the algorithm moves the atoms along the grid lines

preferring short moves over a long-distant atom transport. Usually, there are different ways to reach perfect filling and the routing calculations do not necessarily find the optimal solution. However, they are time efficient and always find a way to achieve the target pattern if there are sufficient atoms available.
Prior to the assembly, the intensity of the array traps is linearly ramped down by typically a factor of 4 resulting in $U_0/k_\mathrm{B} = 0.05(1)\,\mathrm{mK} \ldots 0.43(5)\,\mathrm{mK}$ and the rearrangement sequence is initiated. Each move consists of three stages as illustrated in Fig. 3.4 (b): First the time-dependent tweezer position $s(t) = s_\mathrm{i}$ is set to be superimposed with the source trap and kept static while the tweezer intensity is linearly increased to the maximum level I_m yielding a typical trap depth of $U_0'/k_\mathrm{B} = 0.52\,\mathrm{mK}$. As a next step, $s(t)$ is moved to the destination trap s_f following a sinusoidal shape $s(t) = s_\mathrm{f} + (s_\mathrm{i} - s_\mathrm{f})\frac{1+\cos(\pi t/T)}{2}$ with $T = \frac{s_\mathrm{f}-s_\mathrm{i}}{\bar{v}}$ being the transport duration. The latter depends on the distance while the mean velocity $\bar{v}$ is typically chosen to be $21\,\mu\mathrm{m/ms}$ at maximum. This is favorable in order to preserve adiabaticity during the transport and avoid heating [119]. Eventually, the tweezer intensity level is linearly decreased until it reaches zero releasing the atom in its new location. In this manner all moves are executed sequentially which gives an average probability for a successful atom transport of 75 %. Finally, the rearrangement cycle is completed by ramping the array light up again and taking another image to analyze the resulting structure.
In case of defects due to imperfect transport or lifetime-related atom losses, a subsequent rearrangement cycle attempts to eliminate them. This significantly enhances the probability of reaching defect-free filling of the target structures. Additionally, exploiting up to 80 consecutive rearrangement cycles a given configuration of atoms can be maintained over a course of up to 10 s continuously refilling defects that result from atom loss. In case of a 5×5 cluster $49(13)$ of 80 images contained a defect-free target structure. As discussed in more detail in [57] multiple rearrangement sequences even have a stabilizing effect regarding the atom lifetime due to laser cooling during the repetitive fluorescence imaging. An increase in the $1/e$-lifetime τ from a photon-scattering dominated value of $3(1)$ s to a value of $13(1)$ s can be observed which even exceeds the vacuum-limited lifetime reported in [120] for significantly larger detuned trapping light at a wavelength of 805 nm in the present setup.

3.2.3. Multiple rearrangements for large-scale clusters

The increase of accessible cluster size resulting from the execution of multitudinous rearrangements is presented in Fig. 3.5. By the example of assembling a target cluster comprising 10×10 atoms, Fig. 3.5 (a) shows a sequence for the repetitive rearrangement. Starting with an initially random atom distribution the images depict the full sequence of consecutive stages of the assembly process. Between each image, the trap occupation is evaluated and a sequence of moves is calculated and executed achieving defect-free filling after a total of five cycles. The whole process until the final pattern is reached takes 1.3 s.
Figure 3.5 (b) depicts the dependence of the cumulative success rates for defect-free filling of quadratic target clusters on the size of the final pattern over 15 rearrangement cylces. Up to a cluster size of 5×5 atoms, the cumulative success rate exceeds 99 %. This decreases for larger clusters due to atom losses during transport as well as atoms escaping the target structure itself which prevents complete filling in every repetition of the experiment. Nevertheless, even for the largest clusters, the cumulative success rate is still high, reaching values of 64 % for 8×8 atoms, 12 % for 9×9 atoms, and 3.1 % for 10×10 atoms. Comparing the final values of the success rates to the ones after only one rearrangement cycle the advantage resulting

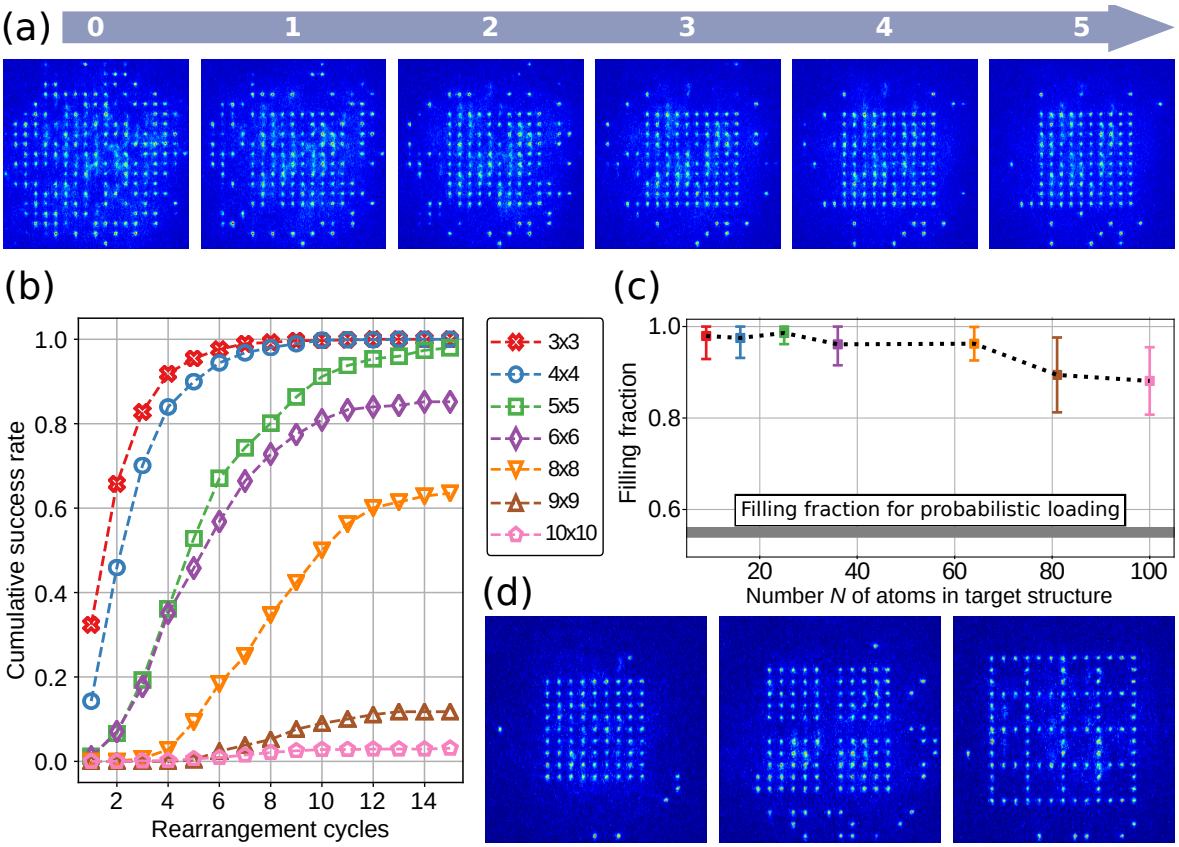

Figure 3.5.: Multiple rearrangements leading to large clusters. (a) Atom distribution during a sequence of rearrangement cycles for a 10×10 target structure. Starting from an unsorted atom array, a defect-free cluster is generated within a rearrangement sequence of 5 cycles. (b) Measured cumulative success rates of achieving defect-free quadratic clusters of different sizes. For most clusters, the final value is reached after 10 to 15 rearrangement cycles. Measured success rates are 3.1 % for 10×10 clusters, 64 % for clusters up to 64 atoms, and close to unity for clusters up to 25 atoms. (c) Maximum filling fraction observed during rearrangement runs for different cluster sizes. Error bars correspond to a 1σ interval. The thick line at 0.55 represents an upper bound to the filling fraction obtained via collisional blockade alone, i.e. the situation before the first rearrangement. (d) Various defect-free clusters obtained after multiple rearrangement cycles.

from multitudinous rearrangement cycles becomes evident: The majority of target clusters reach the final success rate after more than 10 rearrangement cycles. In this fashion, the setup provides geometries which are not accessible via stochastic loading in a practical way. When comparing the final success rate of the 10×10 cluster to the one calculated for stochastic loading of this structure through collisional blockade only, yields an enhancement of more than 10^{25}. Consequently, this approach will allow for executing experiments which demand perfect filling that would have been impossible to be realized within a feasible amount of time without this technique.
In contrast to the probability for achieving a predefined pattern within one experimental run, other publications often refer to the filling fraction [28, 29, 35]. This becomes relevant if a certain amount of defects is tolerable when executing an experiment subsequent to the rearrangement. The maximum filling fraction of the different quadratic target configurations is given in Fig. 3.5 (c). For a 10×10 atom cluster a fraction of 88(7) % is obtained while for all structures up to 8×8 atoms more than 95 % of the sites are occupied.
Figure 3.5 (d) presents a gallery of defect-free clusters each having a system size where multiple rearrangements are essential for successful assembly. With respect to quantum computation, the 9×9 cluster (left) as well as the four 5×5 clusters (middle) can be regarded as fault tolerant logical qubits each composed of many physical qubits [104].
So far, only multiple rearrangement sequences heading for creation of one specific target pattern have been demonstrated. The next section deals with further possibilities to make use of the gain in flexibility which results from the movable tweezer.

3.2.4. Extended rearrangement methods

In the previous section, multiple rearrangements have proven to be extremely vital for reaching large-scale defect-free configurations within an imperfect environment that exhibits atom loss. In this context, rearranging always aimed on the assembly of one specific predefined cluster within an experimental cycle. However, the tweezer system provides much more flexibility with respect to controlling the location of atoms within the array. The target structure, for instance, does not necessarily need to be equal for all rearrangement cycles. Additionally, the movable tweezer could also be used to clear the occupation within certain regions. Moreover, if desired, the tweezer implementation in the experiment allows for moving selected atoms from certain sites to arbitrary destination positions.
Figure 3.6 deals with these extended rearrangement procedures which have been performed within a 11×11 workspace. In Fig. 3.6 (a), the repeated reconstruction of a defect-free 3×3 cluster after intentionally emptying the target area and reloading atoms from a spatially separated reservoir is shown. This removal can also be regarded to mimic significant atom loss resulting from a measurement process as discussed in Section 2.5. Using the reservoir in this case allows to replace the lost atoms and immediately proceed with the next measurement sequence without the need for a time-consuming MOT loading phase.
Instead of rearranging the same target structure multiple times, a present configuration of atoms can also serve as a starting point for a new repositioning and be transformed into a different geometry within one experimental run. This is shown in Fig. 3.6 (b) in the example of two inverted patterns.
Finally, deterministic atom transport enables the transfer of particular atoms to specific new sites. If done adiabatically, the transfer preserves coherence as demonstrated in [55, 118] and provides a means for the redistribution of entangled sub-arrays within atom clusters in a large-scale tweezer array. In Fig. 3.6 (c) a rearrangement sequence comprising four pairs

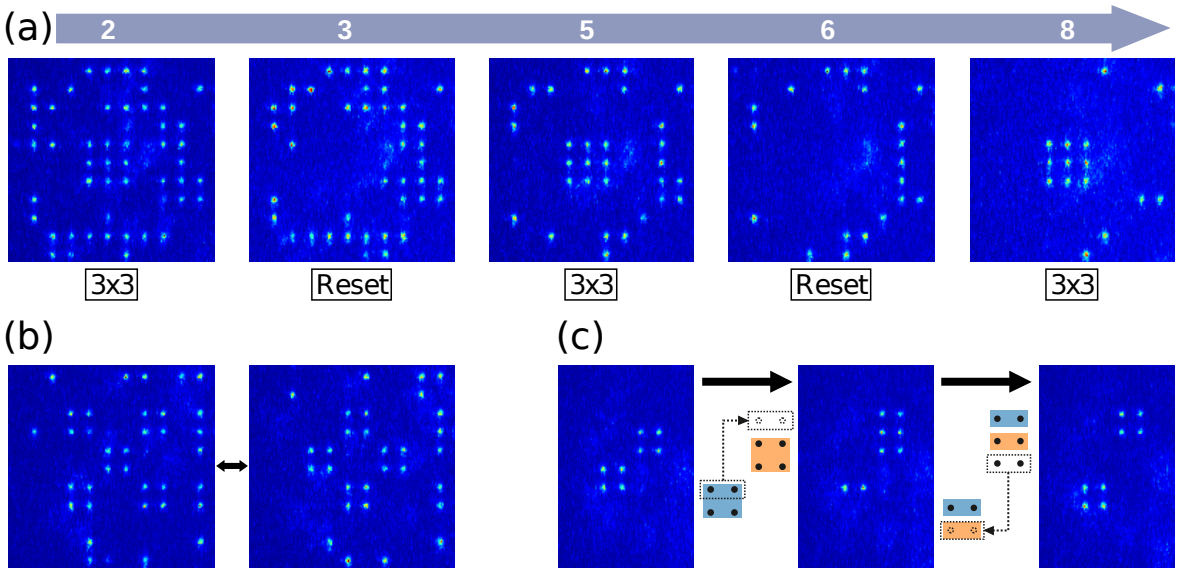

Figure 3.6.: Reloading and reordering schemes. (a) Multiple reconstruction cycles of a central 3×3 cluster are realized after deliberate atom removal using the optical tweezer. The number of feasible repetitions within one experimental run scales with the size of the reservoir array. This demonstration is based on an 11×11 workspace with 96 reservoir sites. (b) Example of the transformation (inversion) of an atom arrangement within a single experimental run. Atoms which get lost during this procedure are replaced by atoms from the surrounding reservoir. (c) Demonstration of an atom exchange between two clusters: From a stochastic initial atom distribution a defect-free structure of two 2×2 clusters is created (left). Next, the atoms are relocated so that two atoms from each of the clusters are moved into the respective other cluster (center and right). The two colors in the schematic correspond to the respective original clusters. This procedure could find its application in the distribution of entanglement [121].

of atoms is demonstrated which can be used for the redistribution of entanglement [121] between the two 2×2 atom clusters.

3.2.5. Atom rearrangement in Talbot planes: On the way to defect-free 3D geometries

Due to the Talbot effect microlens-based dipole trap arrays are intrinsically three-dimensional [68]. Even if only one plane is used there exist applications where working in a Talbot layer is advantageous [122]. Consequently, well-defined initial preparation of atoms within these planes should also be available. In order to demonstrate defect-free assembly for these configurations the microlens array as well as L1 were moved a total of 15.2 mm for the $T_{-1/2}$ plane to reach the original position of the focal plane. This approach ensures that no other optics for imaging or plane selection have to be adjusted, too. The results are depicted in Fig. 3.7. Due to the pitch of the dipole trap array $p = 10.3(3)\,\mu\text{m}$ the distance between half-integer layers illustrated in Fig. 3.7 (a) evaluates to $z_\text{T}^\star = 133(8)\,\mu\text{m}$ following equation 2.24. In this configuration, the assembly of defect-free clusters in the same fashion as implemented in the focal plane T_0 (Fig. 3.7 (b)) can the also be demonstrated within the Talbot plane $T_{-1/2}$

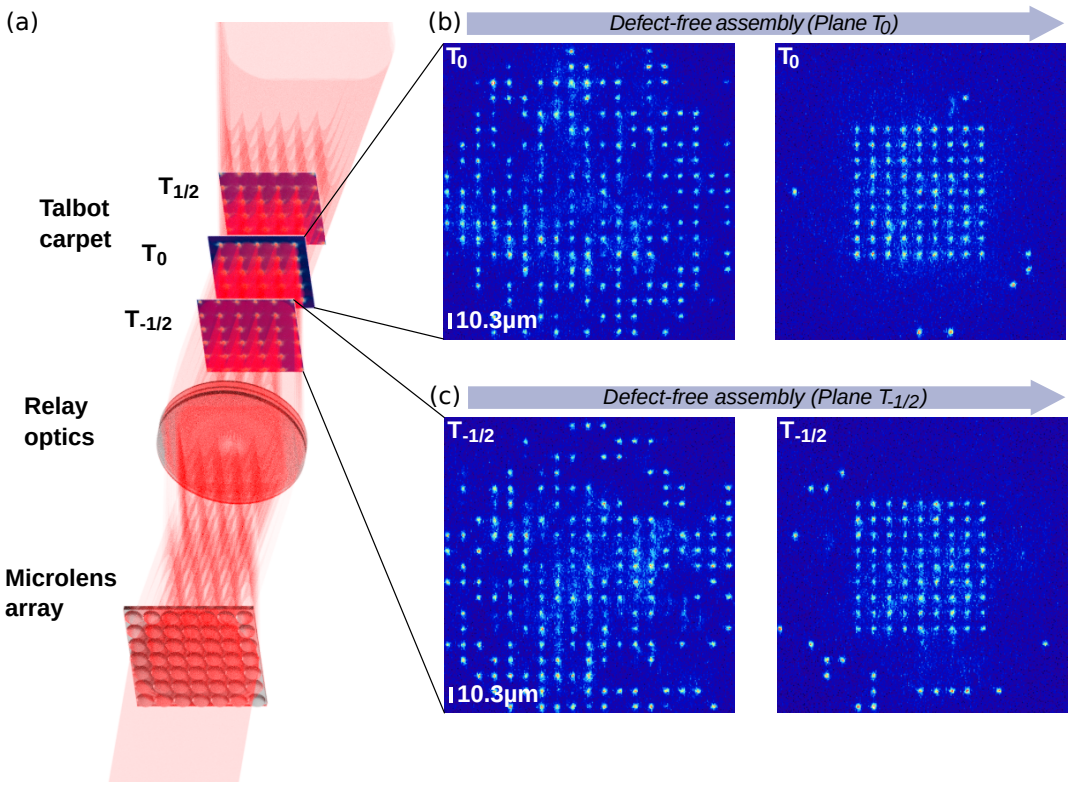

Figure 3.7.: Atom rearrangement in focal and Talbot planes. (a) Talbot carpet showing the focal plane as well as the first half-integer planes. Using the optical tweezer system allows for extension of the already routinely used defect-free cluster assembly from the focal plane (b) to the $T_{-1/2}$ Talbot plane (c) with the same performance.

as shown in Fig. 3.7 (c).
While this demonstrated the applicability of the present tweezer system in the Talbot planes, additional extensions are required to develop a fully featured three-dimensional architecture. When it comes to fluorescence detection, atoms in different planes cause disturbing light as discussed in [67]. Therefore, it would be necessary to implement a plane selective detection scheme. This could be realized using a combination of spatial light modulation for the excitation lasers and tunable lenses as utilized in [34]. Additionally, the tweezer beam focus needs to be made tunable along the optical axis. Nevertheless, these extensions can be realized with manageable effort. The following section will discuss a localized detection scheme which could be extremely vital in this case of a further extended 3D system.

3.3. Fluorescence detection on a single-site basis using the movable tweezer

The implementation of the movable tweezer has created entirely new possibilities to control the atom configuration within the array. In addition, this light path with dynamic position control at a single-microsecond timescale allows for fast site-selective addressing. This leads to a vast number of possible applications ranging from state-selective removal of atoms or spin-selective detection as demonstrated on a millisecond addressing rate in [67] to state preparation and site-selective coherent quantum operations.
Moreover, it is possible to make use of the single-site addressability with respect to fluorescence detection. As this measurement technique relies on resonant scattering processes which do not preserve the quantum state of the atom, a scalable platform greatly benefits from the capability to execute this in a localized fashion. This is analyzed within a dipole trap array with a pitch of $p = 7.0(2)$ µm using the microlens array MLA2.
As discussed in Chapter 2, the standard detection scheme involves continuous excitation of the atoms during an exposure time of typically 60 ms along the cyclic cooling transition $|5S_{1/2}, F = 3\rangle \rightarrow |5P_{3/2}, F = 4\rangle$ with simultaneous repumping. The latter takes care of atoms which decayed into $|5S_{1/2}, F = 2\rangle$ after off-resonant excitation and would otherwise not be excited anymore. This, in turn, can be used in order to implement a site-selective fluorescence detection scheme. For this purpose, the tweezer beam is superimposed before the optical fiber with laser light at $\lambda = 795$ nm driving the excitation $|5S_{1/2}, F = 2\rangle \rightarrow |5P_{1/2}, F = 3\rangle$ and thus serving as repump light. This laser is offset locked to a second laser stabilized on the $|5S_{1/2}, F = 3\rangle \rightarrow |5P_{1/2}, F = 2\rangle$ transition running an MTS stabilization [73]. The laser is intensity stabilized at a power of approximately $P \approx 100$ nW at the focus and detuned from the resonance about $\Delta = 2\pi \cdot 900$ MHz which allows for stabilization at a higher power while keeping the coupling strength in an acceptable regime. Otherwise increasing atom loss has been observed. Figure 3.8 depicts a sequence of images taken during one experimental cycle. First, atoms are stochastically loaded from the MOT (Fig. 3.8 (a)) and then rearranged into a 3×3 cluster (Fig. 3.8 (b)). For both of these images the standard detection scheme applying the cooler laser synchronously

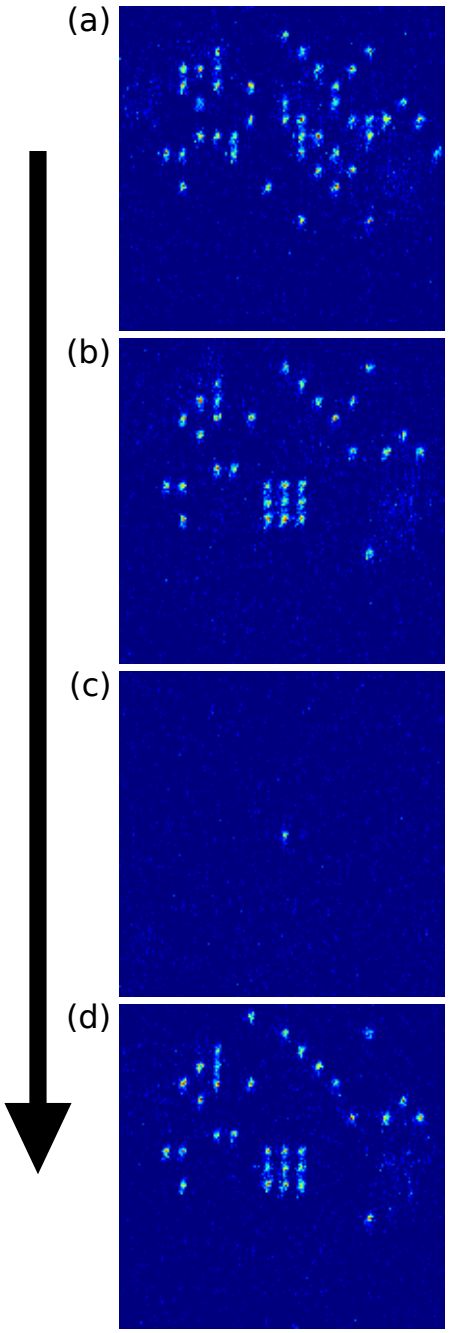

Figure 3.8.: Site-addressed fluorescence detection. See text for details.

with the regular repump beam is used to generate fluorescence. As a next step, the atoms were pumped into $|5S_{1/2}, F = 2\rangle$ applying the cooler beam for another 0.4 ms. After this duration, a local detection sequence is executed and yields Fig. 3.8 (c). During this exposure time only the cooler laser in combination with the addressing beam were turned on. Consequently, solely the atom at the addressed site is visible while the other atoms which are still present remain hidden. When returning to the standard exposure scheme it becomes evident that all atoms are still present in the array. This is demonstrated using a final exposure phase (Fig. 3.8 (d)) immediately after the site-selective detection with cooling and repumping light on the D2 line. For this measurement 300 repetitions have been executed and in the addressed trap 77 % of the atoms detected in the second image are still observed in the last image. In contrast 93 % are retained in the 8 surrounding traps.
As a consequence, there is still demand for future characterization measurements in order to identify the sources for additional atom loss. Moreover, as the present approach is based on illumination of the entire array with near resonant light along the transition $|5S_{1/2}, F = 3\rangle \rightarrow |5P_{3/2}, F = 4\rangle$ atoms in state $|5S_{1/2}, F = 3\rangle$ would be affected by scattering in the whole array. Therefore, in a next stage the present technique could be further developed in order to allow for site-selective lossless state detection using excitation along the D_2 line by a steerable beam which has been realized in [123, 124] for a single dipole trap in a static way. Fast state detection at a sub-millisecond timescale two orders of magnitude below the coherence time demonstrated in [67] seems feasible in a straightforward fashion.

3.4. Conclusion

The micro-optical platform equipped with the rearrangement system detailed in this chapter offers scaling capabilities for defect-free prepared initial configurations of individual neutral atoms in an yet unprecedented fashion. Starting from a randomly loaded 19×19 micro-trap array with a filling fraction of about 50 %, clusters comprising up to 111 atoms in predefined locations can be assembled without imperfections.
The option to use multiple rearrangement cycles mitigates the impact of atom loss and is essential for reaching large-scale defect-free clusters. Furthermore, this offers additional flexibility within one experimental cycle. Executing consecutive rearrangement and measurement phases in one run reduces time-consuming MOT loading stages and can significantly increase the data acquisition rate. Moreover, the possibility to remove atoms from a distinct area within the array has been demonstrated. For instance, this allows to control the occupation within an interaction zone which is especially relevant for parallelized Rydberg excitation as discussed in [56]. Even more, as the tweezer system enables exact repositioning from a distinct site to a different location, protocols for entanglement distribution can be implemented in a straightforward way [121].
The movable optical tweezer has also demonstrated to work within Talbot planes of the intrinsically three dimensional dipole trap geometry created by the microlens array. This paves the road to fully filled 3D clusters. Additionally, the tweezer beam path allows for applications apart from atom transport. Offering a beam for individual addressing of sites which is movable on the microsecond timescale, site-selective fluorescence detection of atoms has been demonstrated. Nevertheless, there is also potential for improvement. Within the course of this thesis the limitation regarding the transport efficiency of 75 % has not been finally clarified in detail yet. In reference [29] an efficiency of 99.3 % for atom transfer has been reported for moving atoms in a tweezer array with waists of 1 µm using a movable tweezer with a waist of 1.3 µm. Besides

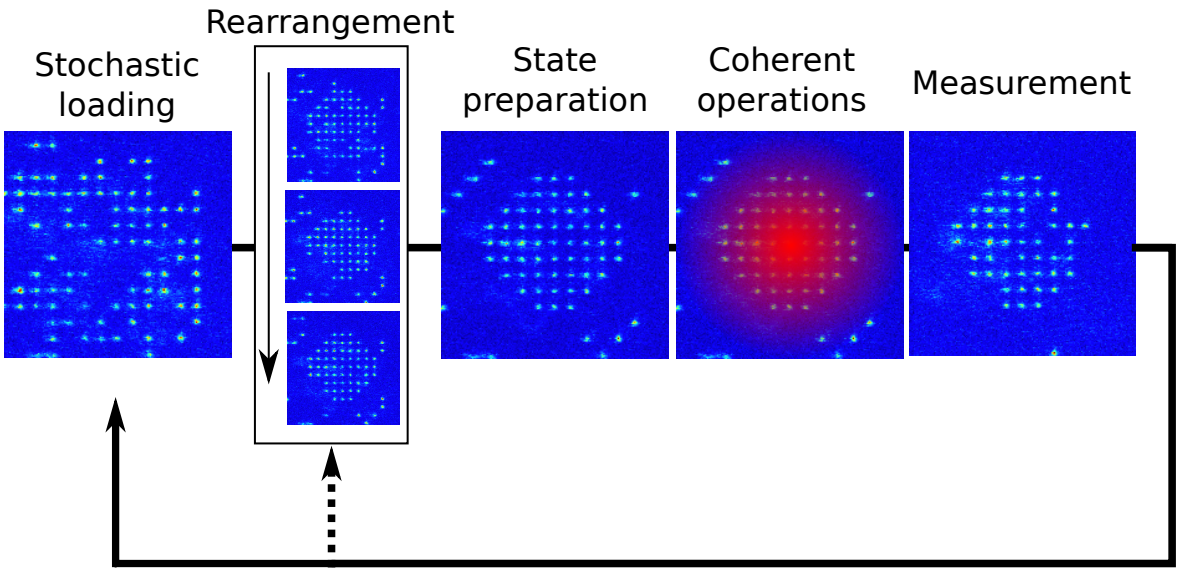

Figure 3.9.: Implementation of the tweezer assembly process into a typical measurement cycle. Subsequent to the stochastic loading from the MOT via collisional blockade a rearrangement sequence is started. After the preparation of a well-defined internal state of the atoms, a phase with coherent operations can be initiated. The result is typically obtained in a loss-based measurement. The emerging defects can either be repaired via rearrangement or a new experimental cycle begins with loading the MOT.

slightly smaller waists, this is in a similar parameter regime as the present platform. Therefore, it remains to be examined whether a reduction of the waists can lead to an improvement in this setup. Based on the perspective of increased transport efficiency and Monte Carlo simulations detailed in [57], defect-free clusters of several hundred atoms are accessible with minor modifications on the experimental platform and up to 1000 atoms are within reach.
As schematically illustrated in Fig. 3.9 the rearrangement process can be included in a typical experimental cycle in a flexible manner and is at hand for the measurements discussed in the following chapters. A typical experimental cycle using the tweezer system includes a rearrangement process directly after the stochastic loading. After the preparation of the atoms into a well-defined internal state, coherent operations on the qubit states can be executed. Typically, this induces atom loss which is detected in the subsequent measurement phase. Given this situation, the residual occupation in the array can serve as a starting point for a new rearrangement cycle or a new loading process from the MOT can be triggered which initiates the next experimental run.

4. Rydberg dynamics with coherent single-site control

4.1. Status quo

As detailed in [56, 57], coherent coupling between the hyperfine ground states and different Rydberg states has been made accessible for the present experimental platform using a two-photon process. This allows for Rabi frequencies of up to $\Omega_{\mathrm{2Ph}} = 2\pi \cdot 0.77(2)\,\mathrm{MHz}$ as demonstrated for coupling between $|5\mathrm{S}_{1/2}, F = 3, m_F = -3\rangle$ and the $|57\mathrm{D}_{5/2}\rangle$ state applying synchronous addressing of 5×5 sites. Moreover, using the $|87\mathrm{D}_{5/2}\rangle$ state, interactions between Rydberg-excited atoms have been realized in a 7 µm-pitch array. These interatomic couplings lead to collective enhancement of the Rabi frequency in the Rydberg blockaded regime.
In order to implement two-qubit gate operations as discussed in Section 2.6.2 in the example of a C_{Z} protocol it is necessary to obtain single-qubit control. Since the coupling between the Rydberg laser fields and the atom is determined by the resonance frequency as well as the laser intensity, both parameters can in principle be used to implement an addressing scheme. The resonance frequency of a ground-to-Rydberg-state excitation can be shifted for selected atoms via application of a local light shift on the ground state. This has been realized in [47, 125] within an 1D alignment of up to 3 traps using an additional focused laser beam. In the present setup this can be implemented utilizing the movable optical tweezer [57]. The light-shift based method has the advantage that it does not require modifications to the optical setup and preserves the ability for synchronous addressing of many atoms. However, this approach relies on an out-of-resonance shift leading to a coupling of all atoms to the Rydberg laser light field except for the addressed one. Therefore, this does not allow for fully independent site-selective control. Additionally, residual coupling is observed for the present setup in this case [57].
As a possible alternative one could take into account shifting a specific atom into resonance using the light shift from the movable tweezer. However, the principle to turn off the dipole traps during the excitation pulse has turned out to be advantageous and is commonly practiced in order to reduce cycle-by-cycle fluctuations of the resonance frequency [47, 125, 126]. Therefore, implementing this approach is also not considered here.
Consequently, an extension featuring site-selective addressing which controls the Rydberg laser light field intensity has been implemented in the experimental apparatus during the course of this thesis. In the following sections this novel system will be presented. First of all, the fundamental concept of Rydberg excitation with respect to the present setup will be explained. This ranges from the two-photon process used for coupling between ground and Rydberg states via the detection mechanism of successful excitation to a presentation of typical measurement techniques used for characterization. As a next step, the Rydberg laser system including frequency stabilization will be discussed which is essential for the following experiments. Thereafter, the setup for site-selective addressing and the integration in the experimental apparatus is detailed and individual-site control within the array is demonstrated. Finally, blockaded interaction between atoms in the tweezer array using the newly integrated system is characterized.

4.2. Driving coherent Rydberg excitations from the ground state

4.2.1. Two-photon ground-Rydberg state coupling

Excitation of rubidium atoms from the ground state to a Rydberg state requires a photon energy in the ultra-violet spectrum corresponding to a wavelength of about $\lambda = 297\,\mathrm{nm}$. Such a direct excitation scheme into a Rydberg state is utilized by various groups [109, 127, 128]. While this way avoids spontaneous emission from an intermediate state when compared to using a multi-photon transition it is in contrast far more difficult to implement in the experimental apparatus. Consequently, it was decided to use a two-photon process as indicated in Fig. 4.1 (a). As illustrated, a laser field at $\lambda_\mathrm{R} = 780\,\mathrm{nm}$ couples the hyperfine ground state $|5\mathrm{S}_{1/2}, F = 3\rangle$ to the intermediate state $|5\mathrm{P}_{3/2}\rangle$ off-resonantly at a detuning Δ_i which enables two-photon excitation into the Rydberg state $|r\rangle$ using additional laser light at $\lambda_\mathrm{B} = 480\,\mathrm{nm}$. This configuration can be treated as an effective two-level system comprising the ground and the Rydberg state as long as $\Delta_\mathrm{i} \gg \Omega_\mathrm{R}, \Omega_\mathrm{B}$ where Ω_R and Ω_B denote the Rabi frequency for the near-infrared and the blue light field, respectively. That condition is fulfilled for all of the experiments presented in this chapter. In this case, the coupling is determined by

$$\Omega_\mathrm{2Ph} = \frac{\Omega_\mathrm{R}\Omega_\mathrm{B}}{2\Delta_\mathrm{i}} \quad \delta = \delta_\mathrm{2Ph} - \left(\frac{\Omega_\mathrm{R}^2}{4\Delta_\mathrm{i}} - \frac{\Omega_\mathrm{B}^2}{4\Delta_\mathrm{i}}\right) \tag{4.1}$$

with the two-photon Rabi frequency Ω_2Ph and the effective detuning δ to the Rydberg state which considers the light shifts resulting from both laser fields. As already discussed in Section 2.1.1 regarding equation 2.15, the photon scattering rate scales as $\Gamma_\mathrm{SC} \propto 1/\Delta_\mathrm{i}^2$ demanding for maximum possible detuning in order to reduce spontaneous processes involving $|5\mathrm{P}_{3/2}\rangle$. However, due to the significantly lower coupling strength between the intermediate and the Rydberg state compared to the ground and the intermediate state, the available power of blue laser light poses the major limitation.

4.2.2. Detection of Rydberg-excited atoms

In addition to the possibility to excite atoms into Rydberg states it is essential that this excitation can be detected. The fact that trapping of Rydberg atoms requires additional effort [129, 130] allows to implement the detection of Rydberg excitation in a loss-based fashion. Ground state atoms are continuously influenced by the dipole potential and are therefore trapped in the tweezers. Even in case of an excitation via the D_1 or D_2 line there is only an insignificant time on the order of tens of nanoseconds (Table A.1) without attractive coupling to the laser field of the dipole traps due to the short lifetime of the excited states.
In contrast, as a result of the n^3-scaling of the lifetime, already for a $57\mathrm{D}_{5/2}$ state one obtains about $\tau_{57} = 93\,\mu\mathrm{s}$ while for $82\mathrm{S}_{1/2}$ the lifetime calculates to $\tau_{87} = 217\,\mu\mathrm{s}$ as discussed in Section 2.6. During this period, the atoms do not experience the attractive force from the tweezer potential and escape from the traps because of their residual velocity. There is even an additional repulsive effect owing to the ponderomotive potential V_p experienced by the weakly bound Rydberg electron [131] which can be written in terms of the dipole trap intensity I, the electron mass m_e and the laser frequency ω_L of the dipole trapping light as

$$V_\mathrm{p} = \frac{e^2 I}{4 m_\mathrm{e} \omega_\mathrm{L}^2}. \tag{4.2}$$

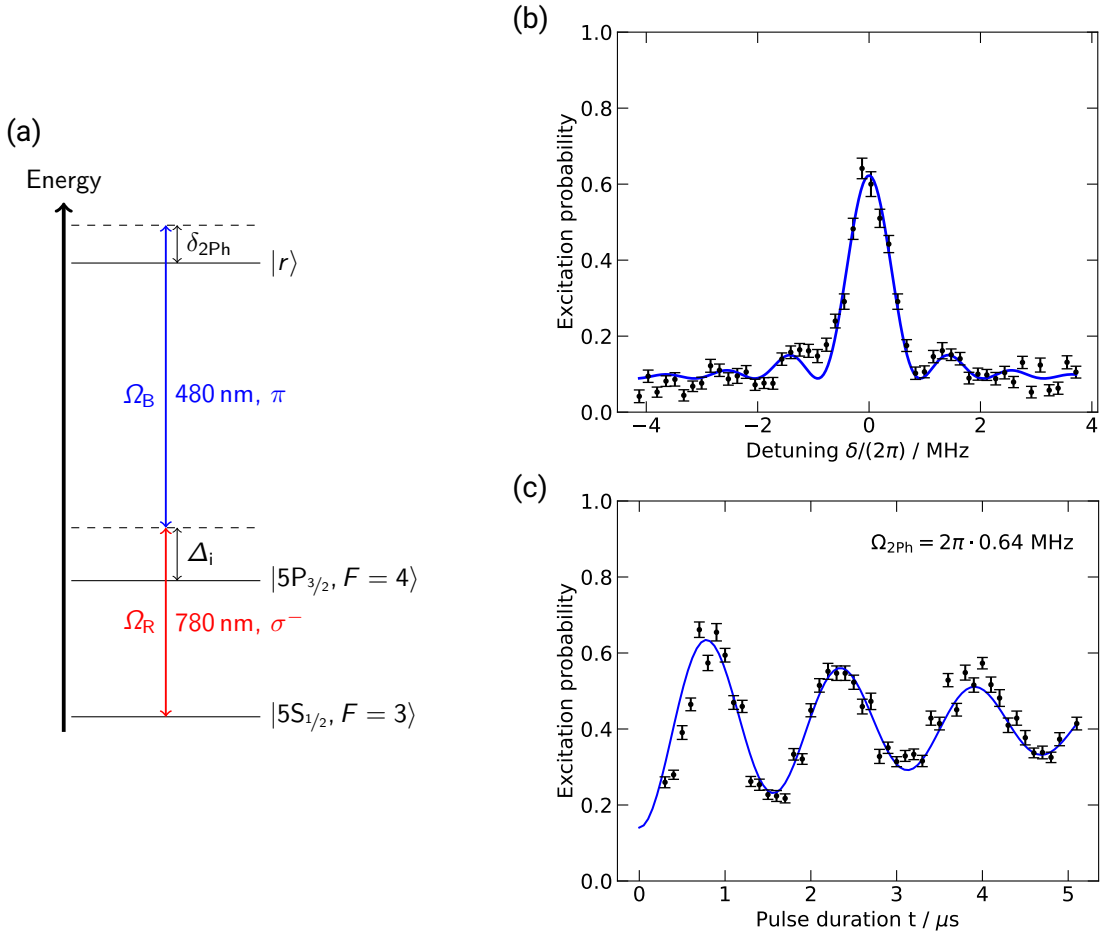

Figure 4.1.: Rydberg spectroscopy and ground-Rydberg state coupling strength measurement. (a) Using a two-photon process detuned by Δ_i from the intermediate state and with variable detuning δ_{2Ph} to the excited state allows for excitation into the Rydberg state and spectroscopy. (b) Resonance of $|57D_{5/2}\rangle$. The peak is found for an effective detuning $\delta = 0$ including light shifts and shows the excitation probability into the Rydberg state for a pulse duration of $\tau = 1$ µs. (c) At resonance ($\delta = 0$) the coupling strength to the Rydberg state can be determined via measuring the Rabi frequency.

This leads to the loss of atoms from the trap after being excited into the Rydberg state which can be verified through fluorescence detection after the Rydberg excitation sequence. Consequently, after multiple repetitions the observed probability P_r to excite an atom can be calculated from the detected number of lost N_- and retained N_+ atoms via $P_r = \frac{N_-}{N_+ + N_-}$. This does not account for detection errors which will be discussed in Section 4.2.4 in the example of typical characterization measurements.

4.2.3. Typical experimental cycle for Rydberg experiments

Rydberg measurements discussed in this thesis always start after the rearrangement phase which typically consists of multiple rearrangement cycles as detailed in Chapter 3. After the

last cycle, the occupation of the traps is determined via fluorescence detection in order to retrieve the initial situation before the Rydberg measurement phase. Next, the magnetic field which defines the quantization axis is turned on and the depth of the dipole traps is reduced by about a factor of 5. In order to obtain a well-defined internal state of the atoms, preparation via optical pumping according to Section 2.5 is executed which takes up to 800 µs. During all Rydberg experiments presented in this thesis the effective pulse length of the two-photon coupling τ shall be determined by the width of the 780 nm Rydberg laser pulse which is defined using an AOM that allows for switching of the laser light below 100 ns. This keeps spontaneous processes involving the intermediate level at a minimum. Therefore, the blue light field is always turned on prior to the 780 nm laser beam and deactivated after the latter has been switched off. During the short time of the 780 nm laser pulse of only a few microseconds, the dipole traps are fully turned off which avoids spatial dependence of the two-photon resonance frequency due to inhomogeneous light shift on $|5S_{1/2}, F = 3\rangle$ over the array. Furthermore, this avoids cycle-by-cycle variations in the resonance frequency resulting from atoms being at different positions in the trapping potential. Finally, the dipole traps are ramped up again for detection of the remaining atoms in the array via fluorescence imaging.

4.2.4. Measuring coupling strength for coherent Rydberg excitation

Figure 4.1 (b, c) shows single-atom Rydberg excitation signals obtained for typical characterization measurements of the ground-Rydberg state coupling. In this case, the two-photon transition $|5S_{1/2}, F = 3, m_F = -3\rangle \rightarrow |57D_{5/2}, m_J = -3/2\rangle$ is depicted and a detuning to the intermediate state $|5P_{3/2}, F = 4\rangle$ of $\Delta_i = 2\pi \cdot 410$ MHz is chosen. Maintaining a constant duration $\tau = 1$ µs of the excitation pulse and varying the detuning δ to the Rydberg state, one obtains the spectroscopic signal of the resonance as shown in Figure 4.1 (b). Approximating the excitation probability P_r with the Fourier transformation of a square pulse

$$P_r(\delta) = A \cdot \frac{\Omega_{2Ph}^2}{\Omega_{2Ph}^2 + \delta^2} \sin^2\left(\frac{\tilde{\tau}}{2}\sqrt{\Omega_{2Ph}^2 + \delta^2}\right) + B \tag{4.3}$$

and leaving $\tilde{\tau}$ as a free parameter yields the solid curve with $\tilde{\tau} = 0.94(7)$ µs which matches the configured pulse length of $\tau = 1$ µs. From these type of spectroscopic measurements, the exact position of the two-photon resonance can be determined as a basis for subsequent experiments. In order to retrieve a value for the coupling strength, the result of a spectroscopy can then be used for recording Rabi oscillations on resonance as shown in Figure 4.1 (c). In this case, the laser frequency is kept constant ($\delta = 0$) and the pulse duration is varied. The time-dependent two-photon coupling between ground and Rydberg state can then be written as

$$P_r(t) = \frac{\Omega_{2Ph}^2}{2\Omega_{2Ph}^2 + \gamma^2}\left[1 - \left(\cos\left(\tilde{\Omega}t\right) + \frac{3\gamma}{4\tilde{\Omega}}\sin\left(\tilde{\Omega}t\right)\right)e^{-3\gamma t/4}\right] \tag{4.4}$$

with an exponential damping factor and an effective frequency $\tilde{\Omega} = \sqrt{\Omega_{2Ph}^2 + \gamma^2/16}$ as derived in [132]. The solid curve shows the approximation of the measured data with equation 4.4. From this fit, the two-photon Rabi frequency can be determined to $\Omega_{2Ph} = 2\pi \cdot 0.64(5)$ MHz. Apparently, the curves neither reach $P_r = 0$ excitation probability away from the resonance nor $P_r = 1$ in case of resonant coupling. This is due to several reasons and has been thoroughly analyzed in [57]. First, a finite recapture probability of typically 95 % leads to a permanent baseline in the excitation probability. Second, imperfect initial state preparation efficiency

of 96 % results in an upper bound. Third and mostly, according to a Monte Carlo simulation based on a release and recapture measurement the probability to trap a Rydberg-excited atom again after decay into the ground state is about 19 % for $57D_{5/2}$ and therefore a significant contribution. This could be overcome by increasing the wavelength of the trapping light leading to a stronger ponderomotive potential but is beyond the scope of this thesis.

4.3. Fast tunable laser light for Rydberg excitation

In order to execute spectroscopic measurements or coherent quantum operations with Rydberg atoms stable yet quickly adjustable laser fields are necessary. This requires, on the one hand, a reliable intensity stabilization which is implemented using the control unit reported in [70]. On the other hand, stable laser frequencies are indispensable to achieve high-fidelity quantum control [126]. This section discusses the implementation of those prerequisites in the experiment.

4.3.1. Laser frequency stabilization

Both Rydberg lasers are stabilized in frequency using a high finesse cavity (VH-6020-4, Stable Laser Systems). The cavity is kept under a vacuum with a residual pressure of 4×10^{-5} mbar and temperature stabilization near the experimentally determined zero crossing point of 302.61(7) K [57]. This renders the relaxation of the spacer material to be the dominant contribution to the resonance drift which is specified by the manufacturer as 50 kHz per day. The free spectral range *FSR* was measured to $FSR = 1496.923(2)$ MHz and the finesse for light at $\lambda = 780$ nm and $\lambda = 960$ nm has been determined via cavity ring-down time measurements to $\mathcal{F}_{780} = 31\,500(100)$ and $\mathcal{F}_{960} = 46\,700(120)$, respectively. From an analysis of the cavity transmission signal, a linewidth below 11 kHz for the 780 nm laser and smaller than 9 kHz for the frequency doubled light at 480 nm can be estimated [57].

Near-infrared Rydberg laser setup

The near-infrared Rydberg laser is an interference filter based ECDL providing the light for coupling to the intermediate level during Rydberg excitation at $\lambda_R = 780$ nm. The frequency stabilization to the high finesse cavity relies on the Pound-Drever-Hall (PDH) technique [133, 134] which enables locking to the narrow cavity resonances. This requires the modulation of sidebands on the probe light fed into the cavity which is realized using an AOM in double-pass configuration driven at a carrier frequency of 110 MHz and a modulation frequency of 10 MHz based on a multi-channel DDS (AD9959, Analog Devices). The slow feedback loop to the piezo actuator which steers the resonator length and the fast feedback circuit that acts on the diode current via a field-effect transistor (FET) are closed by a control unit (VP-D2-125, Vescent).

Blue Rydberg laser system

The laser light at $\lambda_B = 480$ nm is produced by a commercial laser system (TA-FHG 110, Toptica) consisting of a tapered amplifier (TA) which is seeded by a grating-stabilized ECDL running at $\lambda = 960$ nm and fed into a frequency doubling stage. After the second harmonic generation (SHG) light at $\lambda = 480$ nm is coupled into a single-mode optical fiber which delivers it to the

experimental apparatus. Frequency stabilization to the high finesse cavity is realized using the PDH method with a feedback loop involving a fast laser locking module (FALC 110, Toptica). For this purpose, the laser current is modulated at 24 MHz in order to produce the sidebands. The laser frequency is stabilized via control of the external cavity length by a piezo element and a FET for fast feedback to the diode. In addition, a second PDH control loop optimizes the SHG efficiency.

Implementations for dynamic frequency variation

Dynamic laser frequency control of the Rydberg lasers is not only important for spectroscopical identification of a transition but also allows for application of excitation schemes in the future which are based on rapid adiabatic passage [135, 136] enabling high-fidelity qubit gates. During this thesis means for dynamic frequency control of the Rydberg laser system have been implemented. This includes frequency change on a cycle-by-cycle basis as well as in real-time if necessary. With regard to the blue Rydberg laser system, the 960 nm light used for stabilization is directed through an AOM in double-pass configuration before being coupled into the cavity. As a consequence, changes in the frequency set point of the blue laser light always involve the feedback loop for stabilization to the reference cavity, too. Even though this limits the bandwidth for frequency adaption that implementation is chosen in order avoid additional losses of blue laser light power. Therefore, this method of frequency control is used on a cycle-by-cycle basis only.
In contrast, the beam path of the 780 nm Rydberg laser includes an AOM in double-pass configuration before the fiber coupling to the experimental apparatus which enables fast frequency adaption in a span of several tens of megahertz. This is especially vital in the scope of fast single-site addressing with a steerable beam controlled via acousto-optic deflection that is presented in the following section.

4.4. Site-selective coherent Rydberg dynamics in predefined configurations

4.4.1. Experimental setup

Optical setup

Figure 4.2 depicts the optical setup for Rydberg excitation on a site-selective basis. The measurements in this chapter are based on the microlens array MLA2 (Table 2.1) for the creation of a 7 µm-pitch tweezer array. After exiting a single single-mode optical fiber, the 780 nm Rydberg laser beam is σ^--polarized and enters the chamber along the x-direction. For the beam radius a value of $w_\mathrm{R} = 550(50)$ µm has been measured. The linearly polarized blue Rydberg laser beam is also delivered by a single-mode fiber and passes a 2D acousto-optic deflection system composed of two AOD (CT4105, Crystal Technology) that are mounted with their deflection plane oriented orthogonally against each other. An achromatic doubled L6 with a focal length of $f_\mathrm{L6} = 40$ mm is positioned so that the AOD pivot center of rotation lies in the focal plane of L6. The beam passes another achromatic doublet L7 with a focal length of $f_\mathrm{L7} = 500$ mm before being focused onto the array plane within the vacuum chamber. As the microscope objective LS2 is used for monitoring the intensity distribution of the dipole trap array and the movable tweezer as well as for focusing the blue laser beam the latter is kept

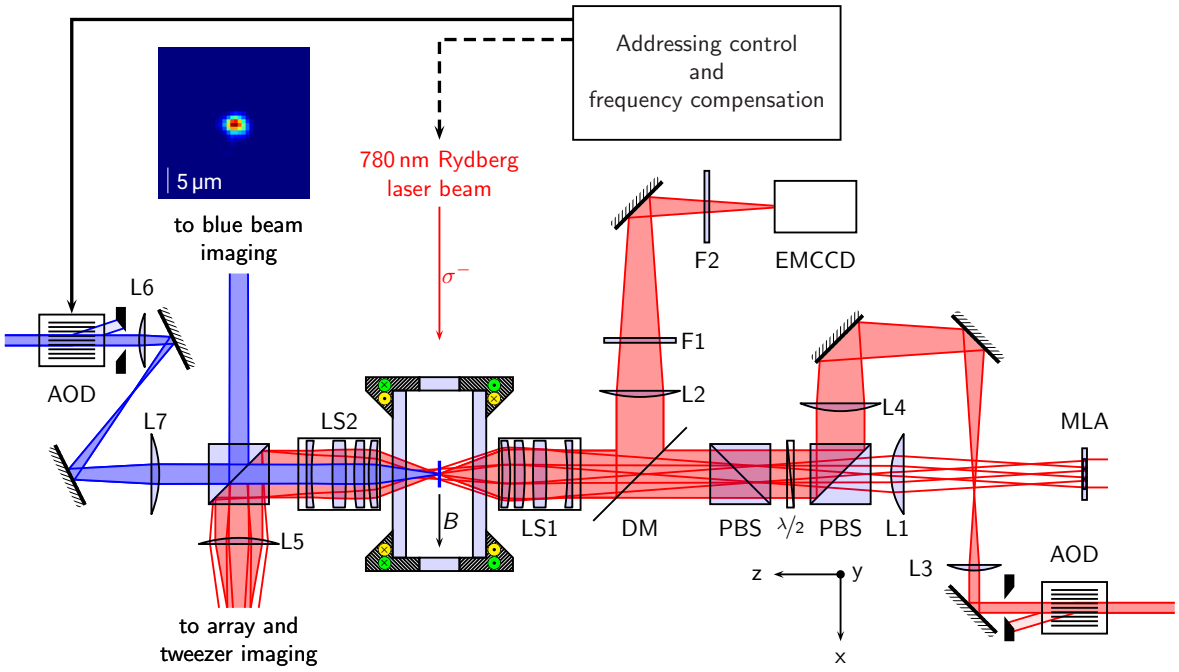

Figure 4.2.: Simplified schematic of the setup for Rydberg excitations with single-site addressing. Using the 2D beam steering system composed of two AODs with orthogonally oriented deflection planes allows for individual addressing of atoms in the tweezer array with the blue Rydberg laser. For this purpose, two achromatic doublets L6 and L7 are used in combination with the microscope objective LS2 to turn the collimated laser beam deflected by the AODs into a movable spot in the atom plane. The beam positioning is executed by the addressing control system which supplies the RF for the AODs and also takes care of the frequency compensation to maintain the two-photon resonance via shifting the 780 nm Rydberg laser frequency accordingly. The deflected light off the polarizing beam sampler is utilized for continuous monitoring of the blue spot with a CCD camera. Entering the chamber along the x-direction the σ^--polarized 780 nm Rydberg laser illuminates the full array due to its large radius.

slightly diverging after L7 in order to compensate for the chromatic axial shift of the focal spot which calculates to about 900 µm. The light which is deflected at the polarizing beam sampler before LS2 is used for spatial monitoring of the blue beam. In the inset an image of the beam focus taken with the CCD camera is shown from which the beam waist could be determined to $w_{0,\mathrm{B}} = 2.1(2)$ µm. The spot position is moved through the RF connected to the AODs and generated by the addressing control system which can also alter the frequency of the 780 nm Rydberg laser beam via the AOM in double-pass configuration in the beam path before the fiber coupling to the experiment. Based on a diffraction efficiency of more than 50 % measured for the 2D deflector over a frequency span of 40 MHz this allows for addressing of an area larger than 100 µm × 100 µm corresponding to 14 × 14 sites with the blue Rydberg laser beam.

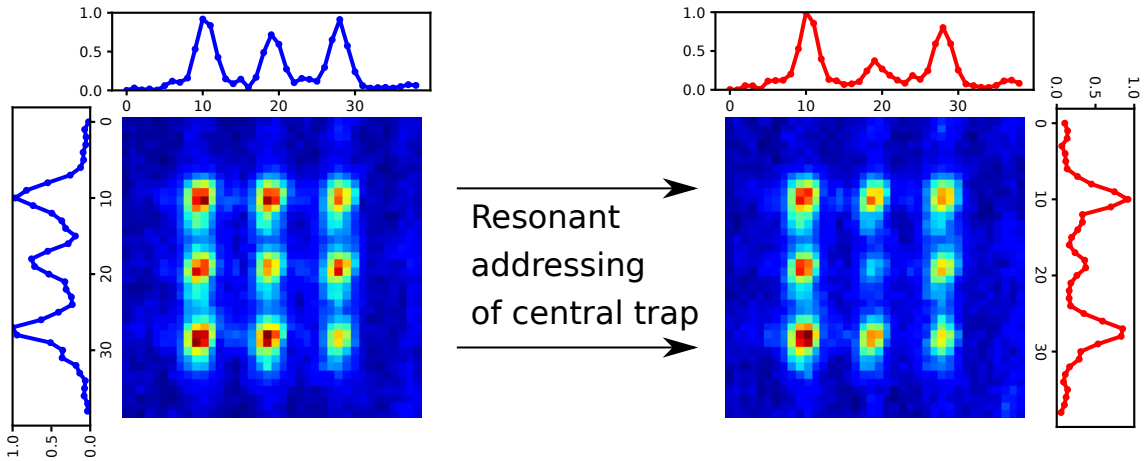

Figure 4.3.: Determining the blue beam alignment using resonant excitation to a Rydberg state. The signal distribution in the averaged fluorescence images can be associated with the mean occupation in the assembled 3×3 cluster before (left) and after (right) the excitation phase of the blue beam in combination with the MOT lasers. The horizontal and vertical cross sections through the image centers show the normalized fluorescence signal, respectively. As a result from focusing the blue beam onto the central trap in the cluster, this exhibits a significant reduction in the signal when comparing the second with the first image which allows for a clear localization of the spot within the array. The slightly lower signal in the central trap before the addressing can be associated with imperfect preparation of this site during the measurement.

Integration of the module in the experimental control system.

In order to guarantee fast frequency switching, the RF source for the AODs was chosen to be two DDS evaluation boards (AD9910, Analog Devices) which grant direct access to the frequency via parallel ports. This DDS allows for defining the output frequency via a 16-bit frequency tuning word (FTW) attached to its parallel input port at a rate of 250 MHz using a system clock running at 1 GHz. From these settings a frequency resolution of 954 Hz can be achieved. The FTWs are provided by an FPGA module (DE1-SoC, Terasic) identical to the one used for the movable tweezer but with an adapted circuit synthesized in the FPGA fabric. Using a system clock of 50 MHz the circuit takes 40 ns for a single channel frequency change. For the purpose of achieving this rate, a FIFO (first-in, first-out) buffer has been implemented in the system which can store up to 1000 predefined frequencies. This allows for a change of the DDS frequency in-sync with the main experimental control system well below the limit given by the switching time of the AOD which is about 1 µs. While the addressing of neighboring array sites necessitates frequency changes of 2.7(1) MHz for both dimensions this demands for a compensation mechanism in order to maintain the two-photon resonance when addressing different sites. This is realized using a third DDS ("frequency compensation") of the same type which is controlled synchronously by the FPGA system and supplies the radio frequency for the double-pass AOM in the 780 nm Rydberg laser beam.

4.4.2. Beam alignment

Due to the small radius of the blue Rydberg laser beam, the initial alignment has been executed via loss detection on resonance. For this purpose, the blue Rydberg laser is stabilized to the transition $|5P_{3/2}, F = 4\rangle \rightarrow |84D_{5/2}\rangle$ which allows in combination with the MOT lasers to resonantly excite atoms into the Rydberg state. Figure 4.3 shows the result of a measurement consisting of 50 experimental runs to determine the alignment. After an assembly sequence for a 3×3 cluster utilizing the optical tweezer a fluorescence image is taken. This is followed directly by a phase of 5 ms in which the MOT lasers are activated together with the blue Rydberg laser beam. A second image is then used to determine the occupation within the cluster afterwards. Figure 4.3 (left) shows the averaged fluorescence images before and Figure 4.3 (right) after the excitation phase. The horizontal and vertical cross sections depict the normalized fluorescence signal through the image center, respectively. Using about 200 µW blue laser power is sufficient to see a clearly localized effect and verify good overlap with the central trap in the cluster.

4.4.3. Demonstration of site-selective ground-to-Rydberg state excitation

As shown in Fig. 4.4, for the following measurement the $|82S_{1/2}\rangle$ Rydberg state has been selected to demonstrate site-selective addressability. This is a suitable candidate on the way to an implementation of entangled atom clusters within the present platform as illustrated in Figure 3.6 (c) since the van der Waals interaction is isotropical for $|nS\rangle$ states to very good approximation. Furthermore, the $|5S_{1/2}, F = 3, m_F = 0\rangle$ is chosen as initial state due to its magnetic field insensitivity which has shown coherence times on the order of 100 ms [55, 67, 122]. The efficiency of initial state preparation via optical pumping has been measured to 80(5) % using ground state stimulated Raman transitions as discussed in Chapter 5. For the two-photon transition the detuning to the intermediate state is set to $\Delta_i = 550$ MHz. The 780 nm Rydberg laser power in the atom plane amounts to $P_R = 1$ mW while the power of the blue laser is $P_B = 10$ mW. This yields theoretical Rabi frequencies of $\Omega_R = 2\pi \cdot 28.8$ MHz and $\Omega_B = 2\pi \cdot 29.4$ MHz, respectively, resulting in a two-photon Rabi frequency $\Omega_{2Ph} = 2\pi \cdot 0.74$ MHz. Figure 4.5 demonstrates the capability of the addressing system to create site-selective coherent ground-Rydberg state coupling in predefined atom-by-atom assembled configurations. As depicted in the inset (left), a target geometry for rearrangement consisting of 10 atoms is selected for this measurement while in each experimental realization one of the five colored traps (right) is addressed randomly using a variable pulse length. Addressing a specific trap within a cycle is reflected by the same color of the respective data points of all the curves visible for the various sites. Each of the addressed traps exhibit clear Rabi oscillations between the Rydberg and the ground state solely in case the blue beam is steered on their position during the 780 nm Rydberg laser pulse while in all other sites no coherent

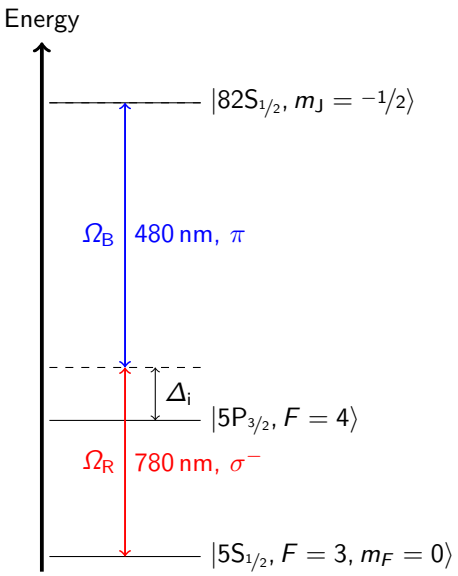

Figure 4.4.: Excitation scheme for site-selective ground-Rydberg state coupling. Using a two-photon process detuned by $\Delta_i = 2\pi \cdot 550$ MHz.

coupling is observed for the respective group of cycles. It becomes evident that only in the traps which are addressed atom loss exceeding the baseline loss discussed in Section 4.2.2 is detected. The solid curves are the results from a fit of equation 4.4 to the measured data. This yield two-photon Rabi frequencies ranging from $2\pi \cdot 0.57(5)$ MHz (green) to $2\pi \cdot 0.78(5)$ MHz (purple) corresponding to sub-microsecond π-pulse times.

4.4.4. Site-selective Rydberg blockade

A crucial next step for the implementation of a two-qubit gate is the evidence of Rydberg blockaded interactions in the novel site-selectively addressable setup. This can be demonstrated in the configuration shown in Fig. 4.6 (a) where two atoms are positioned near each other and are sequentially addressed by the blue Rydberg laser beam. One of them is defined as the control atom (left) the other as the target atom (right) in analogy to Fig. 2.9 in Section 2.6.2. During the addressing sequence each excitation pulse width is always defined by the 780 nm Rydberg laser beam which illuminates both atoms simultaneously and can be switched quickly. As shown in Fig. 4.6 (b), this is implemented in the experiment using atom rearrangement into two central sites of the array through the movable optical tweezer. After the assembly phase and a state preparation into $|5S_{1/2}, F = 3, m_F = 0\rangle$ the experimental runs alternate in a pseudo-random fashion between two realizations. Either the control atom is addressed with a π-pulse of 1.4 µs followed by addressing the target atom for a variable time t or the former step is omitted. For this addressing sequence a 780 nm laser power of $P_{\mathrm{R}} = 0.5$ mW and a blue laser power of $P_{\mathrm{B}} = 8$ mW is employed for which the Rabi frequencies calculate to $\Omega_{\mathrm{R}} = 2\pi \cdot 20.4$ MHz and $\Omega_{\mathrm{B}} = 2\pi \cdot 26.7$ MHz, respectively, yielding a theoretical two-photon Rabi frequency of $\Omega_{\mathrm{2Ph}} = 2\pi \cdot 0.47$ MHz. The measured π-pulse duration of $\tau_{\pi,\mathrm{exp}} = 1.33(4)$ µs is therefore below the calculated value of $\tau_\pi = 1.06$ µs which can be related to a radial displacement of the blue beam focus relative to the addressed site of 1 µm. Figure 4.6 (c) depicts the probability to lose the target atom when the control atom has been successfully excited after the pulse ($|c\rangle = |r\rangle$) or is preserved in the array ($|c\rangle = |g\rangle$) having left out the control pulse. Apparently, Rydberg excitation of the control atom prevents the target atom from getting excited which demonstrates Rydberg blockade.

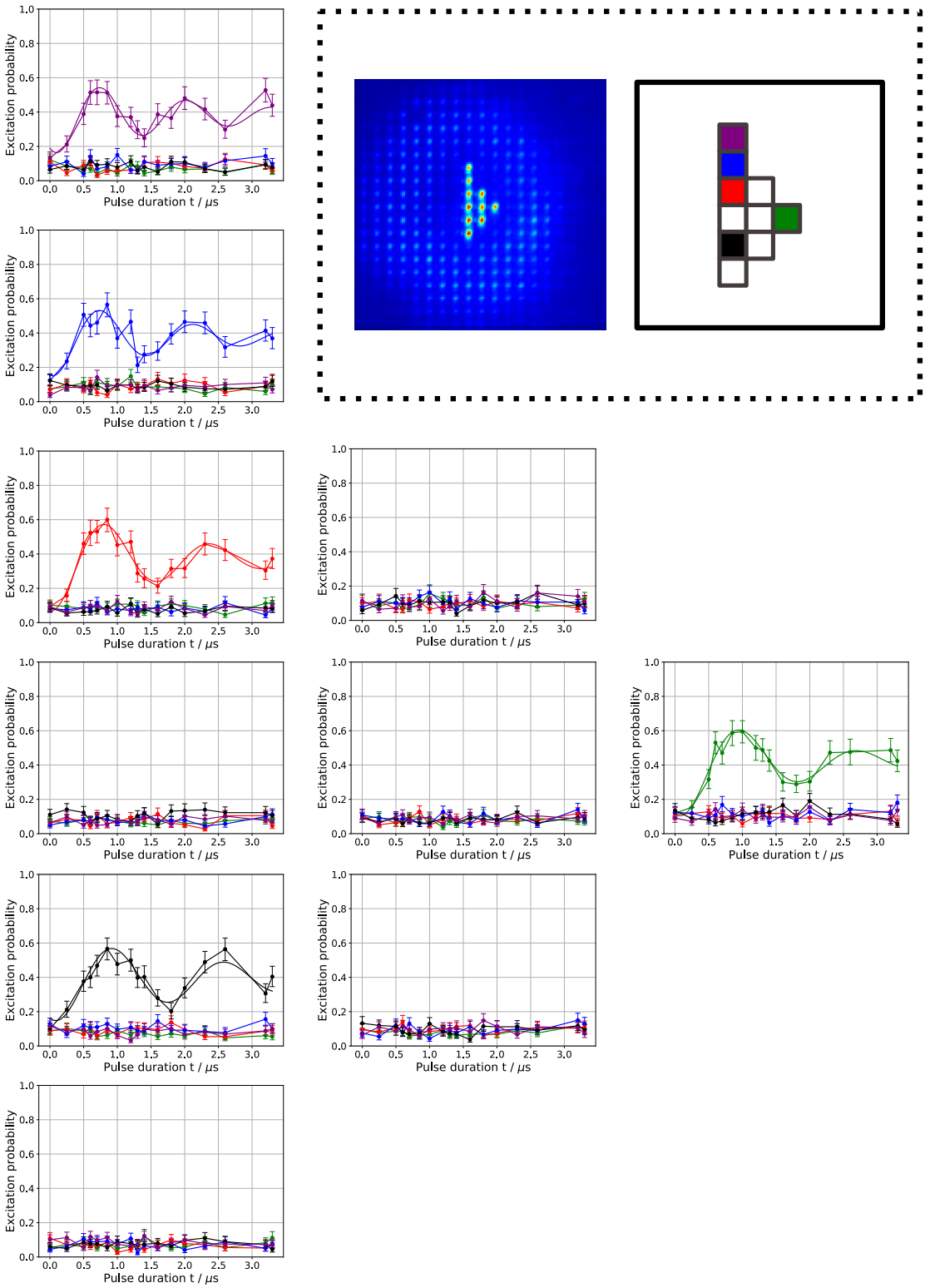

Figure 4.5.: Site-selective Rydberg excitations. Using the 2D beam steering system enables individual addressing of arbitrary sites in assembled geometries. The arrangement of the data panels reflects the target configuration of the arranged atoms. See main text for details.

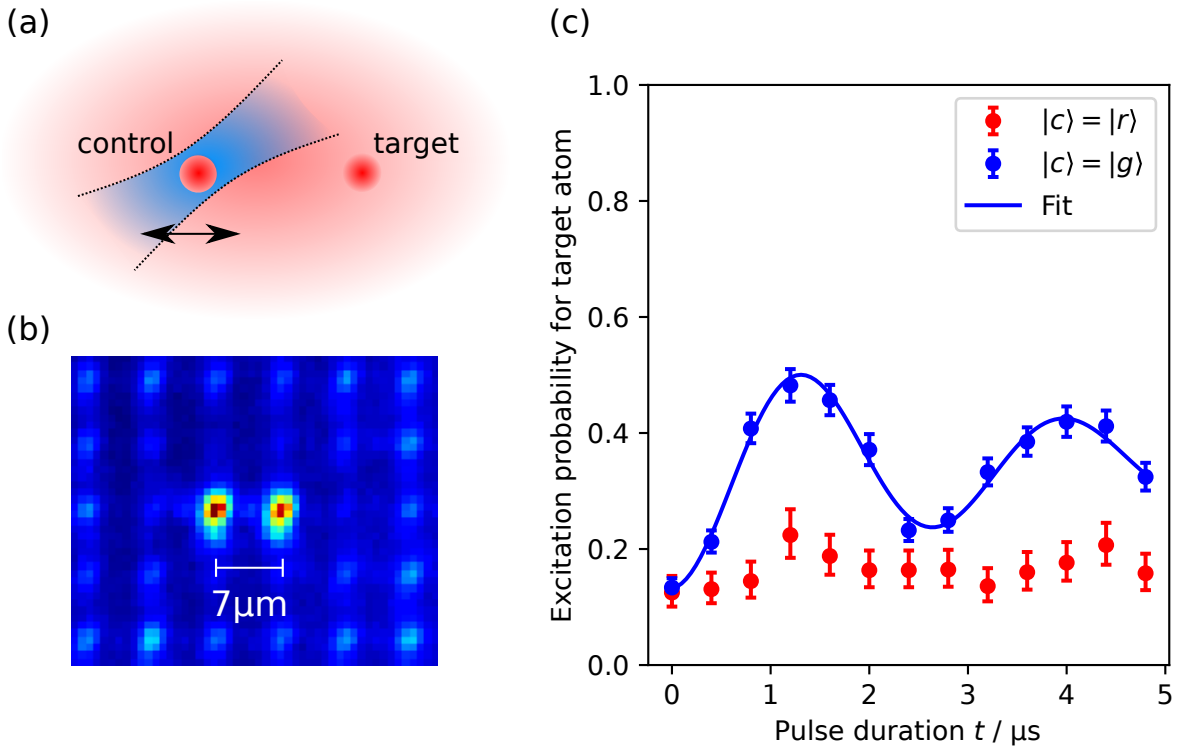

Figure 4.6.: Blockaded Rydberg interaction of atom pair. (a) Schematic illustration of the addressing. While the 780 nm Rydberg laser field illuminates the whole array moving the blue Rydberg laser focus allows for site-selective control. Interaction can be demonstrated when analyzing the excitation probability into the Rydberg state of a target atom depending on whether a nearby control atom has been excited before or not. (b) This alignment is implemented in the array for two neighboring sites in the 7 µm-pitch array as shown in the averaged fluorescence image after rearrangement using the movable optical tweezer. (c) Excitation probability for the target atom without excitation pulse on the control atom ($|c\rangle = |g\rangle$) and after successful excitation of control atom ($|c\rangle = |r\rangle$).

4.5. Conclusion

In this chapter, a novel setup for coherent ground-Rydberg state coupling with single-site addressability in the optical tweezer platform has been presented which was realized in the course of this thesis. Based on a two-dimensional beam steering system, individual atom addressability via a two-photon transition is available yielding Rabi frequencies of up to $\Omega_{2\mathrm{Ph}} = 2\pi \cdot 0.78(5)\,\mathrm{MHz}$ limited by the available laser power. The reduced beam radius which goes along with the site-selective control enables to achieve the same coupling strength for the $|87\mathrm{D}_{5/2}\rangle$ state as for the $|57\mathrm{D}_{5/2}\rangle$ state [56, 57] in the experimental platform despite the increased detuning to the intermediate state of the two-photon process. Using an upgraded, readily commercially available blue laser system will now easily allow for pushing the coupling strength into the megahertz regime for high-lying Rydberg states just via increasing the laser power. This is beneficial in order to decrease sensitivity to spontaneous emission processes from the intermediate state, reduce atom loss resulting from the fact that Rydberg atoms are

not trapped anymore, and minimize dephasing due to the finite velocity of the atoms during the interaction period [47]. Additionally, as practiced in [126] counterpropagating alignment of the Rydberg laser beams can be applied as a next step to reduce the Doppler effect which significantly contributes to dephasing as simulated in [57] for the present experimental setup. Even further improvement can then be expected using filtering techniques for the Rydberg laser light as employed in [126] in order to reduce phase noise.
Moreover, the initial ground state preparation efficiency into $|5S_{1/2}, F = 3, m_F = 0\rangle$ needs to be addressed in future work. While the value of $80(5)$ % is in agreement with the reported efficiency in [67] it, nevertheless, significantly reduces the Rydberg excitation probability and will substantially impair the fidelity of gate operations. However, this can be tackled using an optimized initial state preparation scheme via optical pumping involving the D_1 line. For instance, 99 % efficiency has been reported for ^{87}Rb in [137].
Using the site-selective control system, Rydberg-blockaded atom interaction has been successfully demonstrated after sequentially addressing a pair of atoms. This can now serve as a starting point for future work towards implementation of gate operations in the manner detailed in [41], analysis of entanglement distribution using the optical tweezer [121] and implementation of spin-dynamics for simulation of quantum magnetism [49, 90, 91]. Based on the approach for tweezer array generation detailed in [28, 90] a multi-tone configuration will allow for parallelized addressing of many sites in the future and pave the way for the implementation of multiqubit gates in the present experimental platform [42].

5. Magnetic-field sensing within an individual-atom quantum array

5.1. Quantum sensing

Using quantum technology for the purpose of measuring physical quantities has evolved into an highly topical field of research. The principal objective is to exploit quantum properties as entanglement or superposition in order to develop sensors with higher accuracy and/or smaller form factor than conventional instruments. Prominent examples are atomic clocks which have reached one record-breaking result in precision after the other within recent years [138–140]. Besides defining the time standard, they have versatile additional applications. Among them are tests for variations of fundamental constants, further examination of Einstein's theory of relativity as well as geodetic methods [141]. Other technologies based on superconducting devices (SQUIDs) can be used in the context of magnetometry and reach sensitivities that allow for detection of weak magnetic fields. They already find their application in the analysis of the brain's electrical activity which produces fields on the order of femtotesla [142]. Nitrogen-vacancy defects in diamond [143] as well as optically pumped magnetometers [144] also constitute highly sensitive systems with comparable performance each one with specific advantages and requirements.
The universal quantum platform presented in this work is also capable of sensing magnetic fields based on individual atoms in the two-dimensional tweezer plane as sensor elements. This enables flexible configuration of the spatial resolution or sensing position via moving the tweezers [55] as well as changing the microlens array or reimaging optics. Using atomic systems for sensing has the advantage of working with stable quantum entities with identical properties for each individual in contrast to manufactured devices. Consequently, the measurements depend mainly on fundamental constants and can rely on their precise knowledge. With respect to rubidium, for instance, there exists a profound data situation [83].
The technique for sensing is based on the intrinsic sensitivity of the rubidium hyperfine levels on external magnetic fields (Fig. A.1). These levels will be spectroscopically analyzed and shifts in their separation will be traced back to the magnetic field strength experienced by atoms at a specific site in the array.

5.2. Experimental setup

Figure 5.1 illustrates the details of the experimental apparatus which are of special relevance for the measurements discussed in the following sections. Based on the microlens array MLA2 they have all been conducted in a quadratic-grid tweezer configuration with a pitch of $p = 7.0(2)$ µm within a 19×19 workspace comprising 361 sites as detailed for the Rydberg measurements in the previous chapter. In order to use the 2D atom array as a magnetic field sensor plane, a static homogeneous magnetic field $B_{\mathrm{x,q}} = 283(1)$ µT is applied along the x-axis during each measurement phase. It is induced by the pair of coils marked green in Fig. 5.1 (a). This field lifts

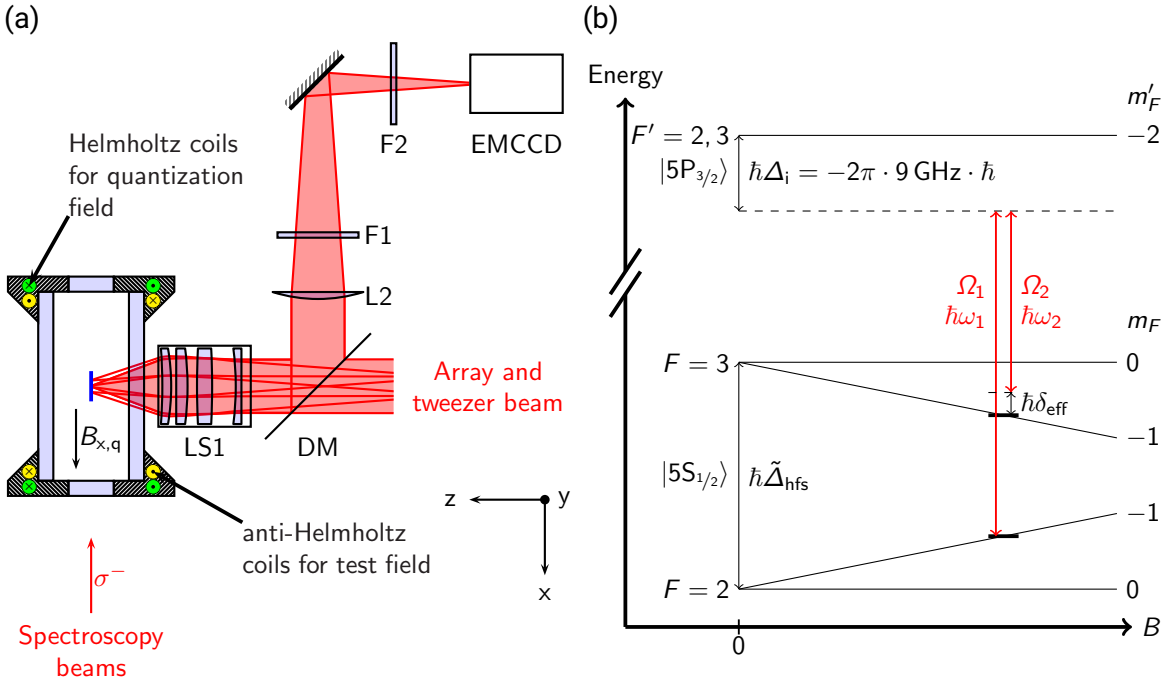

Figure 5.1.: (a) Simplified experimental setup. A 361-site individual-atom array is generated by a microlens array whose focal plane is reimaged into the vacuum chamber. This beam is superimposed with the single movable optical tweezer. The trapped atoms can be addressed via circular polarized spectroscopy beams from the negative x-direction which allows to drive two-photon transitions between the hyperfine ground states of the atoms. (b) Level scheme of the D2-line of ^{85}Rb restricted to the two-photon transitions used for characterization measurements and magnetic field sensing (not to scale). The state energy of $m_\mathrm{F} \neq 0$ states depends strongly on the magnetic field experienced by the atom while states with $m_\mathrm{F} = 0$ exhibit several orders magnitude less sensitivity. For clarity, only the two-photon transition for the case of $m_\mathrm{F} = -1$ states is indicated.

the degeneracy of the magnetic hyperfine levels and creates a well-defined quantization axis. In addition, the gradient field generated by the pair of coils in anti-Helmholtz configuration (colored yellow in Fig. 5.1 (a)) also used for the MOT serves as a test field for sensing. This is realized using the two-photon Raman process that will be detailed in Section 5.3.1 to determine the resonance frequency of states that are sensitive to external magnetic fields and trace this back to a magnetic field strength. The respective spectroscopy beam consisting of the two circular polarized Raman laser beams is delivered by a single-mode fiber and aligned along the quantization axis in the negative x-direction resulting in a Doppler-free configuration. Figure 5.1 (b) shows the hyperfine ground states which are used for the initial characterization measurements as well as for the purpose of magnetic field sensing. As indicated schematically, the dependence of the states with $m_\mathrm{F} = 0$ on the magnetic field strength B is very weak and amounts to a shift of $\pm 2\pi \cdot 5.18(4)$ kHz for $B = B_{\mathrm{x,q}}$ using the Breit-Rabi formula (equation 2.33) where the plus sign corresponds to $F = 3$ and the minus sign to $F = 2$. Consequently, these states are optimally suited to obtain characteristic values only weakly dependent on external magnetic fields. In contrast, states with $m_\mathrm{F} = -1$ show a by far stronger dependence

that can be calculated to $-2\pi \cdot 1.316(5)\,\mathrm{MHz}$ for $F = 3$ and $2\pi \cdot 1.319(5)\,\mathrm{MHz}$ for $F = 2$. Therefore, these states will be utilized afterwards in order to map the magnetic test field.

5.2.1. Phase-stabilized diode laser system

During the course of this work, a new laser system for two-photon stimulated Raman transitions and spectroscopy has been implemented in the experimental apparatus. The setup and characterization is detailed in the master theses [76, 145]. It embodies two ECDL with laser diodes (M9-785-0150-S50, Axcel Photonics) operated at a wavelength of 780 nm which are red-detuned to the D_2 line. The Raman master laser is locked via an offset lock relative to the spectroscopy master laser of the experiment with a detuning of $\Delta_\mathrm{i} = -2\pi \cdot 9\,\mathrm{GHz}$. The Raman slave laser is superimposed with the Raman master laser and a beat signal is generated using a fast photodiode (G5176-03, Hamamatsu). Stabilization of the slave laser is realized via a phase-locked loop (PLL) based on an ADF4007 chip from Analog Devices which is connected to a reference oscillator that can be tuned in frequency via the experimental control system. Changing the reference frequency allows to precisely set the relative frequency between both Raman lasers to match either the two-photon resonance or include a defined detuning to the transition for spectroscopic measurements. The mean phase noise of the stabilized system has been determined to $\sqrt{\langle\phi^2(t)\rangle} = 125(13)\,\mathrm{mrad}$ [76].

5.3. Raman process for ground-state coupling

5.3.1. Two-photon ground-state transitions

In order to couple the hyperfine ground states $|5\mathrm{S}_{1/2}, F = 2, m_F\rangle$ and $|5\mathrm{S}_{1/2}, F = 3, m_F\rangle$ coherently a two-photon process is utilized as depicted in Fig. 5.2 for $m_\mathrm{F} = 0$ states. Following the level diagram shown in Figure 5.2 (a) two σ^--polarized laser fields with Rabi frequencies Ω_1 and Ω_2 which are stabilized close to the frequency difference of the ground states $\tilde{\Delta}_\mathrm{hfs}$ with an effective detuning $\delta_\mathrm{eff} = \omega_1 - \omega_2 - \tilde{\Delta}_\mathrm{hfs}$ can be used to drive stimulated Raman transitions between $|0\rangle = |5\mathrm{S}_{1/2}, F = 2, m_F = 0\rangle$ and $|1\rangle = |5\mathrm{S}_{1/2}, F = 3, m_F = 0\rangle$ in the depicted case. The detuning Δ_i to the intermediate states $|5\mathrm{P}_{3/2}, F' \in \{2, 3\}, m'_F = -1\rangle$ is usually chosen as large as possible with regard to equation 2.15 of Section 2.1.1 in order to minimize spontaneous scattering processes while maintaining a sufficiently high two-photon Rabi frequency

$$\Omega_\mathrm{2p} = \frac{\Omega_1 \Omega_2}{2\Delta_\mathrm{i}} \tag{5.1}$$

at the same time. Therefore, the limitation is typically given by the available laser power. In the present case $\Delta_\mathrm{i} = -2\pi \cdot 9\,\mathrm{GHz}$ was found to be a good compromise and chosen for the measurements presented in this chapter.
The frequency difference between the ground states $\tilde{\Delta}_\mathrm{hfs}$ depends on coupling to external fields and can be written in terms of the literature value for an unperturbed atom $\Delta_\mathrm{hfs} = 2\pi \cdot 3035.732\,439\,0(60)\,\mathrm{MHz}$ (Table A.1) and the respective shifts as

$$\tilde{\Delta}_\mathrm{hfs} = \Delta_\mathrm{hfs} - \delta_\mathrm{diff} - \delta_\mathrm{C} - \delta_\mathrm{B} \tag{5.2}$$

which includes the differential light shift of the tweezers δ_diff and the Raman laser beams δ_C as well as any shift due to external magnetic fields δ_B. Using a measurement in which the

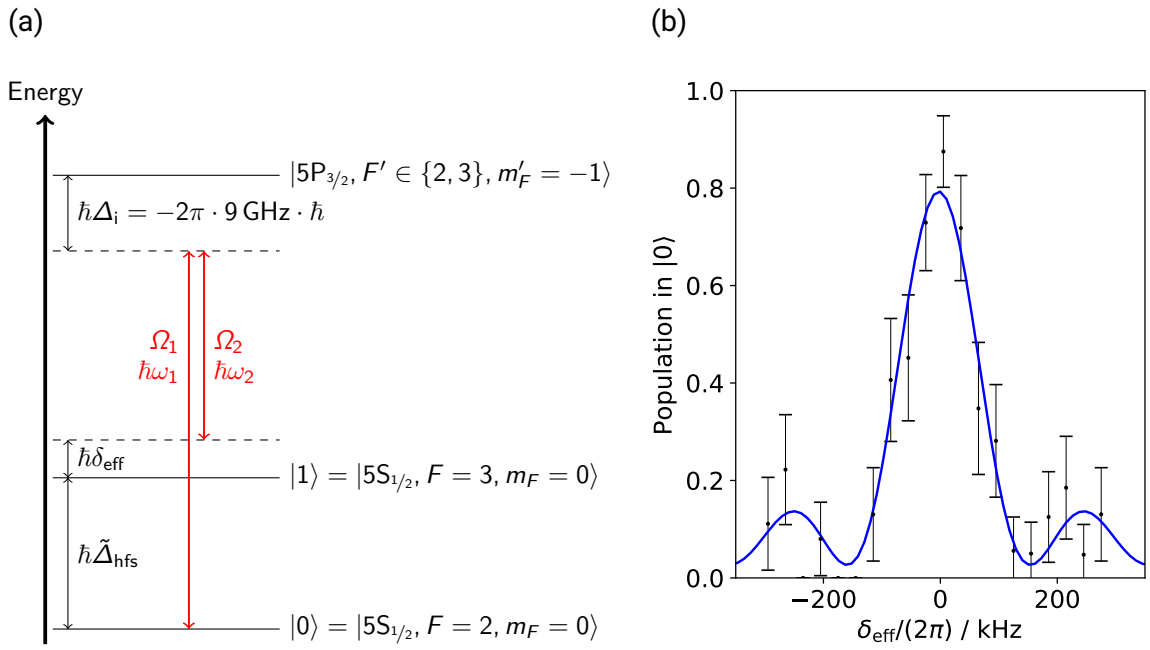

Figure 5.2.: Ground state Raman spectroscopy. Based on a two-photon Raman process the hyperfine ground states $|5S_{1/2}, F = 3, m_F = 0\rangle$ and $|5S_{1/2}, F = 2, m_F = 0\rangle$ are off-resonantly coupled at a detuning $\Delta_i = -2\pi \cdot 9$ GHz to the intermediate state $5P_{3/2}$ (details of the hyperfine structure omitted for clarity). (b) This allows for spectroscopic analysis of the transition and determination of the resonance location ($\delta_{\mathrm{eff}} = 0$) including all energy shifts resulting from magnetic field or light shifts.

atoms are initially prepared in state $|5S_{1/2}, F = 3, m_F = 0\rangle$ one can spectroscopically analyze the two-photon transition via application of a π-pulse to state $|5S_{1/2}, F = 2, m_F = 0\rangle$ before state-selective detection that gives the ratio of atoms that were transferred which works best at resonance. Figure 5.2 (b) shows the resulting signal for one central trap in the array at different detunings where δ_{eff} denotes the effective detuning with the resonance frequency at $\delta_{\mathrm{eff}} = 0$. The solid curve is a fit to equation 4.3 yielding an amplitude of $A = 0.80(3)$ and $\tilde{\tau} = 5.3(2)\,\mu\mathrm{s}$ that is consistent with the configured pulse length of $\tau = 5.4\,\mu\mathrm{s}$. In the light of knowing the location of the resonance frequency further analysis regarding the achievable coupling strength can be conducted.

5.3.2. Ground state Rabi oscillations

Based on the new Raman laser system and optimization of the beam path of the spectroscopy laser which results in an experimentally determined radius of $w = 170(20)\,\mu\mathrm{m}$ at the location of the atoms, the two-photon ground-state coupling strength has been significantly increased. That allows to achieve sub-microsecond π-pulse times in the large-scale array for the typical laser intensity of $I = 5\,\mathrm{W/cm^2}$. This is demonstrated in a measurement where atoms stochastically loaded from the MOT are prepared into $|5S_{1/2}, F = 3, m_F = 0\rangle$ before illumination over a variable duration t with the Raman laser beam. In this period they execute Rabi oscillations between $|5S_{1/2}, F = 3, m_F = 0\rangle$ and $|5S_{1/2}, F = 2, m_F = 0\rangle$. Eventually, the final state is deter-

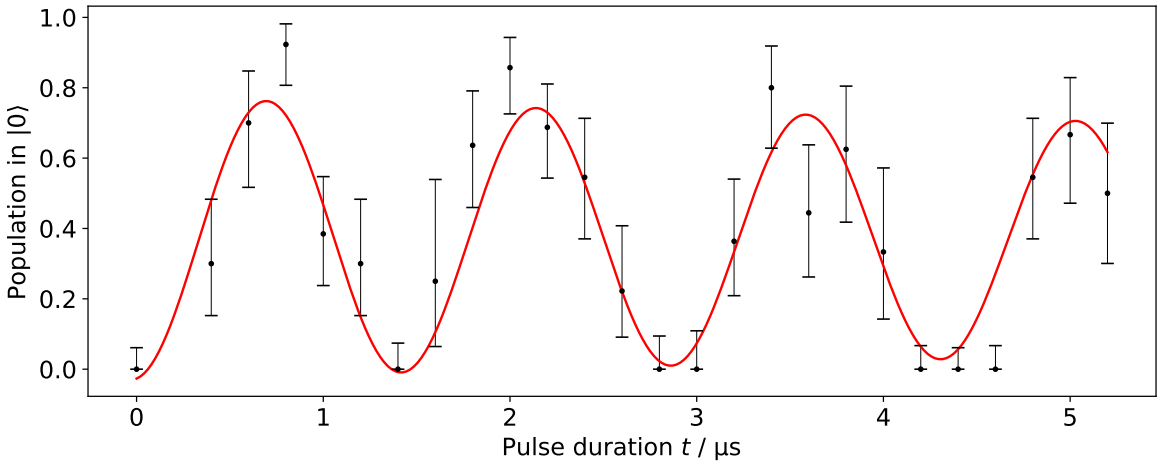

Figure 5.3.: Rabi oscillations between the hyperfine ground states $|0\rangle$ and $|1\rangle$ with sub-microsecond π-pulse duration of individual atoms loaded into a central trap. From the fit to equation 4.4 a Rabi frequency of $\Omega_{2\mathrm{P}} = 2\pi \cdot 692(12)\,\mathrm{kHz}$ with corresponding $\tau_\pi = 722(13)\,\mathrm{ns}$ is obtained.

mined by using fluorescence detection after removing all atoms in the $|5\mathrm{S}_{1/2}, F = 3, m_F = 0\rangle$ state via a pushout laser beam. Figure 5.3 depicts the resulting signal obtained from a central trap in the array. Using equation 4.4 in analogy to the analysis for the Rydberg coupling measurement one obtains a two-photon Rabi frequency of $\Omega_{2\mathrm{P}} = 2\pi \cdot 692(12)\,\mathrm{kHz}$ from a fit as indicated by the solid curve. This corresponds to a π-pulse time of $\tau_\pi = 722(13)\,\mathrm{ns}$. A similar timing is observed in the whole array with respect to the Gaussian intensity distribution along the y-axis in the experimental setup (Fig. 5.1 (a)). In Fig. 5.4 a central 9×9 section of the 361-site array is shown. Within this region the measured Rabi frequencies vary between $\Omega_{2\mathrm{P}}/2\pi = 633(10)\,\mathrm{kHz}$ and $741(15)\,\mathrm{kHz}$. The whole measurement consists of 780 experimental cycles equally distributed over the different pulse durations. Even though there are still variations in the signals between the traps, the statistics is already sufficient to determine the coupling strength to atoms at every site.

Based on this configuration, a spectroscopy technique can be implemented which has several advantages over the way depicted in Fig. 5.2. Using the Ramsey spectroscopy enables to significantly extend the effective measurement time which immediately results in a higher accuracy and has the advantage that the resulting frequency is independent of differential light shifts of the Raman beams which are a source of dephasing in the Rabi scheme. The Ramsey method does only require to apply two $\frac{\pi}{2}$-pulses which substantially reduces the probability for spontaneous processes involving the $|5\mathrm{P}_{3/2}\rangle$ intermediate state. The resulting precision is required for the sensing application presented in the following section as implemented in the experimental platform.

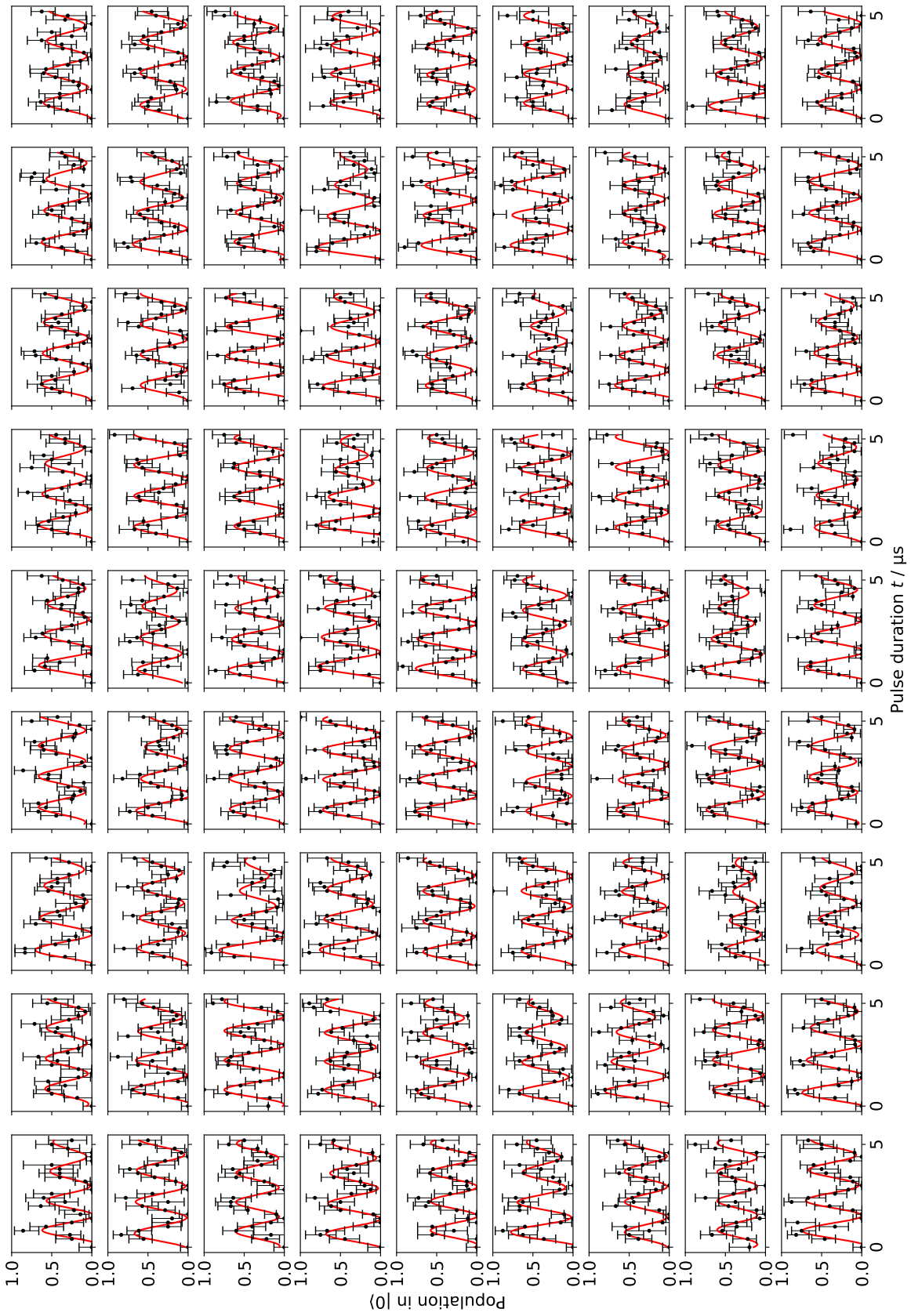

Figure 5.4.: Rabi oscillations between $|0\rangle$ and $|1\rangle$ in the large-scale individual-atom array.

5.4. Ramsey spectroscopy

As demonstrated for atomic ensembles in [74] and for individual atoms in [67], Ramsey spectroscopy [146] finds a wide range of applications in the experimental platform. Characterization measurements for instance allow to measure the differential light shifts of the dipole traps and implement a compensation mechanism or they can be applied to determine the coherence time using the spin echo method [147]. A Ramsey sequence consists of two $\pi/2$-pulses with a variable time of free evolution T in between. This leads to an oscillating probability to find the atom in one of the ground states $|0\rangle = |5S_{1/2}, F = 2, m_F = 0\rangle$ or $|1\rangle = |5S_{1/2}, F = 3, m_F = 0\rangle$ afterwards depending on T. The internal atomic state can be written in terms of the basis states as $|\psi\rangle = a\,|0\rangle + b\,|1\rangle$ with the complex coefficients a and b. Assuming an atom initially prepared in $|1\rangle$ one obtains

$$|a(T)|^2 = \frac{1}{2}\left(1 + \cos\left(\omega_{\mathrm{R}} T\right)\right) \tag{5.3}$$

for the probability to measure the state $|0\rangle$ after the second $\pi/2$-pulse with the Ramsey frequency $\omega_{\mathrm{R}} = |\delta_{\mathrm{eff}}| = |\delta_{\mathrm{2Ph}} + \delta_{\mathrm{diff}} + \delta_{\mathrm{B}}|$ which is equal to the factual detuning δ_{eff} experienced by the atom during the time of free evolution. This includes the detuning $\delta_{\mathrm{2Ph}} = \omega_1 - \omega_2 - \Delta_{\mathrm{hfs}}$ of the laser field to the transition of the free atom and the differential light shift of the tweezers δ_{diff} as well as any shift resulting from an external magnetic field δ_{B}. On the one hand, this offers the possibility to measure the respective physical quantity using the Ramsey technique. Since experiments always consist of multiple realizations to obtain proper statistics these dependencies are, on the other hand, also a source of dephasing in case of cycle-by-cycle fluctuations. The velocity distribution of the atoms loaded into the tweezers from the thermal laser-cooled cloud leads to variations in how deep an atom is finally trapped in the dipole potential between different experimental runs. This results in an inhomogeneous dephasing as discussed in [148] and can be applied with regard to the single-atom quantum array according to the measurements and analysis conducted in [67]. In this case, equation 5.3 can be adapted accordingly

$$|a\,(T)|^2 = C + \frac{A}{2}\Lambda\left(T, T_2^*\right)\cos\left(\omega_{\mathrm{R}} T + \Xi\left(T, T_2^*\right) + \kappa\right) \tag{5.4}$$

which includes a time-dependent amplitude

$$\Lambda\left(T, T_2^*\right) = \left(1 + \left(e^{2/3} - 1\right)\left(\frac{T}{T_2^*}\right)^2\right)^{-2/3} \tag{5.5}$$

and a time-dependent phase factor

$$\Xi\left(T, T_2^*\right) = -3\arctan\left(\frac{T}{T_2^*}\sqrt{e^{2/3} - 1}\right) \tag{5.6}$$

based on a constant for defining the time scale for inhomogeneous dephasing T_2^*. Additionally, equation 5.4 comprises an amplitude scaling A, an offset C as well as a constant phase shift κ. Figure 5.5 shows the result of a Ramsey measurement averaged over the central 3×3 traps. The detuning of the spectroscopy lasers to the hyperfine transition frequency Δ_{hfs} has been set to $\delta_{\mathrm{2Ph}} = 2\pi \cdot 50.00(2)$ kHz and a duration of the $\pi/2$-pulses of $\tau_{\pi/2} = 0.37$ µs is chosen. A fit of equation 5.4 yields $\omega_{\mathrm{R}} = 2\pi \cdot 46.02(4)$ kHz and a time constant for inhomogeneous dephasing $T_2^* = 317(23)$ µs. The discrepancy results from the differential light shift in the tweezers δ_{diff} and magnetic field shift which calculates to $\delta_{\mathrm{B}} = -2\pi \cdot 10.36(8)$ kHz according to equation 2.33

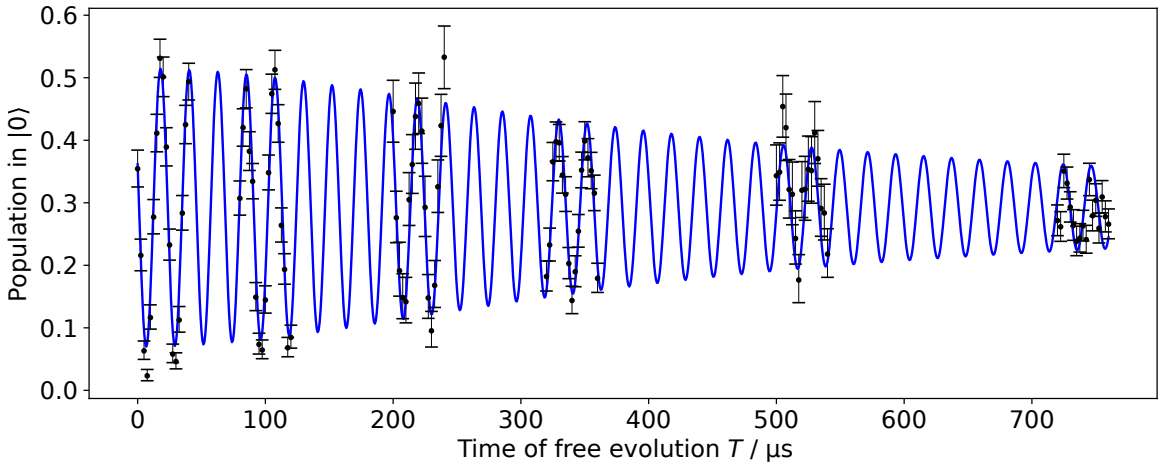

Figure 5.5.: Ramsey measurement averaged over the central 3 × 3 traps. Using a piece wise sampling in the time domain allows to reduce the amount of experimental cycles necessary to determine the Ramsey frequency $\omega_{\mathrm{R}} = 2\pi \cdot 46.02(4)$ kHz and the dephasing time constant $T_2^* = 317(23)$ µs.

using a quantization field of $B_{\mathrm{x,q}} = 283(1)$ µT. This yields a value of $\delta_{\mathrm{diff}} = 2\pi \cdot 6.38(9)$ kHz for the differential light shift. The demonstrated Ramsey measurement already clearly suggests the applicability of the present quantum platform for field metrology. Based on a sensing time of several hundreds of microseconds the differential Stark shift of the atoms in the tweezers could be determined using the information about the strength and impact of the external magnetic field of the quantization axis on the atomic energy levels. In the same way, a magnetic field could be characterized if all the other contributions to energy shifts are known. However, this relies on the precise knowledge of all possible parameters to extract the result due to their interconnection. In the following section, a new technique for magnetic field sensing of a test field will be presented which features a self-calibrating mechanism in order to decouple experimental parameters of the measurement apparatus from the test field.

5.5. 2D magnetic-field sensing with individual atoms

For magnetic-field sensing in the two-dimensional tweezer array the hyperfine ground states with $m_{\mathrm{F}} = 0$ are not appropriate due to their insensitivity to external magnetic fields as discussed in the context of Fig. 5.1 (b). While the stretched states $\left(|5\mathrm{S}_{1/2}, F = 3, m_F = \pm 3\rangle\right)$ exhibit the strongest energy dependence on the magnetic field strength they cannot be used in the current configuration with circular polarized Raman lasers without modifications of the experimental apparatus. However, in the present setup the probability distribution of the occupation of the internal atomic states without initial preparation after loading of the atoms in the dipole trap array and the subsequent fluorescence detection phase shows a strong bias towards states with $m_{\mathrm{F}} < 0$. This can be exploited via optical pumping with π-polarized light along the +y-axis similar to the concept for initialization into $|5\mathrm{S}_{1/2}, F = 3, m_F = 0\rangle$ but for a reduced duration of 300 µs. In this manner, a state preparation efficiency into $|1'\rangle = |5\mathrm{S}_{1/2}, F = 3, m_F = -1\rangle$ of about 30 % is achieved. This state can be easily coupled to $|0'\rangle = |5\mathrm{S}_{1/2}, F = 2, m_F = -1\rangle$ through the two-photon process using the Raman laser configuration at present. According to

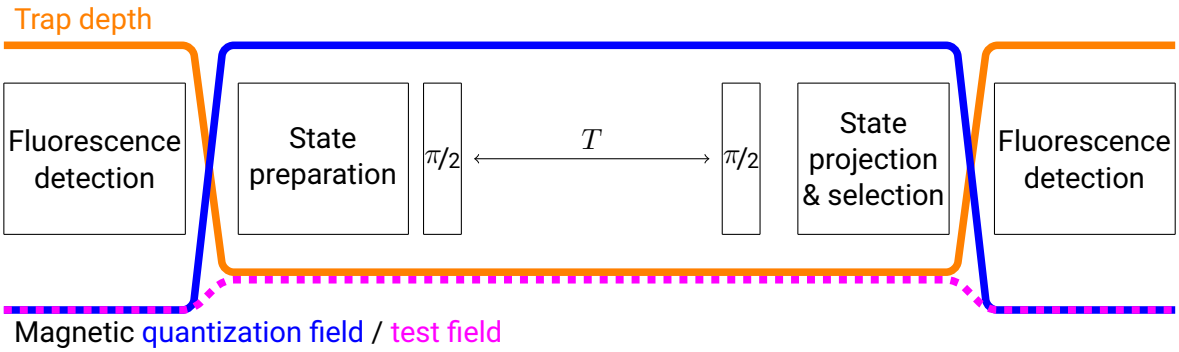

Figure 5.6.: Schematic of a typical measurement cycle. First the magnetic field of the quantization axis as well as the gradient test field is activated while the trap depth of the tweezer array is ramped down by a factor of 6.4. After state preparation to $|1'\rangle = |5S_{1/2}, F = 3, m_F = -1\rangle$ is achieved via optical pumping, a Ramsey sequence with variable time of free precession T in the basis $|1'\rangle$ and $|0'\rangle = |5S_{1/2}, F = 2, m_F = -1\rangle$ is conducted. After removing the atoms in $|1'\rangle$ from the tweezer array the magnetic fields are switched off while the tweezers are ramped up again. Finally, the remaining atoms in $|0'\rangle$ are detected using fluorescence detection.

equation 2.33 the dependence of the two-photon resonance on the magnetic field strength at $B_{\mathrm{x,q}} = 283(1)\,\mu\mathrm{T}$ is $\frac{\partial \delta_{\mathrm{eff}}}{\partial B}|_{B_{\mathrm{x,q}}=283\,\mu\mathrm{T}} = 2\pi \cdot 9.2777(3)\,\mathrm{kHz}/\mu\mathrm{T}$. Based on this ratio, changes of the magnetic field directly convert into a modification of the effective detuning which can be detected using a Ramsey measurement.

5.5.1. Magnetic-field gradient detection in the tweezer array

As a demonstration of the sensing capability of the tweezer setup, the gradient of the field utilized for magneto-optical trapping is characterized using a workspace of 18×15 sites. This amounts to a size of $119\,\mu\mathrm{m} \times 98\,\mu\mathrm{m}$ which is sampled at the $7\,\mu\mathrm{m}$ resolution given by the tweezer pitch. This rectangular area has been selected based on an evaluation of the observed loading efficiency in the 19×19.
Figure 5.6 illustrates the time sequence of a typical measurement cycle. After atom loading and detection of the trap occupation via fluorescence imaging, the magnetic field of the quantization axis is activated while the trap depth of the tweezer array is ramped down by a factor of 6.4. Depending on the respective measurement cycle the test field is either turned on simultaneously or kept deactivated in order to obtain a reference for calibration. After ground state preparation to $|1'\rangle$, a Ramsey sequence with variable time T of free precession with the frequency ω_{R} in the basis $|0'\rangle$ and $|1'\rangle$ is initiated. In this case, a duration of $\tau_{\pi/2} = 0.42\,\mu\mathrm{s}$ for both $\pi/2$-pulses is chosen. After removing the atoms in $|1'\rangle$ from the dipole trap array using the state-selective removal laser, the magnetic fields are switched off while the array traps are being ramped up again. Finally, the remaining atoms in $|0'\rangle$ are identified using fluorescence detection.
Figure 5.7 depicts the results of the field measurement consisting of 14000 cycles with T varied between $2\,\mu\mathrm{s}$ and $110\,\mu\mathrm{s}$ in steps of $\Delta T = 2\,\mu\mathrm{s}$. The order of executing the measurement cycles has been shuffled using a pseudo-random algorithm. As demonstrated in Fig. 5.7 (a) in the example of a central trap of the array at $x = 63\,\mu\mathrm{m}$ and $y = 49\,\mu\mathrm{m}$ the measurement

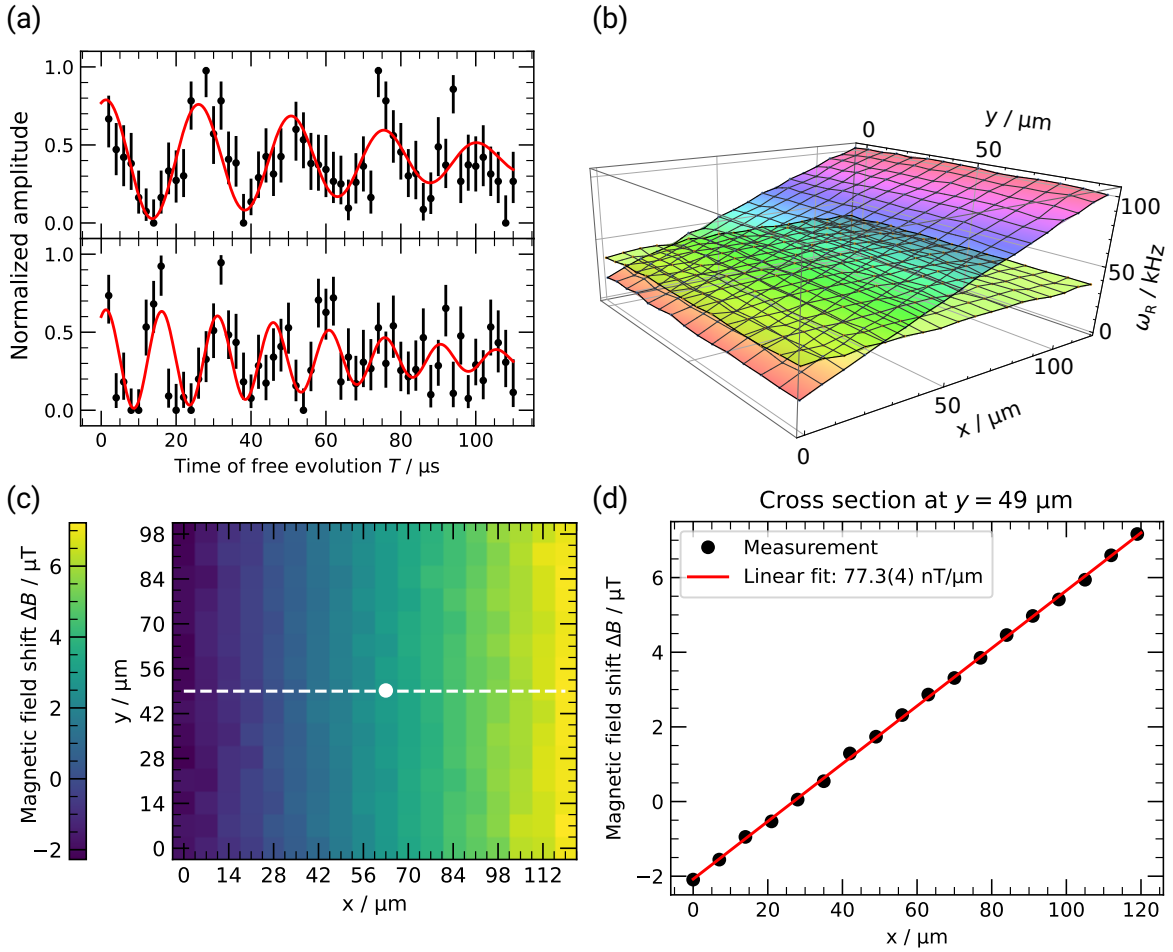

Figure 5.7.: Magnetic field sensing in a two-dimensional array of individual atoms. (a) Using an effective detuning $\delta_{\text{eff}} = 40.0(7)$ kHz measured at the central area of the sensor plane, parallelized individual-atom Ramsey measurements are performed within the large-scale tweezer array as shown in the example of the trap at $x =$ 63 µm, $y =$ 49 µm in the sensor plane. Randomly switching between deactivated (top) and activated (bottom) test field allows to determine the change of the Ramsey frequency caused by the test field due to modification of the effective magnetic field and the resulting shifts of the energy levels connected via the two-photon transition. Based on an approximation of equation 5.7, Ramsey frequencies for the deactivated field of $\omega_{\text{R,ref}} = 40.3(5)$ kHz and $\omega_{\text{R}} = 67.1(7)$ kHz for active test field can be determined in this case. (b) Evaluation of the whole array yields the frequency distribution for both situations in the sensor plane. An active test field shows a gradient along the x-direction while in the deactivated case only minor deviations from a perfectly parallel plane resulting from local variations of the light shift can be detected. These results can be used (c) to create a two-dimensional map of the difference of the magnetic field strength ΔB in both situations (d) from which the magnetic field gradient can be determined via approximation of a linear function. This yields $77.3(4)\,\text{nT}/\mu\text{m}$ for a cross section along the dashed line indicated in (c) which includes the position analyzed in (a).

yields two Ramsey signals for each site. In case of deactivated test field (top) the reference frequency $\omega_{\mathrm{R,ref}}$ can be obtained from a fit which corresponds to the effective detuning δ_{eff}. For activated test field (bottom), a different value for δ_{eff} is determined as the additional magnetic field shifts the energy of the levels depending on the effective magnetic field $\boldsymbol{B}_{\mathbf{eff}} = \boldsymbol{B}_{\mathbf{x,q}} + \boldsymbol{B}_{\mathbf{test}}$ where $\boldsymbol{B}_{\mathbf{test}}$ denotes the test field. In these measurements, a significantly stronger dephasing is observed in contrast to the measurement detailed in Section 5.4 for the magnetically insensitive $m_{\mathrm{F}} = 0$ states which limits the effectively usable time of free evolution to $T \leq 110\,\mu\mathrm{s}$. Therefore, using equation 5.4 to describe the time dependence cannot be justified in the present case as there is a more dominant dephasing mechanism. Instead

$$|a(T)|^2 = A\left(1 + e^{-\frac{\sigma^2 (T-T_0)^2}{2}} \cos\left(\omega_{\mathrm{R}}(T - T_0)\right)\right) + C \tag{5.7}$$

is used as function for the probability to detect an atom in state $|0'\rangle$ after the end of the Ramsey sequence. Assuming that the resonance frequency is perturbed by noise which follows a normal distribution with standard deviation σ a Gaussian damping factor is motivated in this case. A fit of equation 5.7 to the data depicted in Fig. 5.7 (a) yields the solid curves with frequencies $\omega_{\mathrm{R,ref}} = 40.3(5)\,\mathrm{kHz}$ for solely activated quantization field and $\omega_{\mathrm{R}} = 67.1(7)\,\mathrm{kHz}$ in case of additionally enabled test field. When all traps in the workspace are evaluated according to the procedure executed for Fig. 5.7 (a) a detailed map of the frequencies for the calibration as well as the test cycles is obtained which are both shown in Fig. 5.7 (b). While for a deactivated test field a nearly constant Ramsey frequency with an average value of $\omega_{\mathrm{R,ref}} = 2\pi \cdot 38.7(13)\,\mathrm{kHz}$ for the whole sensor plane is measured showing only slight variations due to the differential light shift of the tweezers, an activated test field leads to a frequency distribution with a positive gradient along the quantization axis. Additionally, there is an intersection of the two planes next to $x = 28\,\mu\mathrm{m}$ indicating almost no additional contribution of the test field to the level shift of $|5\mathrm{S}_{1/2}, F = 2, m_F = -1\rangle$ and $|5\mathrm{S}_{1/2}, F = 3, m_F = -1\rangle$. For these traps at $x = 28\,\mu\mathrm{m}$ the difference between the measured Ramsey frequencies for calibration and cycles with activated test field averages to $\omega_{\mathrm{R}} - \omega_{\mathrm{R,ref}} = 1.0(9)\,\mathrm{kHz}$ where the uncertainty gives the standard deviation of the mean value. Then, a Ramsey frequency $\omega_{\mathrm{R}} < \omega_{\mathrm{R,ref}}$ indicates that the test field reduces the effective magnetic field with respect to the reference measurement. Based on the difference between the Ramsey frequencies $\omega_{\mathrm{R}} - \omega_{\mathrm{R,ref}}$ the modification of the effective magnetic field strength $\Delta B = |\boldsymbol{B}_{\mathbf{eff}}| - |\boldsymbol{B}_{\mathbf{test}}|$ resulting from the test field can be calculated for the whole sensor plane using equation 2.30. The mean uncertainty of the frequency differences over the full area amounts to $2\pi \cdot 0.91(27)\,\mathrm{kHz}$ which calculates to a typical magnetic field resolution of $98(29)\,\mathrm{nT}$. As shown in Fig. 5.7 (c), the values for ΔB vary over the sensor plane in analogy to the Ramsey frequencies while the central position analyzed in the context of Fig. 5.7 (a) is indicated by the dot. According to this map, the gradient can be evaluated via approximation of a linear function as shown Fig. 5.7 (d) for the cross section along the dashed line. Based on the values ranging from $-2.1(1)\,\mu\mathrm{T}$ at $x = 0\,\mu\mathrm{m}$ to $7.2(1)\,\mu\mathrm{T}$ at $x = 119\,\mu\mathrm{m}$ a gradient of $77.3(4)\,\mathrm{nT}/\mu\mathrm{m}$ is retrieved. Averaging each column in the sensor area one obtains a mean gradient of $76.9(28)\,\mathrm{nT}/\mu\mathrm{m}$.

Due to the strong contribution of the quantization field to $\boldsymbol{B}_{\mathbf{eff}}$ this measurement directly gives the relative values of $\boldsymbol{B}_{\mathbf{test}}$ along the quantization axis within the sensor plane under the assumption of only a weak component $B_{\perp,\mathrm{test}}$ orthogonal to $\boldsymbol{B}_{\mathbf{x,q}}$. For $B_{\perp,\mathrm{test}} \leq 42\,\mu\mathrm{T}$ the contribution of $B_{\perp,\mathrm{test}}$ to ΔB is below 100 nT and therefore negligible. In this case, the gradient determined in Fig. 5.7 (d) directly represents the test-field gradient along the quantization axis.

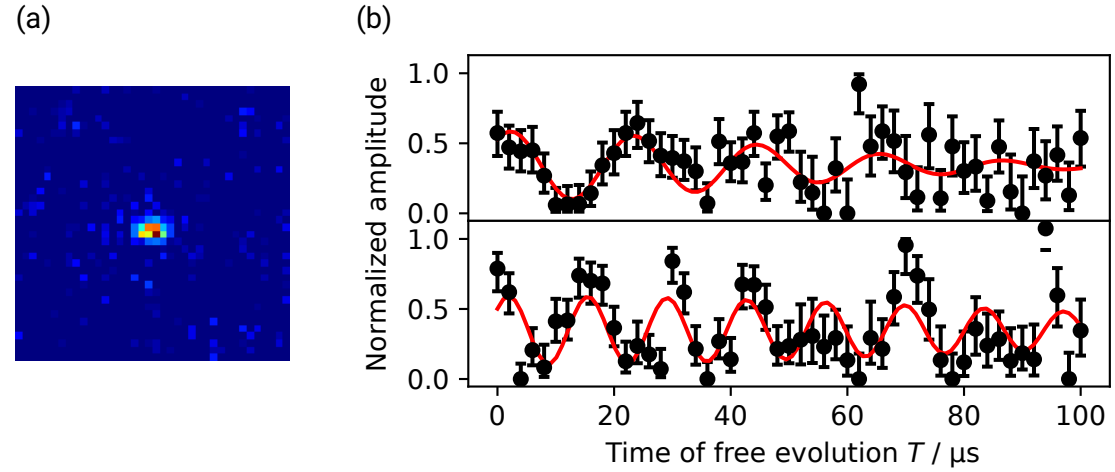

Figure 5.8.: Steerable single-atom probe using the movable optical tweezer. (a) Fluorescence image of an atom in the movable optical tweezer at the sensing location taken prior to the Ramsey detection phase. (b) In analogy to the measurements in the array this is used as the reference image to detect the phase evolution of the superposition state together with the second fluorescence image after the end of the time of free evolution. Based on the same method as used for magnetic field detection in the tweezer array, a signal for calibration with deactivated test field (top) and for the case of activated test field (bottom) is obtained. From these signals, the respective Ramsey frequencies can be extracted via a fit to equation 5.7. This yields $\omega_{\mathrm{R,ref}} = 47.2(19)$ kHz for the calibration and $\omega_{\mathrm{R}} = 73.5(13)$ kHz when the test field is active. From these values, a difference in the magnetic field strength between both situations of $\Delta B = 2.8(3)$ µT can be calculated.

5.5.2. Single-atom probe in an independently steerable optical tweezer

So far, spatial sensing has been limited to the geometric constraints of the array. While that enables parallelized detection in all sites of the sensing area and allows for creation of a detailed map of the field distribution at equidistant points, finer control of the specific positions is vital to enhance the spatial resolution. Using the movable optical tweezer, the restriction to a specific geometry can be surpassed. Based on this system, preparation of a single-atom probe at an arbitrary position within or even outside the area of 19×19 sites can be realized. As discussed in Section 3.2.1 the addressable region of 400 µm × 400 µm which is covered by the tweezer setup can significantly exceed the selected sensor workspace of the dipole trap array of currently 119 µm × 98 µm.
In order to realize single-atom sensing within the tweezer, a trap depth of $U_0' = 1.0(1)$ mK is used during a direct loading process from the optical molasses into the tweezer potential and the subsequent fluorescence imaging before a measurement cycle according to the sequence for detection using the sensor array (Fig. 5.6) is applied, respectively. The trap depth during the measurement comprising state preparation, Ramsey sequence, and state detection is tuned to $U_0' = 200(20)$ µK before it is increased again to the initial value for the final fluorescence detection phase. During these experiments the array is kept deactivated and only loading into the tweezer is executed.
Figure 5.8 (a) shows a fluorescence image of one atom detected within the tweezer which

is obtained in the same fashion as done for the atoms in the array. In the context of this measurement, the tweezer is localized at a position displaced along the quantization axis by $\Delta x = -0.64(62)\,\mu\text{m}$ relative to the array site at $x = y = 63\,\mu\text{m}$. This value for the displacement is extracted from an averaged fluorescence image of the single atom probe compared to the mean image obtained in case of loading into the array. For this position, a value for the contribution of the test field of strength of $\Delta B = 2.8(1)\,\mu\text{T}$ is obtained from the previous measurement within the tweezer array. Figure 5.8 (b) shows the resulting Ramsey oscillations for the calibration (top) cycles in which the test field is not activated and the experimental runs in which both are active (bottom). In this measurement, the time of free evolution is varied between 0 µs and 100 µs in a step size of $\Delta T = 2\,\mu\text{s}$ while all cycles are executed in random order. For both situations, an average value of about 40 atoms has been detected for each setting in the first imaging phase therefore contributing to the respective data point while on average only 6 atoms are retained after the Ramsey sequence. This is a result from the comparably low efficiency for initial state preparation into $|5S_{1/2}, F = 3, m_F = -1\rangle$. Nevertheless, the signals for both situations can be clearly identified and using equation 5.7 allows to extract the respective Ramsey frequencies $\omega_{\text{R,ref}} = 47.2(19)\,\text{kHz}$ for the calibration and $\omega_{\text{R}} = 73.5(13)\,\text{kHz}$ during sensing with activated test field. Using the same evaluation procedure as for the measurement within the array yields $\Delta B = 2.8(3)\,\mu\text{T}$ from the single-atom probe which matches the expectation according to the measurement within the tweezer array. In order to estimate the spatial resolution of the single-atom sensor a localization of the individual atom within the region with dipole potential $U_{\text{D}} \geq 0.8(1) \cdot U_0$ of a trapping potential with depth U_0 is assumed [57, 149]. Given a tweezer waist of $2.0(1)\,\mu\text{m}$, this results in a resolution of 1.3(4) µm. This could be easily enhanced into the sub-micrometer regime via decreasing the waist to 1.45 µm which is obtained for the tweezer array.

5.6. Conclusion

In this chapter, a new application for the quantum platform of this thesis has been presented: single-site resolved magnetic field sensing based on individual-atom probes within a large-scale two-dimensional tweezer array. Featuring a detection workspace of 18×15 sites which covers an area of $119\,\mu\text{m} \times 98\,\mu\text{m}$ the present configuration provides a spatial resolution of 7 µm and a sensitivity of 100 nT. Based on the Ramsey technique the impact of external magnetic fields on the internal atomic states could be traced back to a frequency measurement by optical means which can be executed with high precision and is easily accessible in the experimental setup. This approach found its immediate application in the characterization of the gradient field used in the experimental apparatus for magneto-optical trapping. Applying a self-calibrating technique allowed for ruling out dependencies on external parameters such as light shifts of the internal states due to the trapping potentials as well as environmental conditions, e.g. weak additional static magnetic fields. Furthermore, this renders the measurement result insensitive to the absolute value of the magnetic field strength of the quantization axis over a wide range. Using the movable optical tweezer, sensing of the gradient field independent of the atom array has been demonstrated which is in perfect agreement with the measurement executed via parallelized detection using the tweezer array. Based on the large addressable region of more than $400\,\mu\text{m} \times 400\,\mu\text{m}$ this enables to significantly extend the detection area in future measurements. Additionally, as the movable tweezer can be positioned at arbitrary locations within the addressable area this provides extended flexibility in choosing the spot of interest. Furthermore, using the array traps as a reservoir for loading into the movable tweezer in

combination with selective detection of the single-atom probe offers an additional perspective for optimization which would directly result in a significant speed up of the measurements.
Based on Ramsey spectroscopy, the sensitivity of the magnetic field measurements strongly depends on the duration of free precession used to determine the Ramsey frequency. In the present setup a maximum available time span of 110 µs has been used due to the stronger dephasing observed for the coupling of hyperfine states with magnetic quantum number $m_\mathrm{F} = -1$ in contrast to the magnetically insensitive $m_\mathrm{F} = 0$ states. Additional analysis and characterization measurements are required in order to determine the cause for this and find ways to extend the sensing duration. The present platform offers a great potential for further exploration. Starting with an improved state preparation should immediately allow for increasing the signal amplitude by at least a factor of 3 based on the currently observed initial state preparation efficiency of about 30 %. As this has direct impact on the signal-to-noise ratio a significantly increased detection period can be expected. Additionally, the spin echo method [147] provides a tool for compensation for inhomogeneous dephasing mechanisms. In [67] this technique allowed for a substantial extension of the dephasing time in the experimental platform. Enhanced sensitivity can also be expected from changing to basis states with higher m_F quantum number which are intrinsically more sensitive to magnetic fields leading to stronger frequency shifts. Using a pair of Raman laser beams with π- and σ-polarized light would allow for driving $|5\mathrm{S}_{1/2}, F = 2, m_F = -2\rangle \rightarrow |5\mathrm{S}_{1/2}, F = 2, m_F = -3\rangle$ transitions with 2.5 times higher response to changes in the magnetic field strength.
Due to the principal technique, the current setup only shows significant sensitivity along the quantization axis which has the strong benefit that the component of the magnetic test field along the direction of the quantization axis can be determined if the orthogonal components are not too strong. In order to obtain comprehensive three-dimensional sensitivity yielding the magnetic field vector in case of an arbitrary orientation in space, additional measurements for differently aligned quantization axis can be executed utilizing the readily available coils at the vacuum apparatus (Fig. 2.4) and respectively directed spectroscopic beams through the various optical ports. Combined with the versatile features of the present platform this provides potential for even further extension. Parallelized gradient measurement in a steerable array in the fashion demonstrated in [55, 118], smaller tweezer waists using a microscope objective with a higher numerical aperture in combination with interleaved arrays [118] and the application of movable tweezer sensing offer potential for detection with massively increased spatial resolution. Even more, exploiting the Talbot planes after extension of the setup to 3D prepares the ground for a fully featured three dimensional magnetic field sensor.

6. Novel concepts: Digital micromirror devices and 3D printing

The presented micro-optical tweezer platform can be utilized on a broad basis and in each of the previous chapters various novel developments have been demonstrated which already found immediate applications. While a variety of possible optimization measures have been discussed in the respective contexts, this chapter deals with new concepts that can be integrated in the near future and will allow for an yet unprecedented flexibility in the experimental apparatus. In particular, with respect to applications in quantum computation and quantum simulation, versatile tweezer geometries with individual-site control are essential for obtaining the necessary degree of flexibility for the envisaged experiments. This includes the implementation of recently developed protocols for error correction based on topological color codes [104] or the dynamic adaption of the tweezer configuration which is crucial to mimic a certain different quantum system during a simulation experiment. This results in the requirement for precise mapping of features, such as domain boundaries but also includes artificial imperfections that make it possible to analyze the impact of defects as they can significantly alter the properties of a quantum system [150, 151].
Off-the-shelf microlens arrays manufactured via lithographic etching are perfectly suited for the setup of large-scale systems as discussed in Chapter 2 and are available in different variants including lenses arranged in a quadratic grid or exhibiting hexagonal packing. Currently reaching an order of 10^6 lenslets, this technique renders the present tweezer platform massively scalable while providing a stable configuration with high-quality focused beam dipole traps. At the same time, this reduces the flexibility regarding short-term modifications of the tweezer arrangement without additional effort.
In this chapter, methods for extended flexibility in the creation of tweezer geometries for the present micro-optical platform are evaluated. Due to the direct correspondence between a microlens and the respective diffraction limited focus, controlling the illumination of each microlens individually allows to alter the tweezer structure based on the fundamental array geometry. This has been realized based on a liquid-crystal (LC) spatial light modulator (SLM) for atomic ensembles in a previous setup [54]. While LC-based phase modulators are more power efficient in the creation of tweezer arrays [152] SLMs based on individually switchable micromirrors offer typically at least an order of magnitude higher update rate [153].
Therefore, one of the key aspects demonstrated in this chapter is the utilization of DMD-based addressing for enhanced site-selective control of microlens-based tweezer arrays. This will be introduced at first before precise individual-site addressing is demonstrated. While this method alone, however, still restricts the available tweezer arrangements and fundamental changes of the pattern can require a replacement of the microlens array, a novel development based on a combination with the emergent technology of 3D printing is presented. This hybrid approach exhibits unprecedented flexibility for the tweezer platform as it enables fast replacement of a microlens array based on rapid-prototyping.

6.1. Parallelized single-site addressability based on spatial light modulation

6.1.1. Site-selective illumination of microlenses using digital micromirror devices

Quantum information experiments based on individual-atom array platforms rely on precise control of the internal and external degrees of freedom of each atom at every site. As coherence in these systems is a precious resource, rapid response time is required and operations should preferably be implemented in a parallelized fashion. The unique microlens-array-based platform presented in this thesis profits from the stability involved with the ultimate correspondence between each tweezer site and its respective microlens. This connection provides a comprehensive channel of control to the atom-light-interaction via spatial modulation of the light fields passing the individual microlenses. As illustrated in Fig. 6.1(a), a digital micromirror device (DMD) can serve as an SLM to independently control the illumination of every microlens. This technique can be utilized to dynamically alter the geometry of a tweezer array based on the microlens-generated foci between or even within experimental cycles. The DMD system used in this thesis is the Lightcrafter EVM module by Texas Instruments which is a micro projector with an embedded Linux system controllable over Ethernet via USB. After removing the LED light engine, the DMD unit can be integrated into custom optical setups. The area of the micromirror array measures 6.57 mm x 3.70 mm and features 608 x 684 quadratic mirrors. As depicted in Fig. 6.1(b) their pitch amounts to $\mathcal{D} = 7.64\,\mu\text{m}$ along mirror edges and they can be individually tilted between two distinct orientations of $\pm 12°$. Consequently, the state of each micromirror can be simply encoded in one binary value and the configuration of a whole array is saved in a standard 1-bit image format which is used for upload to the DMD unit via the USB interface. This module provides an on-board storage for 96 of those patterns in the native resolution of the device which allows for sequential pattern change that is specified at a rate of up to 4 kHz. As analyzed in detail in [155], this rate is dependent on the number of patterns and was measured to vary between 4.6 kHz for up to 24 stored configurations and 2.7 kHz if, for instance, the maximum of 96 is stored. Therefore, even for the lower rate far more than two hundred switching operations can be executed during the coherence time of about 100 ms which is measured for the present setup [57].

6.1.2. Versatile tweezer geometries using DMD-based addressing

The aforementioned technique for single-site control can be adapted for usage in the current experimental apparatus. This will be analyzed in detail in this section based on the setup of a module which can be integrated into the experiment and has been realized in the context of this work and built in the course of the master thesis in ref. [156]. In order to investigate new geometries in the experimental platform, a microlens array with a hexagonal symmetry (MLA3, see Table 2.1) is selected, featuring lenses with a pitch of $d = 161.5\,\mu\text{m}$ and a radius of curvature of $R_c = 2.05\,\text{mm}$. Figure 6.2 (a) shows the details of the setup for the implementation of DMD-enhanced tweezer control. A laser beam with a wavelength of $\lambda = 796.7\,\text{nm}$ is deployed by a single-mode optical fiber using an air-spaced triplet (TC12APC-780, Thorlabs) which results in a beam radius of $w = 1.2\,\text{mm}$. After passing a combination of $\lambda/2$-plate and polarizing beam splitter to ensure proper linear polarization and an additional beam sampler for the purpose of intensity stabilization, the DMD system is illuminated under an incident angle of $\alpha = 26°$ to the DMD surface normal. This leads to the third order of diffraction being

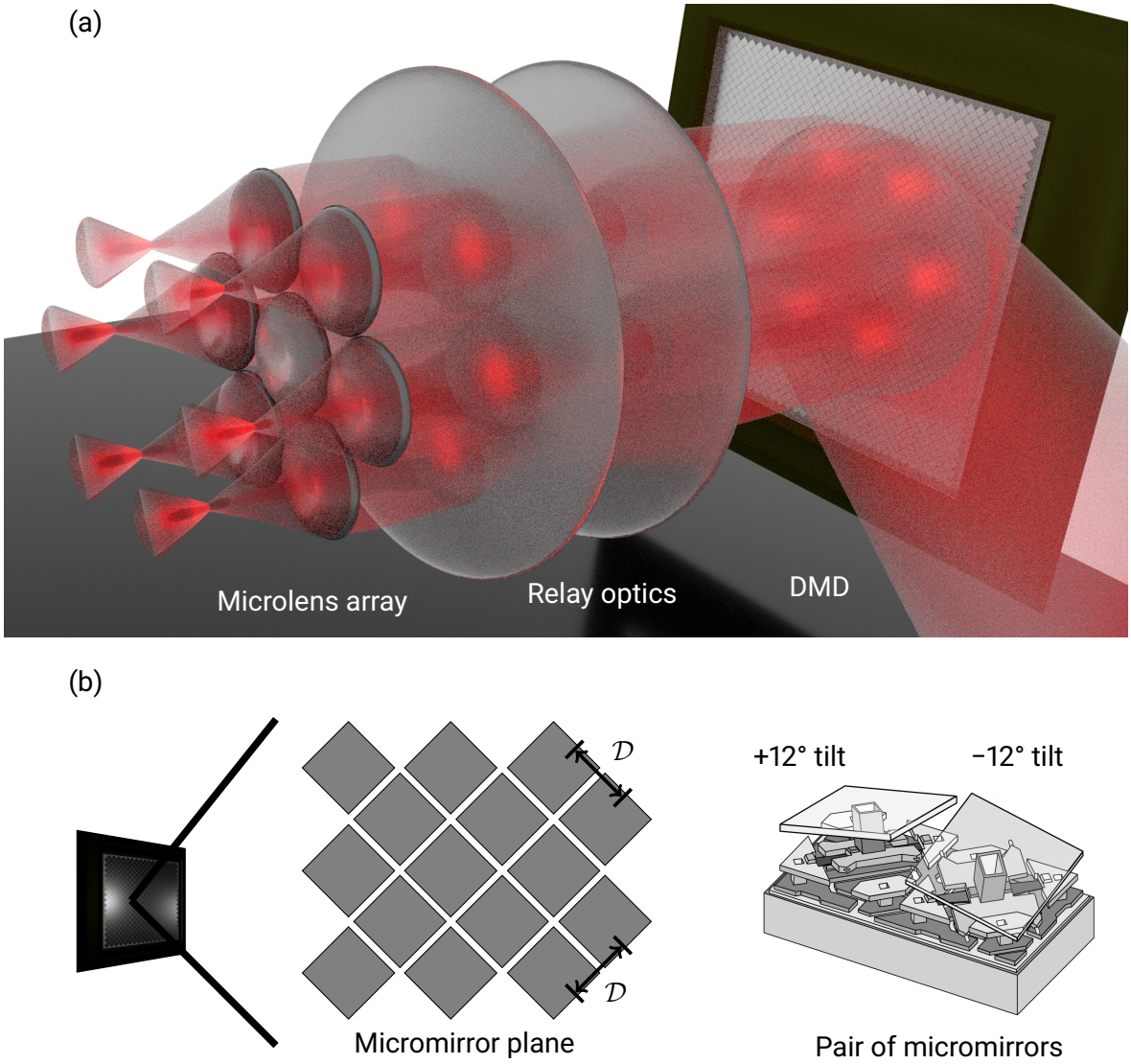

Figure 6.1.: Principles of microlens array addressing using DMD-based spatial light modulation. (a) The Gaussian intensity distribution of a laser beam is modified by a DMD in order to selectively control the illumination of each microlens. Due to the mapping of the DMD plane onto the microlens array via relay optics, the light field amplitude passing each microlens is directly associated with a distinct circular region on the DMD which comprises typically many hundreds of micromirrors. (b) The quadratic mirrors have a pitch of $\mathcal{D} = 7.64\,\mu\text{m}$ along the edges and can be individually oriented into two distinct directions (±12°). Consequently, foci can be switched on and off in a straightforward fashion via flipping the corresponding mirrors. The schematic illustration of the two mirrors in (b, right) is adapted from [154].

deflected orthogonally to the DMD surface parallel to the optical axis of the subsequent optical setup while all other diffraction orders are blocked using an aperture stop. The efficiency of the DMD section amounts to $\eta = 33\,\%$ where the losses are attributed to the deviation of the diffraction angle from the direction of specular reflection off a single mirror (24°), light

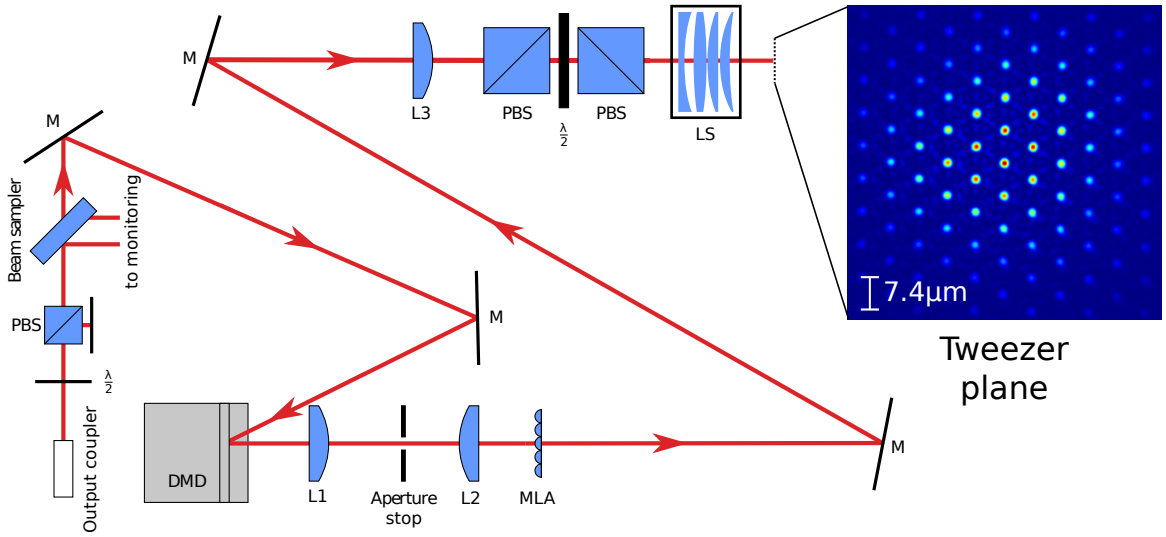

Figure 6.2.: Experimental setup for DMD-based microlens addressing. A laser beam delivered by an optical fiber is defined to linear polarization using a waveplate and a polarizing beam sampler (PBS) before a small fraction of light is taken with a pick-off for power monitoring and implementation of a intensity stabilization. The DMD is then illuminated under an incident angle of 26° which leads to the first order of diffraction being deflected orthogonally to the DMD surface along the optical axis of the subsequent part of the setup. All other diffraction orders are blocked by an aperture stop. Using a combination of achromatic doublets L1 and L2 the DMD surface is mapped onto the microlens array which leads to the association of a certain area on the DMD with a specific microlens in the array whose focal plane is reimaged using an achromatic doublet L3 and a microscope objective comparable to the one implemented in the experimental apparatus LS. Due to the additional PBS before the microscope objective a movable optical tweezer can be included in a straightforward way.

distributed into other orders of diffraction as well as finite window or mirror reflectivity and filling fraction. A confocal telescope composed of two achromatic doublets L1 and L2 with focal lengths of $f_{\mathrm{L1}} = 50\,\mathrm{mm}$ and $f_{\mathrm{L2}} = 30\,\mathrm{mm}$ is employed to map the DMD mirror surface onto the microlens array. The focal plane of the array is demagnified using an achromatic doublet L3 with focal length $f_{\mathrm{L3}} = 750\,\mathrm{mm}$ and a microscope objective LS with the effective focal length $f_{\mathrm{LS}} = 37.5(10)\,\mathrm{mm}$ and a numerical aperture of $NA = 0.25(2)$. The latter is similar to the one implemented in the experimental apparatus but optimized for operation without the window of the vacuum chamber. Two polarizing beam splitter cubes allow for a straightforward superposition of the array beam with a movable optical tweezer (not shown) in the same fashion as demonstrated in Chapter 3. The inset shows an image of the demagnified focal plane with activated illumination of all lenses in the central region. This results in typically 876(7) mirrors being associated with each lenslet. This number is not equal for all lenses since the hexagonal array symmetry differs from the rectangular alignment of the micromirrors. The tweezer pitch is determined to $p = 7.4(2)\,\mu\mathrm{m}$ and the spots measure an average $1/e^2$-waist of $w_0 = 1.33(3)\,\mu\mathrm{m}$. These small waists are well-suited to serve as optical tweezers for trapping of individual atoms after collisional loading as discussed in Section 2.5

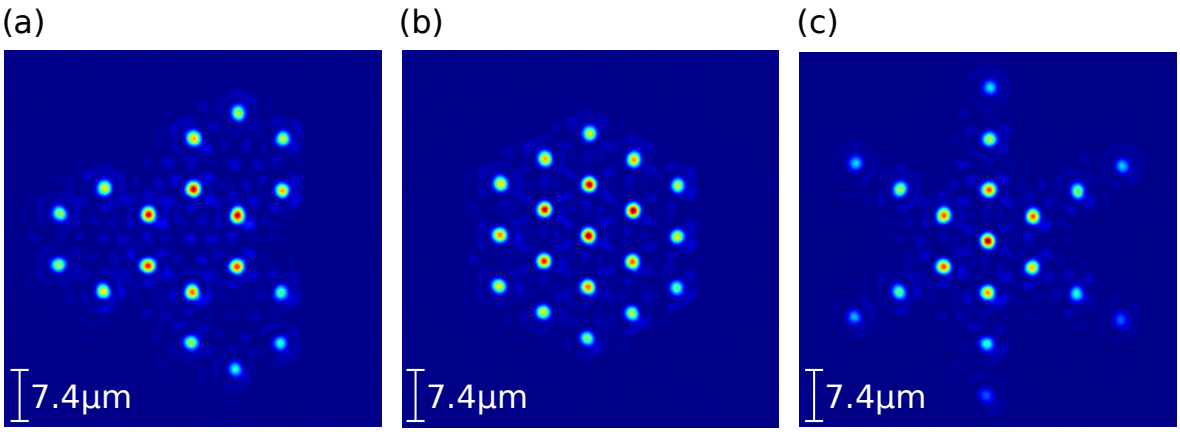

Figure 6.3.: Versatile tweezer geometries. Utilizing the DMD-based site-selective addressability, a wide range of tweezer patterns can be configured without modifications on the optical setup. This includes the arrangement of (a) graphene-like structures, (b) constrained sub-arrays, and (c) star-shaped geometries.

and the spatial separations are ideal to analyze Rydberg interactions in the experimental setup within the blockaded regime (Section 2.6).
Based on the mapping between each focus and the light directed by a certain group of DMD mirrors through the respective lenslet, the native pattern presented in Fig. 6.2 can be reconfigured in a straightforward way just via flipping the associated groups of micromirrors. Activating only the illumination of selected lenses, versatile trap geometries can be created as shown in Fig. 6.3. This grants access to graphene-like patterns (a) as well as compact clusters with clearly defined boundary (b) or star-shaped structures which provide an interesting arrangement for analysis of coherent excitation transfer based on XY spin exchange [47] (c).

6.1.3. Site-selective tweezer intensity optimization

The benefit resulting from spatial light modulation is not only based on binary control over the tweezer spots. This technique also allows for fine tuning of the light field amplitude illuminating each lenslet. As demonstrated in Fig. 6.4 in the example of the central focus, the tweezer intensity of each site can be dynamically controlled through flipping a pseudo-randomly chosen subset of mirrors for every spot such that they deflect the incident light away from the optical path that leads to the microlens array. For convenience, these mirrors are defined as ”deactivated” in the following while the others are termed as being ”active” since they contribute light to the trapping geometry. This enables to tune the intensity from the value obtained in case of activation of all micromirrors associated with this spot down to 4.9(1) % without impairing the quality of the focus where only 20 % of the respective mirrors need to be activated. Combined with the large number of 876(7) micromirrors per lens this approach of random selection ensures that the effective numerical aperture is maintained and, consequently, the waist of the tweezer spots is kept unaffected. In order to quantitatively understand the intensity dependence on the number of activated mirrors, a simulation using wavefront propagation has been executed which matches the measured values to better than 6 % over the full span of possible values of intensity.
This can also be understood qualitatively. In general, the intensity distribution $g(x, y)$ within

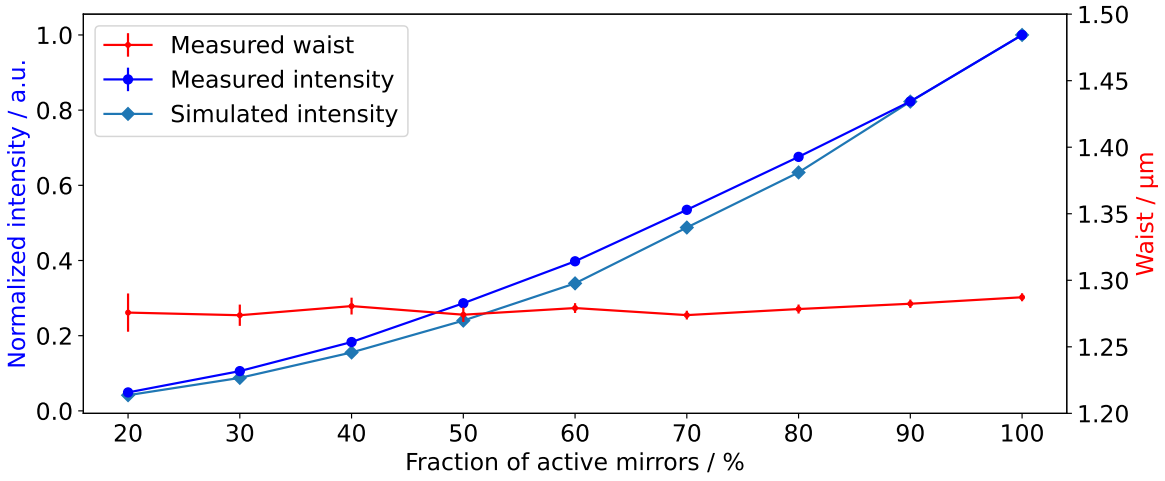

Figure 6.4.: Intensity adaption in the example of the central focus of the region depicted in Fig. 6.3 (b). Flexible control of the focus intensity can be realized via flipping a random set of mirrors such that they do not contribute to the illumination of the respective microlens. Due to the high number of 876(7) mirrors per lens tuning can be achieved on a 0.1 % level within a ratio of activated mirrors ranging from 20 % to 100 % without impeding the quality of the tweezer foci leaving the waist unchanged. The scaling between active mirrors and relative intensity is in good agreement with the expected quadratic dependency (equation 6.2) and is confirmed by a simulation of a two-dimensional analysis of a plane with random wave propagating through a lens with the experimental parameters.

the focal plane of a lens illuminated by a plane wave propagating along the z-axis can be described in terms of the point spread function (PSF)

$$g(x,y) = A_0^2 \left| \iint p(s,t) e^{-i\frac{sx+ty}{f}} dsdt \right|^2 \tag{6.1}$$

with the focal length f of the lens, an amplitude A_0 and the optical axis at $(0,0)$. In case of a circular lens with radius r the pupil function $p(s,t)$ defines the field amplitude illuminating the lens being 1 for $s^2+t^2 \leq r^2$ and 0 otherwise. For the intensity in the focus, i.e. $x = y = 0$, one immediately finds

$$g(0,0) = A_0^2 \left| \iint p(s,t) dsdt \right|^2 \approx A_0^2 \left| \sum_{i,j}^{N_x,N_y} P_{ij} \right|^2 \tag{6.2}$$

when dividing the lens plane into an $N_x \times N_y$ quadratic grid with elements each assigned to a mirror which can be chosen to contribute to illumination of the microlens ($P_{ij} = 1$) or not ($P_{ij} = 0$). Consequently, $g(0,0)$ has a quadratic scaling with the number of activated mirrors that is shown to very good approximation for the data in Fig. 6.4. This technique can be immediately used to compensate for uneven intensity distributions on the microlens array which are typical for Gaussian beams delivered by standard single-mode optical fibers.

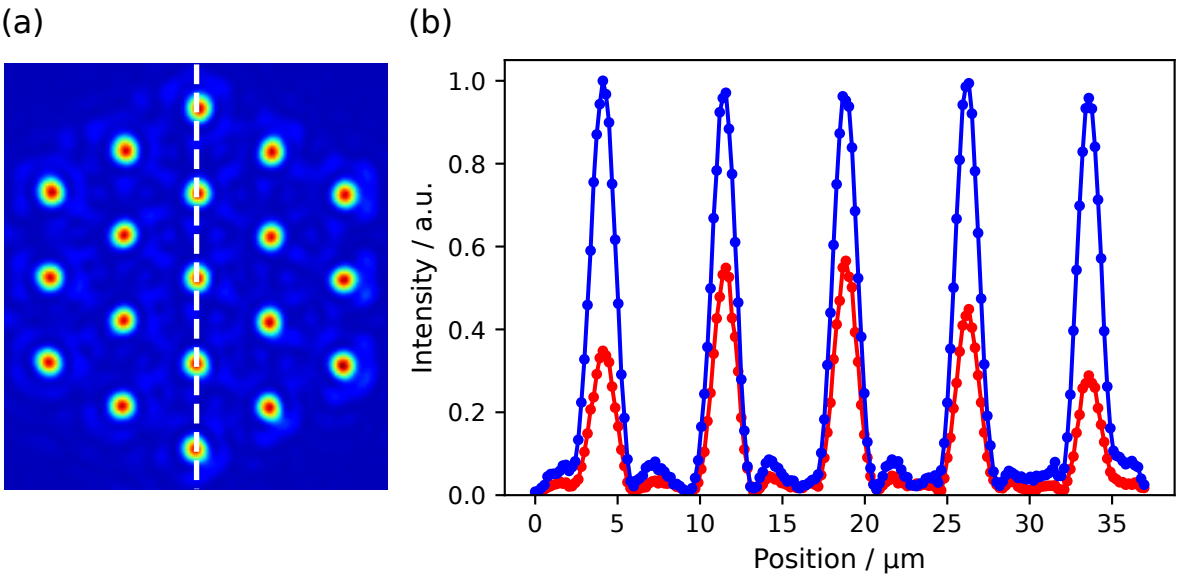

Figure 6.5.: Balancing of the tweezer intensities based on site-selective trap depth control. (a) Resulting intensity distribution in the tweezer plane after adjustment within a 19-site structure in the central region of the array. The cross section indicated through the dashed line given by the blue curve in (b) shows the balanced depths of the diffraction limited tweezer spots. Without individual setting of the ratio of active mirrors per lens, the focus intensities vary due to the Gaussian profile of the beam illuminating the microlens array. This is reflected by the red curve depicting the situation in which 50 % of mirrors associated to each lenslet are activated.

Balancing of non-uniform tweezer intensities in the dipole trap array

Along with a Gaussian intensity distribution on the microlens array there are intensity variations of the foci in the tweezer plane which result in uneven trap depths. As a consequence, the resonance frequencies to transitions connected to the ground states do not shift equally for all sites which needs to be considered during addressing with external laser fields depending on the respective use case. For instance, taking the configuration depicted in Fig. 6.3 (b) into account and assuming $P = 500\,\mathrm{mW}$ available laser power after the optical fiber the trap depths which can be calculated from the intensity distributions vary from $U_0 = 3\,\mathrm{mK} \cdot k_\mathrm{B}$ in the center to $U_0 = 1.5\,\mathrm{mK} \cdot k_\mathrm{B}$ regarding the shallowest trap in the boundary of the compact tweezer geometry. In Fig. 6.5 flexible site-selective intensity control is demonstrated by means of this pattern comprising the 19 central traps. As detailed in the master thesis [156], an automatic optimization routine can be executed which adapts the intensity of the tweezers to a certain depth based on the values retrieved from an image taken with a monitoring camera. After the ratio of active mirrors per lens is individually adjusted, one obtains the final configuration shown in Fig. 6.5 (a). The standard deviation of all 19 traps to their mean intensity is below 2 % while 66 % of the mirrors which are assigned to the central trap are left activated. Figure 6.5 (b) depicts the cross section through the tweezer plane indicated by the dashed line in Fig. 6.5 (a) for the situation without optimization in which the ratio of active mirrors is set to 50 % for all lenses associated to the pattern (red) and after the equalization process (blue). This demonstrates the high level of site-selective control resulting from the

DMD-based spatial light modulation while maintaining the quality of the well-defined focal spots.

6.2. Freely definable geometries using 3D printing and DMD-based spatial light modulation

As demonstrated in the prior chapters, microlens arrays with a lens diameter on the order of 100 µm are ideally suited to fit into the current experimental apparatus, yielding typical tweezer separations of about 10 µm or below after demagnification through the reimaging optics. Additionally, a combination with the DMD technology enables parallelized single-site addressability at a kilohertz rate and grants access to versatile geometries based on the microlens array in use. While commercially available microlens arrays typically feature quadratic or hexagonal grid symmetries, there are applications where extended control over the exact geometry is desired. Even though the flexible implementation in the experimental apparatus allows for an easy modification of the fundamental trap geometry via replacement of the microlens array, the standard manufacturing process lacks short-term availability and involves the production of expensive lithographic masks. In order to overcome these constraints, two powerful state-of-the art technologies are combined in the present section: rapid prototyping of user-defined microlens arrays using 3D dip-in direct laser writing [157, 158] and the DMD-based single-site addressability introduced in the previous section [155, 156]. This hybrid approach profits from the intrinsic stability of the microlens-generated foci while obtaining the additional flexibility for dynamic in-situ modifications of the tweezer pattern. In order to propel this technological symbiosis towards implementation in the experimental apparatus, a novel setup has been developed which features a 3D-printed microlens array with an innovative geometry combining hexagonal and quadratic grid packing.
The results presented in this section emerged from a cooperation with Professor Harald Gießen's group at the University of Stuttgart and have been published in OpticsExpress [159].

6.2.1. Creation of micro-fabricated optical elements using direct laser writing

The typical production process of large-scale microlens arrays used in the experimental setup is based on lithographic etching which allows for scalable manufacturing of hundreds of thousands of lenslets. This is perfectly suited if the lens pattern is precisely known in advance such that the investment into expensive lithographic masks are kept within limits. Consequently, for rapid prototyping and more flexibility in defining the lens shape, the emergent technology of 3D printing offers a tremendous potential. Based on femtosecond direct laser writing, versatile dielectric structures can be created with a typical resolution of 100 nm [160, 161]. Due to this precision, creation of diffractive optical elements [162] is possible and imprinting of free-form optics can be realized on glass substrates and optical fibers [158] as well as directly on light emitting diodes [163]. As it can take only a few hours from design to production and verification until a component is ready to use, this technology provides the possibility for short-term installation of new optics in the experimental setup and is ideally suited for rapid prototyping.
The principle process of 3D laser writing used for the manufacturing of the microlens array presented in this work is shown in Fig. 6.6 and is based on light-induced polymerization of a photoresist due to illumination of a focused laser beam. While the photoresist is transparent for a single photon from light at a wavelength $\lambda = 780\,\mathrm{nm}$ a two-photon process can induce

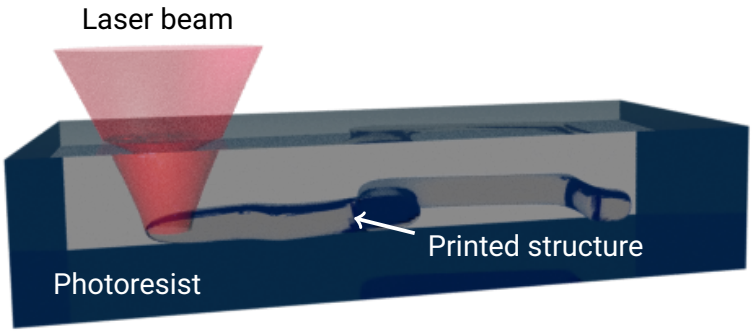

Figure 6.6.: Schematic illustration of the principle of direct laser writing. A focused laser beam is moved withing the photoresist and is absorbed via a two-photon process which is strongly intensity-dependent. This leads to the exposure of the resist in a distinct region (voxel) and its polymerization which allows for printing complex structures with high accuracy.

transitions from a ground to an excited state by simultaneous absorption of two photons from the incident light field resulting in the exposure and polymerization of the resist. The rate R at which these events occur is given by [164]

$$R \propto \Im\left[\chi^{(3)}\right] \cdot I^2 \tag{6.3}$$

and depends on the imaginary part of the complex third-order susceptibility $\chi^{(3)}$ of the specific material, i.e. the photoresist, as well as on the square of the light field intensity I. Therefore, using a tightly focused laser beam allows for well localized excitation within a volume element, a so-called voxel. Printing on a substrate can then be realized by a thin layer of photoresist between the substrate and the objective lens. Using a beam steering system in combination with movement of the substrate itself parallel to the optical axis utilizing a piezo-stage provides the flexibility for three-dimensional adjustment of the voxel within the printing region.

6.2.2. Design parameters and manufacturing process

The microlens array is designed to be tailor-made for a next-generation Rydberg quantum simulation architecture. Due to anisotropic interaction potential V_{int} of Rydberg states with orbital angular momentum $L > 0$ and strong dependence on the interatomic distance R, the array is designed to feature a region with a quadratic grid as well as a region with a purely hexagonal symmetry and a transition between them. This geometry can serve as an ideal testbed to investigate van der Waals type $\left(V_{\text{int}} \propto R^{-6}\right)$ or resonant dipole-dipole coupling $\left(V_{\text{int}} \propto R^{-3}\right)$ in domain boundaries with areas of blocked and unblocked dynamics. Figure 6.7 (a) shows the design schematic for the 3D-printed microlens array comprising 97 circular shaped spherical lenslets. As illustrated, a lens pitch and diameter of $d = 110\,\mu\text{m}$ has been chosen. The array is manufactured using a commercially available two-photon femtosecond lithography system (Photonic Professional GT, Nanoscribe) and the microlenses are sequentially imprinted on a fused silica substrate with a thickness of 700 µm at a resolution of 100 nm normal to the surface of the substrate. Due to the writing speed of 10 lenses per hour this manufacturing process is ideally suited for rapid prototyping of systems comprising up to about 100 microlenses while parallelized writing techniques can be applied in order to force the pace of processing

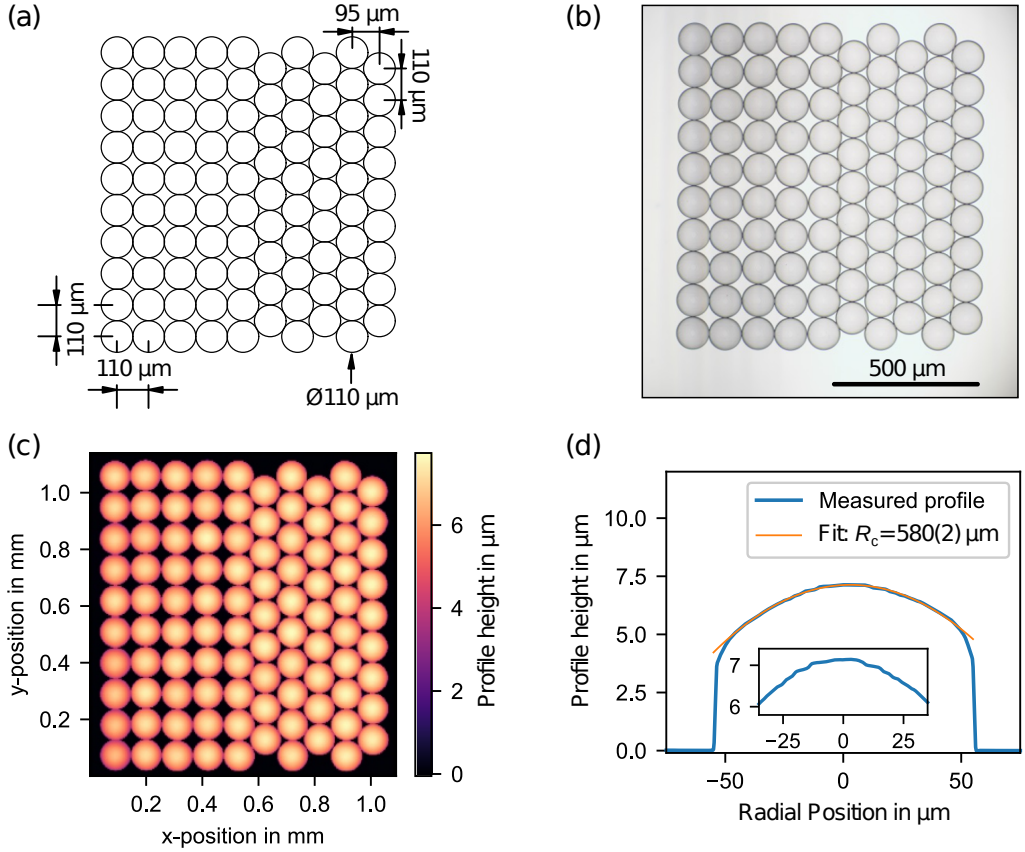

Figure 6.7.: Layout and characterization of the 3D-printed microlens array. (a) Based on a fundamental pitch of $d = 110$ µm the array consists of 97 spherical lenslets and is designed to feature a domain with quadratic and another one with hexagonal packing of the lenses as well as a transition area in between. (b) Inspection via white-light microscopy approves the successful manufacturing process and provides a detailed view on the element. (c) Using a confocal microscope allows for mapping the surface of the microlens array. (d) Profile of one of the microlenses and fit to determine the quality of the spherical surface and the radius of curvature R_c. The inset provides a more detailed view on the central region of the lenslet.

significantly [165].
As the height of each lenslet is typically in the regime of only a few micrometers, it is of vital importance to keep the surface roughness at a minimum. Consequently, the photoresist Nanoscribe IP-S which is optimized for the production of optical surfaces with smooth texture has been selected. In [166] an index of refraction $n = 1.505$ at a wavelength $\lambda = 796$ nm has been reported.

6.2.3. Verification of the manufacturing process

Before the microlens array is used for the generation of dipole traps, the results of fabrication are analyzed by optical means in order to verify a successful manufacturing process. Figure 6.7 (b) shows a white light image of the array taken with a standard optical microscope (Eclipse LV100, Nikon). The 97 lenslets are clearly visible and no defects are detected. Furthermore, a

commercial confocal microscope (µsurf expert, NanoFocus) is used to inspect the microlens array and retrieve a detailed three-dimensional profile of each lenslet (Fig. 6.7 (c)). From this, a cross section of a typical lens is depicted in Fig. 6.7 (d) from which a radius of curvature of $R_c = 580(2)$ µm of the spherical surface can be determined. Within 90 % of the diameter, an rms-deviation of 0.03 µm from a perfect sphere is calculated which yields an effective numerical aperture of $NA = 0.045(2)$. The inset in Fig. 6.7 (d) details the central region of the lens profile and the irregularities are in good agreement with the printing accuracy of the lithography system orthogonal to the substrate surface. Subsequently, the focal plane of the microlens array is examined via illumination of the lenses using a laser beam at a wavelength of $\lambda = 796.7$ nm with a diameter being much larger than the aperture of a microlens. Approximating a two-dimensional Gaussian beam at the foci yields $1/e^2$-waists of $w_q = 6.5(3)$ µm in the quadratic and $w_h = 6.4(3)$ µm in the region with hexagonal packing. This result is in excellent agreement with a wavefront simulation using Fresnel propagation as implemented in the package originally reported in [167] which returns a Gaussian waist of $w_{sim} = 6.3$ µm for a transmission through a lens having a radius of curvature R_c and a diameter of 110 µm.
For the ensuing use of the microlens generated foci for the purpose of trapping single atoms the waist has to be reduced significantly and reimaging optics similar to the implementation in the main experimental apparatus is required. Moreover, combination with DMD-based addressing is desirable for enhanced flexibility with respect to trap geometries and site-selective adjustability. This is demonstrated in the subsequent section.

6.2.4. Extended flexibility through combination of 3D printing and SLM

After the successful verification of the 3D-printed microlens array, the system is finally integrated in a setup featuring DMD-based addressability to reach full site-selective control in the manner detailed in Section 6.1.2. Figure 6.8 gives an overview of the essential constituents of this configuration. As illustrated in the simplified schematic in Fig. 6.8 (a) a laser beam with a wavelength of $\lambda = 796.7$ nm and a $1/e^2$-waist of $w = 1.2$ mm illuminates the DMD under an incident angle of $\alpha = 26°$ to reach the orthogonal reflection of the third diffraction order with respect to the DMD plane. Due to the smaller microlens diameter, the magnification of the mapping optics is adapted compared to the setup presented in the previous section in order to maintain a high number of mirrors per lenslet. Using a confocal telescope composed of two achromatic doublets L1 and L2 with focal lengths of $f_1 = 100$ mm and $f_2 = 45$ mm to map the DMD surface onto the microlens array, typically 730(8) mirrors within a circular region are associated with every lenslet (Fig. 6.8 (b)). This results in an effective aperture with a diameter of 109(1) µm illuminating the individual lenses while avoiding the irradiation of interstices. Thereby, stray light is impeded. Depending on the respective region within the array, 71 % (quadratic) and 82 % (hexagonal) of the mirrors contribute to the illumination of the microlenses, respectively. According to the specific geometry of the microlens array, arbitrary addressing patterns can be chosen as shown in Fig. 6.8 (c). In order to demagnify the focal plane of the microlens array, an achromatic doublet L3 with focal length $f_3 = 400$ mm and the microscope objective L4 with the effective focal length $f_4 = 37.5(10)$ mm ($NA = 0.25(2)$) are employed. Using the illumination configuration depicted in Fig. 6.8 (c) yields the intensity distribution after reimaging that is depicted in Fig. 6.8 (d). From approximation of two-dimensional Gaussian functions, a trap separation (pitch) of $p = 10.2(3)$ µm and waists of $w_q = 1.36(5)$ µm in the quadratic and $w_h = 1.29(6)$ µm in the hexagonal region are determined. Figure 6.9 demonstrates the capability of the fully featured setup. While in Fig. 6.9 (a) the completely enabled array comprising 97 tweezers is depicted a large number of spots have been

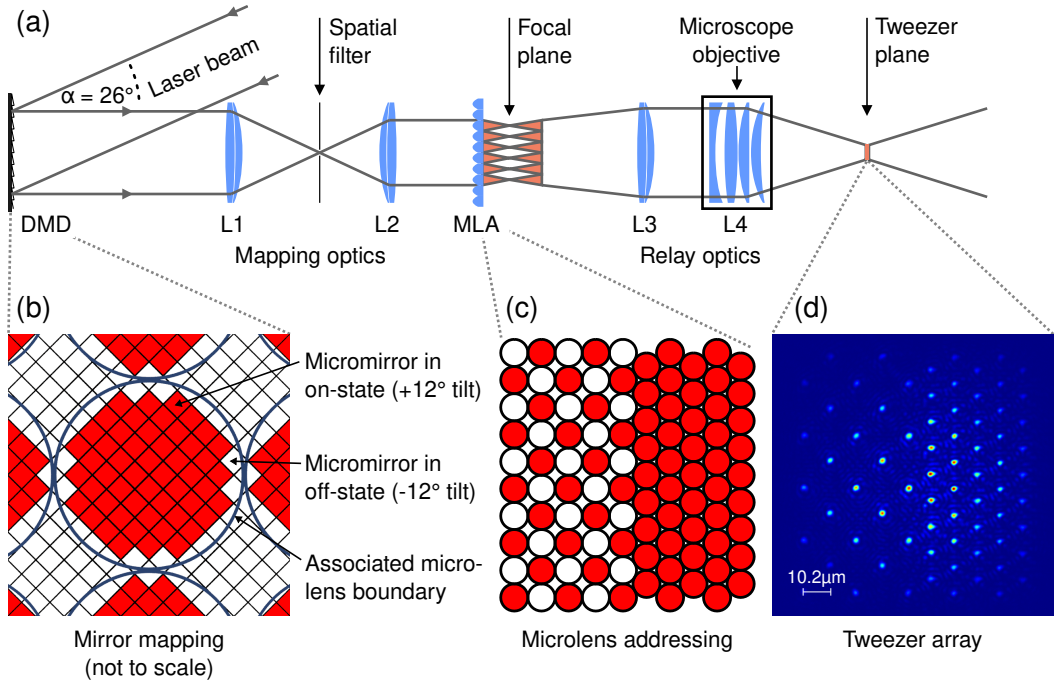

Figure 6.8.: (a) Simplified experimental setup for the DMD-based addressing of the 3D-printed microlens array. A Gaussian laser beam impinges on the DMD under an incident angle of $\alpha = 26°$ resulting in the third order of diffraction to be deflected orthogonally to the DMD surface. The micromirror plane is mapped onto the microlens array employing a confocal telescope. The resulting focal plane is reimaged and demagnified using an achromatic doublet in combination with a microscope objective. (b) This setup ensures that the illumination of each microlens is controlled by mirrors within a distinct circular region on the DMD and (c) allows for individual addressing of the lenses and exact control over (d) the resulting tweezer pattern.

deactivated in Fig. 6.9 (b). The cross sections in Fig. 6.9 (a, right) and Fig. 6.9 (b, right) along the marked paths indicated by the dashed lines in the images at left underpin the well-defined shape of the tweezers visible in the intensity distributions and the high contrast that is observed when deactivating individual tweezers. The Gaussian envelope is consistent with the shape of the beam which is incident on the DMD. However, if a uniform intensity distribution is desired [168, 169] either a beam with a flat top profile or site-selective optimization as demonstrated in Section 6.1.2 can be employed. The large number of 730(8) micromirrors associated with every lenslet allows for intensity adjustment on a 0.2 % scale in the range from 20 % to 100 % without impairing the quality of the tweezers in the same fashion as employed in Section 6.1.3.

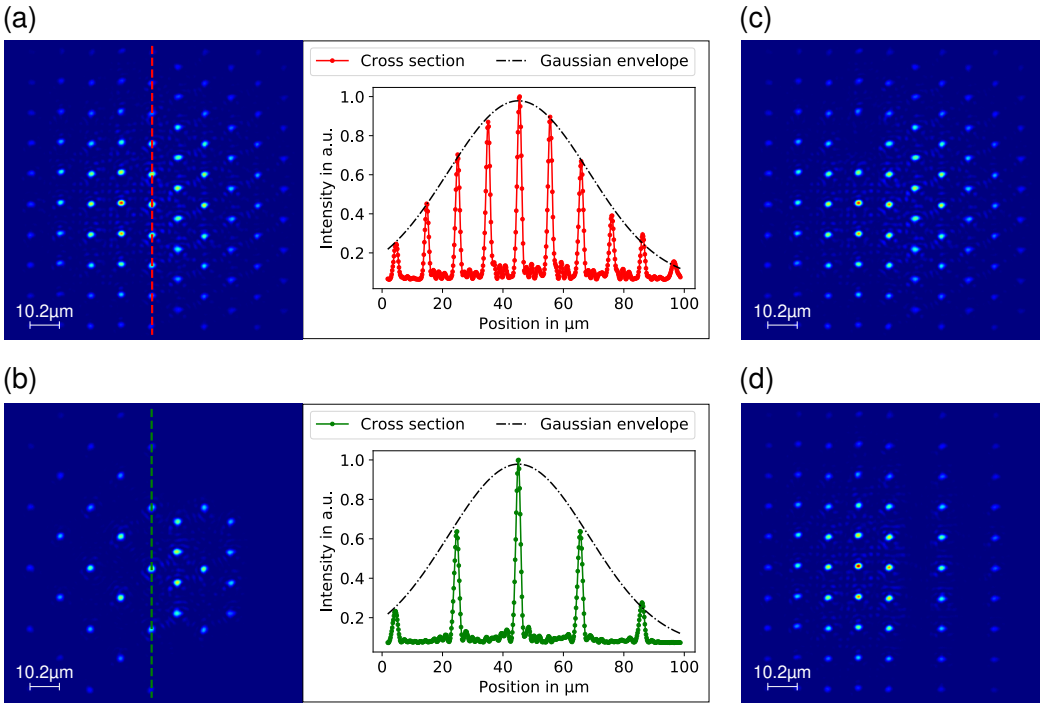

Figure 6.9.: Versatile tweezer geometries through combination of 3D printing and spatial light modulation. (a) Image of the fully activated tweezer array comprising 97 foci in a structure which reflects the fundamental geometry of the manufactured microlens system (left) and a cross section along the dashed line (right) showing the intensity distribution of the diffraction-limited tweezer spots. (b) Deactivation of certain subset foci allows for creation of new arrangements based on the underlying microlens pattern (left) and demonstrates the high contrast resulting from the DMD-based site-selective control (right). This approach provides in-situ flexibility to alter the tweezer geometry and enables the implementation of (c) single defects as well as (d) configurations with completely new symmetry.

6.3. Perspectives for further applications of DMD-based addressing techniques

As demonstrated in the previous sections, the technology of DMD-based spatial light modulation substantially enhances the flexibility in microlens-generated focused-beam tweezer platforms. It allows for exploration of new geometries via on-demand adaption of the tweezer pattern without necessity for modifications on the optical setup of the experimental apparatus when implemented in the beam path utilized for dipole trapping. Besides, there is a wide range of other potential applications where the present experimental platform, in specific, can benefit from this additional degree of adjustability.

Using a more or less identical optical setup, yet optimized for blue laser light, individual microlens addressing could be utilized to parallelize the site-selective Rydberg excitation employed in Chapter 4. Superimposing the tweezer arrays with the focused beams of such a counter-propagating DMD-controlled light field of the blue Rydberg laser excitations could be driven in parallel at various locations within the array with individually tunable interaction

strengths.
Moreover, using an additional tweezer array in combination with conical refraction can be used for the creation of two-dimensional bottle beam traps as detailed in [170]. This could be utilized for storage of Rydberg-excited atoms [130] exploiting the ponderomotive potential which leads to atom loss otherwise as discussed in Section 4.2.2. For future experiments, however, it will be essential to keep atoms spatially confined even after Rydberg excitation in order to increase the gate fidelity [86] or investigate coherent dynamics [47] beyond a time scale of about 10 µs after which we observe falling recapture probability [57] in the experimental setup.
On the way to a fully featured three-dimensional platform, DMD-based spatial light modulation will find immediate application in addressing of the present multi-layer geometry, yet in a modified implementation. Following the demonstration in [155], direct DMD surface mapping can be used to create high-contrast intensity distributions which could be utilized for flexible Talbot plane selection instead of the currently implemented static method discussed in Section 2.5. In the same way, layer-selective addressing and fluorescence imaging could be implemented on the basis of a spatially-modulated excitation light field from a lateral direction with respect to the optical axis of the dipole traps in combination with electrically tunable focusing optics as demonstrated in [34].

6.4. Conclusion

In this chapter, two state-of-the art technologies have been characterized with respect to their applicability in the experimental apparatus, adapted, and developed into a ready-to-use stage: DMD-based spatial light modulation and 3D printing of microlens arrays as well as the combination of both techniques. Extended with lens-selective illumination control by a DMD, the focused-beam tweezer array is equipped with parallelized site-specific addressability. This enables the modification of the tweezer geometry and individual trap depth adjustment on a kilohertz timescale. Relying on the straightforward relation of the light field amplitude passing each microlens and the corresponding tweezer focus this setup maintains the high degree of stability and precision of microlens-array-based platforms while being tunable due to the direct association between a microlens aperture and the respective group of DMD mirrors which control the illumination.
As the available range of tweezer geometries is eventually determined by the structure of the microlens array in use, this restricts the set of accessible patterns and can require its replacement which is easily achievable in the experimental setup. However, depending on the specific configuration the requested array may not be readily commercially available or require the development from the ground up which involves the manufacturing of a lithographic mask leading to expensive investments and long-lasting turn-around times. Using fabrication methods based on 3D direct laser writing as detailed in this chapter, these limitations have been overcome. Additionally, the combination of both technologies provides a yet unprecedented flexibility for the experimental setup making this approach ideally suited for realizing on-demand implementation of new configurations in the experimental platform.
Nevertheless, there are also several possibilities for optimization and extensions which can be addressed for even further enhancement. The measured DMD efficiency of $\eta = 33\,\%$ could be increased using a specially configured unit with anti-reflection coating of the DMD window for near-infrared light and optimized mirror pitch or tilt angle which better fulfills the blazed-grating condition. In [171] a value of 55 % has been reported for the DMD unit of a

disassembled commercial projector which, however, does not offer the necessary control over the mirror switching. In addition, the rate for pattern update of the present system could be potentially increased to several tens of kilohertz using a more advanced DMD system.
Regarding applications of the 3D-printing technology in the experimental setup, there is a vast range of possibilities offering new options which need to be further evaluated. While imprinting individual lenses with different focal lengths provides a straightforward way for implementation of versatile three-dimensional geometries with site-selective addressability, even more complicated optics such as multi-focal lenses seem accessible and deserve further analysis especially in combination with DMD-based spatial light modulation [172].
Integrated in the experimental apparatus, these technologies will allow to study Rydberg-interacting systems in versatile geometries with site-selective addressability. This includes the realization of exchange interactions [47] and the synthesis of spin Hamiltonians for simulation of quantum magnets and analysis of phase transitions [49, 90, 91] in an artificial and precisely controlled environment in which the influence of defects can be characterized as well as the response of the quantum system to domain boundaries.

7. Conclusion and Outlook

In this work, a scalable architecture exhibiting an extensive range of applications in the field of quantum technology has been presented. Based on the principle of focused-beam dipole traps, large-scale two-dimensional tweezer arrays are created using micro-fabricated optical elements. Comprising hundreds of diffraction limited foci, the introduced micro-optical platform is ideally suited to prepare extensive configurations of individual laser-cooled neutral atoms in an environment with accurate control over their internal and external degrees of freedom. The precisely defined spatial separation of the tweezers, on the one hand, allows to clearly resolve each site which is exploited during fluorescence imaging in order to determine the occupancy in the array. On the other hand, this is essential for site-resolved state detection, addressing of certain traps to drive coherent operations and vital when it comes to the implementation of interactions between specific atoms.
The capability of site-selective control has been directly utilized in a novel implementation of a movable optical tweezer system in the experimental apparatus that allows for rearrangement of arbitrary atom distributions in the array into predefined configurations. In this fashion, the initially random occupation of atoms which is a result of stochastic loading from the magneto-optical trap can be turned into defect-free clusters of up to 111 individual atoms via sequentially moving specific atoms between sites following the outcome of a real-time analysis using a heuristic algorithm. On the basis of multiple rearrangement cycles, the previously reported number of 72 atom-by-atom assembled configurations could be significantly exceeded [34] in the course of this work. The developed technique provides the necessary means to commence experiments from well-defined initial situations, furnishes a tool for compensation of atom losses during experimental cycles, and offers the possibility to reduce the required amount of time-consuming MOT-loading phases. The novel movable tweezer system found immediate application during the whole course of this thesis providing predefined initial situations as well as an enhanced filling fraction in a certain region of the tweezer array in order to accelerate characterization measurements. At the same time, it offers a new port for additional site-selective atom-light coupling via the steerable focus as shown in the context of Rydberg excitation in [57] and could also demonstrate its versatility in the example of site-selective fluorescence detection as detailed in this thesis.
An indispensable element for quantum computing is the ability for fast execution of one-qubit operations. During the course of this work, the coupling strength between the hyperfine ground states as demonstrated in [67] could be substantially increased achieving sub-microsecond π-pulse durations with Rabi frequencies above $2\pi \cdot 600\,\mathrm{kHz}$ in the central region of the array. Based on this, the presented platform was also employed for magnetic field sensing offering parallelized two-dimensional detection with a spatial resolution of 7 µm and sensitivity of 100 nT in a sensor plane comprising at total of 270 individual sensors in an area of 119 µm $\times$ 98 µm. This novel approach was utilized to characterize the magnetic gradient field used for magneto-optical trapping while the implementation of a single-atom probe within the movable optical tweezer demonstrated additional flexibility in defining a sensing location independent of the array grid with single-micrometer resolution.
Following the successful realization of Rydberg excitation based on a two-photon process

and Rydberg-mediated interactions in the present platform [56, 57], site-selective ground-to-Rydberg-state coupling was achieved during this work which is of immanent importance for the implementation of first quantum algorithms. Realizing an approach comparable to the movable tweezer setup, coherent excitations from the magnetically insensitive hyperfine ground state $|5S_{1/2}, F = 3, m_F = 0\rangle$ to the $82S_{1/2}$-state were accomplished with individual-site addressability and sub-microsecond π-pulse duration using a steerable focused laser beam. This was directly applied to demonstrate Rydberg blockade for pairs of atoms at neighboring sites in the tweezer array with an interatomic distance of 7 µm which constitutes an essential step towards the realization of two-qubit gate operations in the present setup. [41, 46].
Experiments in quantum computation and quantum simulation necessitate a reliable and stable platform yet providing a high degree of flexibility in specific situations for the implementation of algorithms and the adaption of the configuration to conduct simulations. The introduced micro-optical architecture offers a robust system due to the direct correspondence between the illumination of a lenslet and the respective tweezer focus. During this work, novel concepts for enhanced flexibility in defining tweezer configurations have been demonstrated relying on DMD-based spatial light modulation and microlens-array manufacturing through femtosecond direct laser writing. Due to the short production time, 3D printing allows for near-term change of the microlens array in use and thereby adapt a present tweezer geometry to the preconditions for an intended experiment. Using a DMD in order to control the light field amplitude passing the microlenses enables dynamical reconfiguration of the tweezer pattern at a kilohertz timescale with precise adjustment possibilities while maintaining the high quality of the microlens-based tweezer foci. In this work, a hybrid system has been presented combining both technologies which provides a new level of flexibility for the present quantum platform. Offering completely novel configurations which have not been accessible to this platform before, the system will find direct application in exploring Rydberg-mediated quantum interactions in domain boundaries or in the presence of defects after implementation into the experimental apparatus.
In each of the previous chapters, a specific challenge on the way towards a fully-featured quantum computation and simulation platform has been tackled. While this led to a significant leap forward in each of the addressed topics, it is natural that there are many perspectives for next steps in propelling the experimental architecture. Based on the available Rydberg-mediated interactions, the demonstration of entanglement can be regarded as a next milestone in the present platform. Starting with the demonstration of a CNOT gate [41], it will be possible to analyze techniques for distribution of entanglement within the array using the movable optical tweezer [121]. Additionally, implemented in the experimental setup, the newly achieved flexibility in trapping geometries will offer a testbed, for the investigation of spin-exchange interactions [47] with flexibly tunable configurations and environmental conditions. For both applications, boosting the two-photon Rabi frequency would be vital to mitigate atom loss in the context of Rydberg excitation. Implementation of an enhanced 480 nm laser system will provide enough laser power to reach megahertz coupling strength in a straightforward way. In this context, the realization of trapping techniques for Rydberg atoms [129, 130] provides an additional approach for optimization.
A next major challenge will be to scale up the system size to several thousands of atoms. This is essential to assemble a sufficiently high number of error-corrected logical qubits consisting of physical ones [103, 104]. Using the technique of interleaved arrays presented in [55, 173] will allow to overcome the present power limitations using several arrays driven by different laser sources and superimposed in a loss-free fashion. This can be complemented with an upgrade of the currently used microscope objective in order to achieve sub-micrometer tweezer

waists which will immediately increase the power efficiency. Combined with enhanced loading techniques [32] and parallelized rearrangement using multi-tone addressing via the movable tweezer [90] this will allow to massively expand the system size within a single tweezer plane already. Moreover, the intrinsically three-dimensional trapping geometry in the presented platform which results from the additional Talbot layers will offer an unprecedented range of further possibilities in future experiments.

A. Properties of ^{85}Rb

Detailed information regarding the properties of ^{85}Rb and the D_1 and D_2 transitions can be found in [83]. Some of the most important characteristics that are especially relevant in the context of this work are compiled in Table A.1. Additionally, in Fig. A.1 an energy level scheme of the D lines is depicted.

Atomic properties		
Atomic number	Z	37
Mass number	A	85
Atomic mass	m	$1.409\,993\,199(70) \times 10^{-25}$ kg
Nuclear spin	I	5/2
Nuclear *g*-factor	g_I	$-2.936\,400(6) \times 10^{-4}$

$5S_{1/2}$ ground state		
Fine structure *g*-factor	g_J	2.002 331 13(20)
Ground state splitting	Δ_hfs	$2\pi \cdot 3035.732\,439\,0(60)$ MHz

D1 transition $(5S_{1/2} \rightarrow 5P_{1/2})$		
Wavelength	λ	794.979 014 933(96) nm
Transition frequency	ω_0	2π·377.107 385 690(46) THz
Excited-state lifetime	τ	27.679(27) ns
Natural linewidth	Γ	2π·5.7500(56) MHz

D2 transition $(5S_{1/2} \rightarrow 5P_{3/2})$		
Wavelength	λ	780.241 368 271(27) nm
Transition frequency	ω_0	2π·384.230 406 373(14) THz
Excited-state lifetime	τ	26.2348(77) ns
Natural linewidth	Γ	2π·6.0666(18) MHz
Doppler temperature	T_D	145.57 µK
Recoil temperature	T_R	370.47 nK

Table A.1.: Physical properties of ^{85}Rb and the respective D_1 and D_2 transitions. The data is taken from [83].

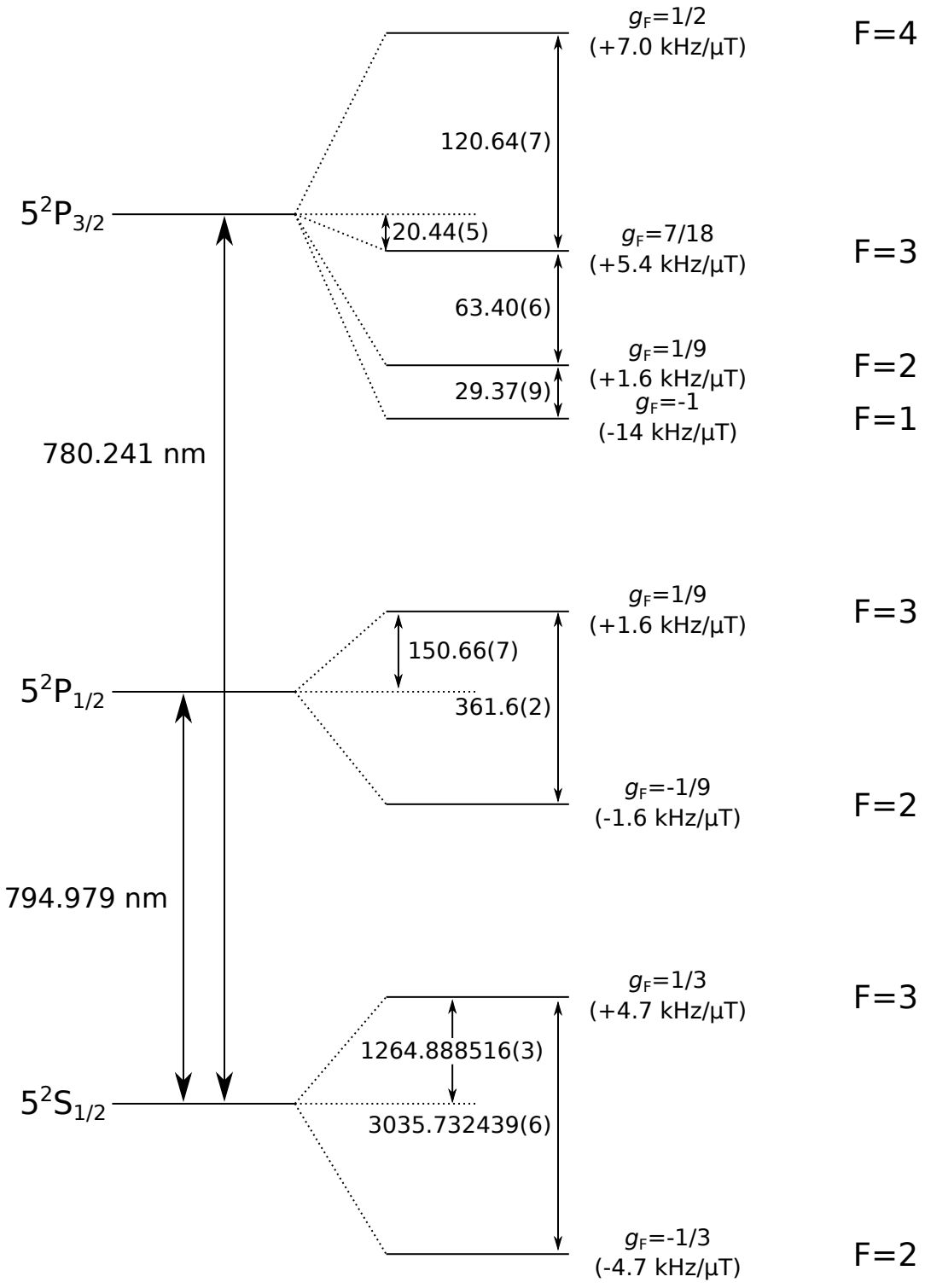

Figure A.1.: Energy level scheme of the ^{85}Rb hyperfine structure regarding the D_1 and D_2 transitions. The values for the splittings are given in megahertz. In addition to the hyperfine Landé g-factor g_F, the Zeeman shift of the m_F levels is provided. While the shifts within each hyperfine manifold are drawn to scale the spacings should not be compared between manifolds. The values are taken from [83].

B. Publications

The research presented in this thesis is shared with the scientific community in the following publications:

M. Schlosser, D. Ohl de Mello, D. Schäffner, T. Preuschoff, L. Kohfahl, and G. Birkl, "Assembled arrays of Rydberg-interacting atoms", Journal of Physics B: Atomic, Molecular and Optical Physics **53**, 144001 (2020)

D. Schäffner, T. Preuschoff, S. Ristok, L. Brozio, M. Schlosser, H. Giessen, and G. Birkl, "Arrays of individually controllable optical tweezers based on 3D-printed microlens arrays", Opt. Express **28**, 8640–8645 (2020)

M. Schlosser, S. Tichelmann, D. Schäffner, D. Ohl de Mello, M. Hambach, and G. Birkl, "Large-scale multilayer architecture of single-atom arrays with individual addressability", arXiv (2019)

D. Ohl de Mello*, D. Schäffner*, J. Werkmann, T. Preuschoff, L. Kohfahl, M. Schlosser, and G. Birkl, "Defect-Free Assembly of 2D Clusters of More Than 100 Single-Atom Quantum Systems", Phys. Rev. Lett. **122**, 203601 (2019)

* D. O. and D. S. contributed equally to this work.

D. Schäffner, "Atoms in optical lattices: Quantum simulation in a strictly aligned manner", Quantum Simulators **198**, 197 (2018)

C. Supervised Bachelor / Master theses

Bachelor theses

Pascal Boller
Generation of selectively addressable hexagonal Dipole Trap Arrays
Bachelor thesis, January 2018

Stefan Scheuren
Theoretical investigation of the interaction between Rydberg atoms
Bachelor thesis, July 2017

Master theses

Lukas Brozio
Micromirror-Based Manipulation of Dipole Traps Created by Microlens Arrays
Master thesis, March 2019

Lars Kohfahl
Two-Photon Rydberg Excitation of Neutral Atoms in Optical Dipole-Trap Arrays
Master thesis, April 2017

René Kolb
A control system for time critical experiments in Python
Master thesis, June 2017

Jan-Niklas Schmidt
Two-photon Rydberg excitation and analysis of an atom-loss detection scheme for atoms in dipole-trap arrays
Master thesis, August 2017

Jan Friedrich Werkmann
Control Systems and Optical Tweezers for Quantum Information Processing
Master thesis, May 2018

Max Werner
Coherent manipulation of cold atoms with phase-stabilized laser systems
Master thesis, November 2017

Bibliography

[1] W. Heisenberg, *Physics and beyond* (Allen & Unwin London, 1971).

[2] M. Planck, “Zur Theorie des Gesetzes der Energieverteilung im Normalspectrum”, in Verhandlungen der Deutschen Physikalischen Gesellschaft, Vol. 2 (1900), p. 237.

[3] S. Haroche, “Nobel Lecture: Controlling photons in a box and exploring the quantum to classical boundary”, Rev. Mod. Phys. **85**, 1083–1102 (2013).

[4] D. J. Wineland, “Nobel Lecture: Superposition, entanglement, and raising Schrödinger’s cat”, Rev. Mod. Phys. **85**, 1103–1114 (2013).

[5] H. D. Zeh, “On the interpretation of measurement in quantum theory”, Foundations of Physics **1**, 69–76 (1970).

[6] S. Chu, “Nobel Lecture: The manipulation of neutral particles”, Rev. Mod. Phys. **70**, 685–706 (1998).

[7] C. N. Cohen-Tannoudji, “Nobel Lecture: Manipulating atoms with photons”, Rev. Mod. Phys. **70**, 707–719 (1998).

[8] W. D. Phillips, “Nobel Lecture: Laser cooling and trapping of neutral atoms”, Rev. Mod. Phys. **70**, 721–741 (1998).

[9] E. A. Cornell and C. E. Wieman, “Nobel Lecture: Bose-Einstein condensation in a dilute gas, the first 70 years and some recent experiments”, Rev. Mod. Phys. **74**, 875–893 (2002).

[10] W. Ketterle, “Nobel lecture: When atoms behave as waves: Bose-Einstein condensation and the atom laser”, Rev. Mod. Phys. **74**, 1131–1151 (2002).

[11] M. Greiner, O. Mandel, T. Esslinger, T. W. Hänsch, and I. Bloch, “Quantum phase transition from a superfluid to a Mott insulator in a gas of ultracold atoms”, Nature **415**, 39–44 (2002).

[12] R. P. Feynman, “Simulating physics with computers”, International Journal of Theoretical Physics **21**, 467–488 (1982).

[13] D. Deutsch and R. Penrose, “Quantum theory, the Church-Turing principle and the universal quantum computer”, Proceedings of the Royal Society of London. A. Mathematical and Physical Sciences **400**, 97–117 (1985).

[14] L. K. Grover, “Quantum Mechanics Helps in Searching for a Needle in a Haystack”, Phys. Rev. Lett. **79**, 325–328 (1997).

[15] P. W. Shor, “Polynomial-Time Algorithms for Prime Factorization and Discrete Logarithms on a Quantum Computer”, SIAM Journal on Computing **26**, 1484–1509 (1997).

[16] S. Lloyd, “Universal Quantum Simulators”, Science **273**, 1073–1078 (1996).

[17] I. L. Chuang, L. M. K. Vandersypen, X. Zhou, D. W. Leung, and S. Lloyd, “Experimental realization of a quantum algorithm”, Nature **393**, 143–146 (1998).

[18] L. M. K. Vandersypen, M. Steffen, G. Breyta, C. S. Yannoni, M. H. Sherwood, and I. L. Chuang, “Experimental realization of Shor’s quantum factoring algorithm using nuclear magnetic resonance”, Nature **414**, 883–887 (2001).

[19] R. Blatt and C. F. Roos, “Quantum simulations with trapped ions”, Nature Physics **8**, 277–284 (2012).

[20] M. Gärttner, J. G. Bohnet, A. Safavi-Naini, M. L. Wall, J. J. Bollinger, and A. M. Rey, “Measuring out-of-time-order correlations and multiple quantum spectra in a trapped-ion quantum magnet”, Nature Physics **13**, 781–786 (2017).

[21] M. Kjaergaard, M. E. Schwartz, J. Braumüller, P. Krantz, J. I.-J. Wang, S. Gustavsson, and W. D. Oliver, “Superconducting Qubits: Current State of Play”, Annual Review of Condensed Matter Physics **11**, 369–395 (2020).

[22] A. D. King, J. Carrasquilla, J. Raymond, I. Ozfidan, E. Andriyash, A. Berkley, M. Reis, T. Lanting, R. Harris, F. Altomare, K. Boothby, P. I. Bunyk, C. Enderud, A. Fréchette, E. Hoskinson, N. Ladizinsky, T. Oh, G. Poulin-Lamarre, C. Rich, Y. Sato, A. Y. Smirnov, L. J. Swenson, M. H. Volkmann, J. Whittaker, J. Yao, E. Ladizinsky, M. W. Johnson, J. Hilton, and M. H. Amin, “Observation of topological phenomena in a programmable lattice of 1,800 qubits”, Nature **560**, 456–460 (2018).

[23] F. Arute, K. Arya, R. Babbush, D. Bacon, J. C. Bardin, R. Barends, R. Biswas, S. Boixo, F. G. S. L. Brandao, D. A. Buell, B. Burkett, Y. Chen, Z. Chen, B. Chiaro, R. Collins, W. Courtney, A. Dunsworth, E. Farhi, B. Foxen, A. Fowler, C. Gidney, M. Giustina, R. Graff, K. Guerin, S. Habegger, M. P. Harrigan, M. J. Hartmann, A. Ho, M. Hoffmann, T. Huang, T. S. Humble, S. V. Isakov, E. Jeffrey, Z. Jiang, D. Kafri, K. Kechedzhi, J. Kelly, P. V. Klimov, S. Knysh, A. Korotkov, F. Kostritsa, D. Landhuis, M. Lindmark, E. Lucero, D. Lyakh, S. Mandrà, J. R. McClean, M. McEwen, A. Megrant, X. Mi, K. Michielsen, M. Mohseni, J. Mutus, O. Naaman, M. Neeley, C. Neill, M. Y. Niu, E. Ostby, A. Petukhov, J. C. Platt, C. Quintana, E. G. Rieffel, P. Roushan, N. C. Rubin, D. Sank, K. J. Satzinger, V. Smelyanskiy, K. J. Sung, M. D. Trevithick, A. Vainsencher, B. Villalonga, T. White, Z. J. Yao, P. Yeh, A. Zalcman, H. Neven, and J. M. Martinis, “Quantum supremacy using a programmable superconducting processor”, Nature **574**, 505–510 (2019).

[24] I. Bloch, J. Dalibard, and S. Nascimbène, “Quantum simulations with ultracold quantum gases”, Nature Physics **8**, 267–276 (2012).

[25] T. Byrnes, K. Wen, and Y. Yamamoto, “Macroscopic quantum computation using Bose-Einstein condensates”, Phys. Rev. A **85**, 040306 (2012).

[26] D. P. DiVincenzo, “The Physical Implementation of Quantum Computation”, Fortschritte der Physik **48**, 771–783 (2000).

[27] P. W. Shor, “Scheme for reducing decoherence in quantum computer memory”, Phys. Rev. A **52**, R2493–R2496 (1995).

[28] M. Endres, H. Bernien, A. Keesling, H. Levine, E. R. Anschuetz, A. Krajenbrink, C. Senko, V. Vuletić, M. Greiner, and M. D. Lukin, “Atom-by-atom assembly of defect-free one-dimensional cold atom arrays”, Science **354**, 1024–1027 (2016).

[29] D. Barredo, S. de Léséleuc, V. Lienhard, T. Lahaye, and A. Browaeys, “An atom-by-atom assembler of defect-free arbitrary two-dimensional atomic arrays”, Science **354**, 1021–1023 (2016).

[30] C. Gross and I. Bloch, “Quantum simulations with ultracold atoms in optical lattices”, Science **357**, 995–1001 (2017).

[31] D. Ohl de Mello, D. Schäffner, J. Werkmann, T. Preuschoff, L. Kohfahl, M. Schlosser, and G. Birkl, “Defect-Free Assembly of 2D Clusters of More Than 100 Single-Atom Quantum Systems”, Phys. Rev. Lett. **122**, 203601 (2019).

[32] M. O. Brown, T. Thiele, C. Kiehl, T.-W. Hsu, and C. A. Regal, “Gray-Molasses Optical-Tweezer Loading: Controlling Collisions for Scaling Atom-Array Assembly”, Phys. Rev. X **9**, 011057 (2019).

[33] Y. Wang, X. Zhang, T. A. Corcovilos, A. Kumar, and D. S. Weiss, “Coherent Addressing of Individual Neutral Atoms in a 3D Optical Lattice”, Phys. Rev. Lett. **115**, 043003 (2015).

[34] D. Barredo, V. Lienhard, S. de Léséleuc, T. Lahaye, and A. Browaeys, “Synthetic three-dimensional atomic structures assembled atom by atom”, Nature **561**, 79–82 (2018).

[35] A. Kumar, T.-Y. Wu, F. Giraldo, and D. S. Weiss, “Sorting ultracold atoms in a three-dimensional optical lattice in a realization of Maxwell’s demon”, Nature **561**, 83–87 (2018).

[36] M. Anderlini, P. J. Lee, B. L. Brown, J. Sebby-Strabley, W. D. Phillips, and J. V. Porto, “Controlled exchange interaction between pairs of neutral atoms in an optical lattice”, Nature **448**, 452–456 (2007).

[37] D. Barredo, S. Ravets, H. Labuhn, L. Béguin, A. Vernier, F. Nogrette, T. Lahaye, and A. Browaeys, “Demonstration of a Strong Rydberg Blockade in Three-Atom Systems with Anisotropic Interactions”, Phys. Rev. Lett. **112**, 183002 (2014).

[38] T. Wilk, A. Gaëtan, C. Evellin, J. Wolters, Y. Miroshnychenko, P. Grangier, and A. Browaeys, “Entanglement of Two Individual Neutral Atoms Using Rydberg Blockade”, Phys. Rev. Lett. **104**, 010502 (2010).

[39] A. Omran, H. Levine, A. Keesling, G. Semeghini, T. T. Wang, S. Ebadi, H. Bernien, A. S. Zibrov, H. Pichler, S. Choi, J. Cui, M. Rossignolo, P. Rembold, S. Montangero, T. Calarco, M. Endres, M. Greiner, V. Vuletić, and M. D. Lukin, “Generation and manipulation of Schrödinger cat states in Rydberg atom arrays”, Science **365**, 570–574 (2019).

[40] H. Jo, Y. Song, M. Kim, and J. Ahn, “Rydberg Atom Entanglements in the Weak Coupling Regime”, Phys. Rev. Lett. **124**, 033603 (2020).

[41] L. Isenhower, E. Urban, X. L. Zhang, A. T. Gill, T. Henage, T. A. Johnson, T. G. Walker, and M. Saffman, “Demonstration of a Neutral Atom Controlled-NOT Quantum Gate”, Phys. Rev. Lett. **104**, 010503 (2010).

[42] H. Levine, A. Keesling, G. Semeghini, A. Omran, T. T. Wang, S. Ebadi, H. Bernien, M. Greiner, V. Vuletić, H. Pichler, and M. D. Lukin, “Parallel Implementation of High-Fidelity Multiqubit Gates with Neutral Atoms”, Phys. Rev. Lett. **123**, 170503 (2019).

[43] A. Facon, E.-K. Dietsche, D. Grosso, S. Haroche, J.-M. Raimond, M. Brune, and S. Gleyzes, “A sensitive electrometer based on a Rydberg atom in a Schrödinger-cat state”, Nature **535**, 262–265 (2016).

[44] A. Paris-Mandoki, C. Braun, J. Kumlin, C. Tresp, I. Mirgorodskiy, F. Christaller, H. P. Büchler, and S. Hofferberth, “Free-Space Quantum Electrodynamics with a Single Rydberg Superatom”, Phys. Rev. X **7**, 041010 (2017).

[45] C. S. Adams, J. D. Pritchard, and J. P. Shaffer, "Rydberg atom quantum technologies", Journal of Physics B: Atomic, Molecular and Optical Physics **53**, 012002 (2019).

[46] M. Saffman, T. G. Walker, and K. Mølmer, "Quantum information with Rydberg atoms", Rev. Mod. Phys. **82**, 2313–2363 (2010).

[47] D. Barredo, H. Labuhn, S. Ravets, T. Lahaye, A. Browaeys, and C. S. Adams, "Coherent Excitation Transfer in a Spin Chain of Three Rydberg Atoms", Phys. Rev. Lett. **114**, 113002 (2015).

[48] H. Labuhn, D. Barredo, S. Ravets, S. de Léséleuc, T. Macrì, T. Lahaye, and A. Browaeys, "Tunable two-dimensional arrays of single Rydberg atoms for realizing quantum Ising models", Nature **534**, 667–670 (2016).

[49] V. Lienhard, S. de Léséleuc, D. Barredo, T. Lahaye, A. Browaeys, M. Schuler, L.-P. Henry, and A. M. Läuchli, "Observing the Space- and Time-Dependent Growth of Correlations in Dynamically Tuned Synthetic Ising Models with Antiferromagnetic Interactions", Phys. Rev. X **8**, 021070 (2018).

[50] P. Schauss, "Quantum simulation of transverse Ising models with Rydberg atoms", Quantum Science and Technology **3**, 023001 (2018).

[51] A. Keesling, A. Omran, H. Levine, H. Bernien, H. Pichler, S. Choi, R. Samajdar, S. Schwartz, P. Silvi, S. Sachdev, P. Zoller, M. Endres, M. Greiner, V. Vuletić, and M. D. Lukin, "Quantum Kibble-Zurek mechanism and critical dynamics on a programmable Rydberg simulator", Nature **568**, 207–211 (2019).

[52] A. Kitaev, "Fault-tolerant quantum computation by anyons", Annals of Physics **303**, 2–30 (2003).

[53] A. Ashkin, J. M. Dziedzic, J. E. Bjorkholm, and S. Chu, "Observation of a single-beam gradient force optical trap for dielectric particles", Opt. Lett. **11**, 288–290 (1986).

[54] J. Kruse, C. Gierl, M. Schlosser, and G. Birkl, "Reconfigurable site-selective manipulation of atomic quantum systems in two-dimensional arrays of dipole traps", Phys. Rev. A **81**, 060308 (2010).

[55] A. Lengwenus, J. Kruse, M. Schlosser, S. Tichelmann, and G. Birkl, "Coherent Transport of Atomic Quantum States in a Scalable Shift Register", Phys. Rev. Lett. **105**, 170502 (2010).

[56] M. Schlosser, D. Ohl de Mello, D. Schäffner, T. Preuschoff, L. Kohfahl, and G. Birkl, "Assembled arrays of Rydberg-interacting atoms", Journal of Physics B: Atomic, Molecular and Optical Physics **53**, 144001 (2020).

[57] D. Ohl de Mello, "Rydberg interactions in a defect-free array of single-atom quantum systems", PhD thesis (TU Darmstadt, 2020).

[58] A. Ashkin, "Acceleration and Trapping of Particles by Radiation Pressure", Phys. Rev. Lett. **24**, 156–159 (1970).

[59] A. Ashkin, *Optical trapping and manipulation of neutral particles using lasers* (WORLD SCIENTIFIC, 2006).

[60] A. Ashkin, "Applications of Laser Radiation Pressure", Science **210**, 1081–1088 (1980).

[61] P. Polimeno, A. Magazzù, M. A. Iatì, F. Patti, R. Saija, C. D. Esposti Boschi, M. G. Donato, P. G. Gucciardi, P. H. Jones, G. Volpe, and O. M. Maragò, "Optical tweezers and their applications", Journal of Quantitative Spectroscopy and Radiative Transfer **218**, 131–150 (2018).

[62] K. R. Dhakal and V. Lakshminarayanan, "Optical Tweezers: Fundamentals and Some Biophysical Applications", Progress in Optics **63**, 1–31 (2018).

[63] H. J. Metcalf and P. van der Straten, *Laser Cooling and Trapping* (Springer, 1999).

[64] D. A. Steck, *Quantum and Atom Optics*, (2019) `http://steck.us/teaching`.

[65] V. Weisskopf and E. Wigner, "Berechnung der natürlichen Linienbreite auf Grund der Diracschen Lichttheorie", Zeitschrift für Physik **63**, 54–73 (1930).

[66] R. Grimm, M. Weidemüller, and Y. B. Ovchinnikov, "Optical dipole traps for neutral atoms", Advances In Atomic, Molecular, and Optical Physics **42**, 95–170 (2000).

[67] M. Schlosser, "Preparation and coherent control of single-atom quantum systems in two-dimensional quantum processing architectures", PhD thesis (TU Darmstadt, 2013).

[68] M. Schlosser, S. Tichelmann, D. Schäffner, D. Ohl de Mello, M. Hambach, and G. Birkl, "Large-scale multilayer architecture of single-atom arrays with individual addressability", arXiv (2019).

[69] B. Besold and N. Lindlein, "Fractional Talbot effect for periodic microlens arrays", Optical Engineering **36**, 1099–1105 (1997).

[70] T. Preuschoff, M. Schlosser, and G. Birkl, "Digital laser frequency and intensity stabilization based on the STEMlab platform (originally Red Pitaya)", Review of Scientific Instruments **91**, 083001 (2020).

[71] T. Preuschoff, "Optimization of a Master Spectroscopy Laser System via MTS Stabilization", Master thesis (TU Darmstadt, 2016).

[72] T. Preuschoff, M. Schlosser, and G. Birkl, "Optimization strategies for modulation transfer spectroscopy applied to laser stabilization", Opt. Express **26**, 24010–24019 (2018).

[73] F. Christ, "Laser frequency stabilization via MTS on the D_1 transition of rubidium", Bachelor thesis (TU Darmstadt, 2020).

[74] J. Kruse, "Neutral Atoms in a Dipole Trap Array for Quantum Information Processing", PhD thesis (TU Darmstadt, 2010).

[75] J. Sattler, "Planung und Aufbau eines Experiments zur Manipulation einzelner neutraler Atome", Master thesis (TU Darmstadt, 2008).

[76] M. Werner, "Coherent manipulation of cold atoms with phase-stabilized lasersystems", Master thesis (TU Darmstadt, 2017).

[77] P. D. Lett, R. N. Watts, C. I. Westbrook, W. D. Phillips, P. L. Gould, and H. J. Metcalf, "Observation of Atoms Laser Cooled below the Doppler Limit", Phys. Rev. Lett. **61**, 169–172 (1988).

[78] A. Aspect, E. Arimondo, R. Kaiser, N. Vansteenkiste, and C. Cohen-Tannoudji, "Laser Cooling below the One-Photon Recoil Energy by Velocity-Selective Coherent Population Trapping", Phys. Rev. Lett. **61**, 826–829 (1988).

[79] N. Schlosser, G. Reymond, I. Protsenko, and P. Grangier, "Sub-poissonian loading of single atoms in a microscopic dipole trap", Nature **411**, 1024–1027 (2001).

[80] N. Schlosser, G. Reymond, and P. Grangier, "Collisional Blockade in Microscopic Optical Dipole Traps", Phys. Rev. Lett. **89**, 023005 (2002).

[81] B. Ueberholz, S. Kuhr, D. Frese, D. Meschede, and V. Gomer, "Counting cold collisions", Journal of Physics B: Atomic, Molecular and Optical Physics **33**, L135–L142 (2000).

[82] S. J. M. Kuppens, K. L. Corwin, K. W. Miller, T. E. Chupp, and C. E. Wieman, "Loading an optical dipole trap", Phys. Rev. A **62**, 013406 (2000).

[83] D. A. Steck, *Rubidium 85 D Line Data*, version 2.2.2, `http://steck.us/alkalidata`.

[84] A. Corney, "The hyperfine structure of atoms and its investigation by magnetic resonance methods", in *Atomic and laser spectroscopy* (Oxford University Press, 2006).

[85] G. Breit and I. I. Rabi, "Measurement of Nuclear Spin", Phys. Rev. **38**, 2082–2083 (1931).

[86] M. Saffman, "Quantum computing with atomic qubits and Rydberg interactions: progress and challenges", Journal of Physics B: Atomic, Molecular and Optical Physics **49**, 202001 (2016).

[87] A. Browaeys, D. Barredo, and T. Lahaye, "Experimental investigations of dipole–dipole interactions between a few Rydberg atoms", Journal of Physics B: Atomic, Molecular and Optical Physics **49**, 152001 (2016).

[88] A. Browaeys and T. Lahaye, "Many-body physics with individually controlled Rydberg atoms", Nature Physics **16**, 132–142 (2020).

[89] J. Zeiher, P. Schauß, S. Hild, T. Macrì, I. Bloch, and C. Gross, "Microscopic Characterization of Scalable Coherent Rydberg Superatoms", Phys. Rev. X **5**, 031015 (2015).

[90] H. Bernien, S. Schwartz, A. Keesling, H. Levine, A. Omran, H. Pichler, S. Choi, A. S. Zibrov, M. Endres, M. Greiner, V. Vuletić, and M. D. Lukin, "Probing many-body dynamics on a 51-atom quantum simulator", Nature **551**, 579–584 (2017).

[91] S. de Léséleuc, S. Weber, V. Lienhard, D. Barredo, H. P. Büchler, T. Lahaye, and A. Browaeys, "Accurate Mapping of Multilevel Rydberg Atoms on Interacting Spin-$1/2$ Particles for the Quantum Simulation of Ising Models", Phys. Rev. Lett. **120**, 113602 (2018).

[92] D. Tiarks, S. Schmidt-Eberle, T. Stolz, G. Rempe, and S. Dürr, "A photon-photon quantum gate based on Rydberg interactions", Nature Physics **15**, 124–126 (2019).

[93] S. Ravets, H. Labuhn, D. Barredo, L. Béguin, T. Lahaye, and A. Browaeys, "Coherent dipole-dipole coupling between two single Rydberg atoms at an electrically-tuned Förster resonance", Nature Physics **10**, 914–917 (2014).

[94] J. A. Sedlacek, A. Schwettmann, H. Kübler, R. Löw, T. Pfau, and J. P. Shaffer, "Microwave electrometry with Rydberg atoms in a vapour cell using bright atomic resonances", Nature Physics **8**, 819–824 (2012).

[95] C. G. Wade, N. Šibalić, N. R. de Melo, J. M. Kondo, C. S. Adams, and K. J. Weatherill, "Real-time near-field terahertz imaging with atomic optical fluorescence", Nature Photonics **11**, 40–43 (2017).

[96] T. F. Gallagher, *Rydberg Atoms*, Cambridge Monographs on Atomic, Molecular and Chemical Physics (Cambridge University Press, 1994).

[97] S. Weber, C. Tresp, H. Menke, A. Urvoy, O. Firstenberg, H. P. Büchler, and S. Hofferberth, "Tutorial: Calculation of Rydberg interaction potentials", J. Phys. B: At. Mol. Opt. Phys. **50**, 133001 (2017).

[98] X. Wu, X. Liang, Y. Tian, F. Yang, C. Chen, Y.-C. Liu, M. K. Tey, and L. You, "A concise review of Rydberg atom based quantum computation and quantum simulation", Chinese Physics B **30**, 020305 (2021).

[99] N. Šibalić, J. Pritchard, C. Adams, and K. Weatherill, "ARC: An open-source library for calculating properties of alkali Rydberg atoms", Computer Physics Communications **220**, 319–331 (2017).

[100] I. I. Beterov, I. I. Ryabtsev, D. B. Tretyakov, and V. M. Entin, "Quasiclassical calculations of blackbody-radiation-induced depopulation rates and effective lifetimes of Rydberg nS, nP, and nD alkali-metal atoms with $n \leq 80$", Phys. Rev. A **79**, 052504 (2009).

[101] P. Pillet, T. Vogt, M. Viteau, A. Chotia, J. Zhao, D. Comparat, T. F. Gallagher, D. Tate, A. Gaëtan, Y. Miroshnychenko, T. Wilk, A. Browaeys, and P. Grangier, "Controllable interactions between Rydberg atoms and ultracold plasmas", Journal of Physics: Conference Series **194**, 012066 (2009).

[102] E. Robertson, N. Šibalić, R. Potvliege, and M. Jones, "ARC 3.0: An expanded Python toolbox for atomic physics calculations", Computer Physics Communications **261**, 107814 (2021).

[103] A. G. Fowler, M. Mariantoni, J. M. Martinis, and A. N. Cleland, "Surface codes: Towards practical large-scale quantum computation", Phys. Rev. A **86**, 032324 (2012).

[104] H. Bombin and M. A. Martin-Delgado, "Statistical mechanical models and topological color codes", Phys. Rev. A **77**, 042322 (2008).

[105] W. S. Bakr, A. Peng, M. E. Tai, R. Ma, J. Simon, J. I. Gillen, S. Fölling, L. Pollet, and M. Greiner, "Probing the Superfluid–to–Mott Insulator Transition at the Single-Atom Level", Science **329**, 547–550 (2010).

[106] J. F. Sherson, C. Weitenberg, M. Endres, M. Cheneau, I. Bloch, and S. Kuhr, "Single-atom-resolved fluorescence imaging of an atomic Mott insulator", Nature **467**, 68–72 (2010).

[107] A. Mazurenko, C. S. Chiu, G. Ji, M. F. Parsons, M. Kanász-Nagy, R. Schmidt, F. Grusdt, E. Demler, D. Greif, and M. Greiner, "A cold-atom Fermi-Hubbard antiferromagnet", Nature **545**, 462 (2017).

[108] C. S. Chiu, G. Ji, A. Mazurenko, D. Greif, and M. Greiner, "Quantum State Engineering of a Hubbard System with Ultracold Fermions", Phys. Rev. Lett. **120**, 243201 (2018).

[109] E. Guardado-Sanchez, P. T. Brown, D. Mitra, T. Devakul, D. A. Huse, P. Schauß, and W. S. Bakr, "Probing the Quench Dynamics of Antiferromagnetic Correlations in a 2D Quantum Ising Spin System", Phys. Rev. X **8**, 021069 (2018).

[110] Y. Miroshnychenko, W. Alt, I. Dotsenko, L. Förster, M. Khudaverdyan, D. Meschede, D. Schrader, and A. Rauschenbeutel, "An atom-sorting machine", Nature **442**, 151–151 (2006).

[111] K. D. Nelson, X. Li, and D. S. Weiss, "Imaging single atoms in a three-dimensional array", Nat. Phys. **3**, 556–560 (2007).

[112] A. Gaëtan, Y. Miroshnychenko, T. Wilk, A. Chotia, M. Viteau, D. Comparat, P. Pillet, A. Browaeys, and P. Grangier, "Observation of collective excitation of two individual atoms in the Rydberg blockade regime", Nat. Phys. **5**, 115–118 (2009).

[113] T. Grünzweig, A. Hilliard, M. McGovern, and M. F. Andersen, "Near-deterministic preparation of a single atom in an optical microtrap", Nature Physics **6**, 951–954 (2010).

[114] B. J. Lester, N. Luick, A. M. Kaufman, C. M. Reynolds, and C. A. Regal, "Rapid Production of Uniformly Filled Arrays of Neutral Atoms", Phys. Rev. Lett. **115**, 073003 (2015).

[115] H. Kim, W. Lee, H.-g. Lee, H. Jo, Y. Song, and J. Ahn, "In situ single-atom array synthesis using dynamic holographic optical tweezers", Nature communications **7**, 13317 (2016).

[116] J. Werkmann, "Control Systems and Optical Tweezers for Quantum Information Processing", Master thesis (TU Darmstadt, 2018).

[117] T. Grünzweig, M. McGovern, A. J. Hilliard, and M. F. Andersen, "Using light-assisted collisions to consistently isolate individual atoms for quantum information processing", Quantum Information Processing **10**, 925–940 (2011).

[118] M. Schlosser, J. Kruse, C. Gierl, S. Teichmann, S. Tichelmann, and G. Birkl, "Fast transport, atom sample splitting and single-atom qubit supply in two-dimensional arrays of optical microtraps", New Journal of Physics **14**, 123034 (2012).

[119] D. Hucul, M. Yeo, W. K. Hensinger, J. Rabchuk, S. Olmschenk, and C. Monroe, "On the transport of atomic ions in linear and multidimensional ion trap arrays", Quantum Information and Computation **8**, 501–578 (2008).

[120] M. Hambach, "Towards the implementation of quantum gates in optical dipole trap arrays", Master thesis (TU Darmstadt, 2012).

[121] A. M. Kaufman, B. J. Lester, M. Foss-Feig, M. L. Wall, A. M. Rey, and C. A. Regal, "Entangling two transportable neutral atoms via local spin exchange", Nature **527**, 208–211 (2015).

[122] D. Ohl de Mello, "Experimental demonstration of 100+ qubit registers and fast atom transport", Master thesis (TU Darmstadt, 2014).

[123] A. Fuhrmanek, R. Bourgain, Y. R. P. Sortais, and A. Browaeys, "Free-Space Lossless State Detection of a Single Trapped Atom", Phys. Rev. Lett. **106**, 133003 (2011).

[124] M. J. Gibbons, C. D. Hamley, C.-Y. Shih, and M. S. Chapman, "Nondestructive Fluorescent State Detection of Single Neutral Atom Qubits", Phys. Rev. Lett. **106**, 133002 (2011).

[125] H. Labuhn, S. Ravets, D. Barredo, L. Béguin, F. Nogrette, T. Lahaye, and A. Browaeys, "Single-atom addressing in microtraps for quantum-state engineering using Rydberg atoms", Phys. Rev. A **90**, 023415 (2014).

[126] H. Levine, A. Keesling, A. Omran, H. Bernien, S. Schwartz, A. S. Zibrov, M. Endres, M. Greiner, V. Vuletić, and M. D. Lukin, "High-Fidelity Control and Entanglement of Rydberg-Atom Qubits", Phys. Rev. Lett. **121**, 123603 (2018).

[127] A. M. Hankin, Y.-Y. Jau, L. P. Parazzoli, C. W. Chou, D. J. Armstrong, A. J. Landahl, and G. W. Biedermann, "Two-atom Rydberg blockade using direct $6S$ to nP excitation", Phys. Rev. A **89**, 033416 (2014).

[128] J. Zeiher, R. van Bijnen, P. Schauß, S. Hild, J.-y. Choi, T. Pohl, I. Bloch, and C. Gross, "Many-body interferometry of a Rydberg-dressed spin lattice", Nature Physics **12**, 1095–1099 (2016).

[129] S. E. Anderson, K. C. Younge, and G. Raithel, "Trapping Rydberg Atoms in an Optical Lattice", Phys. Rev. Lett. **107**, 263001 (2011).

[130] D. Barredo, V. Lienhard, P. Scholl, S. de Léséleuc, T. Boulier, A. Browaeys, and T. Lahaye, "Three-Dimensional Trapping of Individual Rydberg Atoms in Ponderomotive Bottle Beam Traps", Phys. Rev. Lett. **124**, 023201 (2020).

[131] K. C. Younge, B. Knuffman, S. E. Anderson, and G. Raithel, "State-Dependent Energy Shifts of Rydberg Atoms in a Ponderomotive Optical Lattice", Phys. Rev. Lett. **104**, 173001 (2010).

[132] R. Loudon, *The quantum theory of light* (OUP Oxford, 2000).

[133] R. W. P. Drever, J. L. Hall, F. V. Kowalski, J. Hough, G. M. Ford, A. J. Munley, and H. Ward, "Laser phase and frequency stabilization using an optical resonator", Applied Physics B **31**, 97–105 (1983).

[134] E. D. Black, "An introduction to Pound–Drever–Hall laser frequency stabilization", American Journal of Physics **69**, 79–87 (2001).

[135] A. Mitra, M. J. Martin, G. W. Biedermann, A. M. Marino, P. M. Poggi, and I. H. Deutsch, "Robust Mølmer-Sørensen gate for neutral atoms using rapid adiabatic Rydberg dressing", Phys. Rev. A **101**, 030301 (2020).

[136] M. Saffman, I. I. Beterov, A. Dalal, E. J. Páez, and B. C. Sanders, "Symmetric Rydberg controlled-z gates with adiabatic pulses", Phys. Rev. A **101**, 062309 (2020).

[137] X. L. Zhang, L. Isenhower, A. T. Gill, T. G. Walker, and M. Saffman, "Deterministic entanglement of two neutral atoms via Rydberg blockade", Phys. Rev. A **82**, 030306 (2010).

[138] S. L. Campbell, R. B. Hutson, G. E. Marti, A. Goban, N. Darkwah Oppong, R. L. McNally, L. Sonderhouse, J. M. Robinson, W. Zhang, B. J. Bloom, and J. Ye, "A fermi-degenerate three-dimensional optical lattice clock", Science **358**, 90–94 (2017).

[139] G. E. Marti, R. B. Hutson, A. Goban, S. L. Campbell, N. Poli, and J. Ye, "Imaging Optical Frequencies with 100 μHz Precision and 1.1 μm Resolution", Phys. Rev. Lett. **120**, 103201 (2018).

[140] Boulder Atomic Clock Optical Network (BACON) Collaboration, "Frequency ratio measurements at 18-digit accuracy using an optical clock network", Nature **591**, 564–569 (2021).

[141] A. D. Ludlow, M. M. Boyd, J. Ye, E. Peik, and P. O. Schmidt, "Optical atomic clocks", Rev. Mod. Phys. **87**, 637–701 (2015).

[142] D. Cohen, "Magnetoencephalography: Detection of the Brain's Electrical Activity with a Superconducting Magnetometer", Science **175**, 664–666 (1972).

[143] L. Rondin, J.-P. Tetienne, T. Hingant, J.-F. Roch, P. Maletinsky, and V. Jacques, "Magnetometry with nitrogen-vacancy defects in diamond", Reports on Progress in Physics **77**, 056503 (2014).

[144] D. Budker and M. Romalis, "Optical magnetometry", Nature Physics **3**, 227–234 (2007).

[145] F. Stopp, “Setup and characterization of a phase-stabilized laser system for coherent manipulation of cold rubidium atoms”, Master thesis (TU Darmstadt, 2014).

[146] N. F. Ramsey, “A Molecular Beam Resonance Method with Separated Oscillating Fields”, Phys. Rev. **78**, 695–699 (1950).

[147] E. L. Hahn, “Spin Echoes”, Phys. Rev. **80**, 580–594 (1950).

[148] S. Kuhr, W. Alt, D. Schrader, I. Dotsenko, Y. Miroshnychenko, A. Rauschenbeutel, and D. Meschede, “Analysis of dephasing mechanisms in a standing-wave dipole trap”, Phys. Rev. A **72**, 023406 (2005).

[149] P. Schauß, “Characterization of Dipole Trap Arrays for Quantum Information Processing with Neutral Atoms”, Master thesis (TU Darmstadt, 2009).

[150] A. Shekhawat and R. O. Ritchie, “Toughness and strength of nanocrystalline graphene”, Nature Communications **7**, 10546 (2016).

[151] S. de Léséleuc, V. Lienhard, P. Scholl, D. Barredo, S. Weber, N. Lang, H. P. Büchler, T. Lahaye, and A. Browaeys, “Observation of a symmetry-protected topological phase of interacting bosons with Rydberg atoms”, Science **365**, 775–780 (2019).

[152] F. Nogrette, H. Labuhn, S. Ravets, D. Barredo, L. Béguin, A. Vernier, T. Lahaye, and A. Browaeys, “Single-Atom Trapping in Holographic 2D Arrays of Microtraps with Arbitrary Geometries”, Phys. Rev. X **4**, 021034 (2014).

[153] N. Holland, D. Stuart, O. Barter, and A. Kuhn, “Benchmarking modern algorithms to holographically create optical tweezers for laser-cooled atoms”, Journal of Modern Optics **65**, 2133–2141 (2018).

[154] L. J. Hornbeck, “From cathode rays to digital micromirrors: A history of electronic projection display technology”, TI Technical Journal, 38 (1998).

[155] D. Schäffner, “Site-Selective Addressing in Dynamically Configurable Dipole Trap Arrays”, Master thesis (TU Darmstadt, 2015).

[156] L. Brozio, “Micromirror-Based Manipulation of Dipole Traps Created by Microlens Arrays”, Master thesis (TU Darmstadt, 2019).

[157] S. Kawata, H.-B. Sun, T. Tanaka, and K. Takada, “Finer features for functional microdevices”, Nature **412**, 697–698 (2001).

[158] T. Gissibl, S. Thiele, A. Herkommer, and H. Giessen, “Two-photon direct laser writing of ultracompact multi-lens objectives”, Nature Photonics **10**, 554–560 (2016).

[159] D. Schäffner, T. Preuschoff, S. Ristok, L. Brozio, M. Schlosser, H. Giessen, and G. Birkl, “Arrays of individually controllable optical tweezers based on 3D-printed microlens arrays”, Opt. Express **28**, 8640–8645 (2020).

[160] J. Fischer and M. Wegener, “Three-dimensional optical laser lithography beyond the diffraction limit”, Laser & Photonics Reviews **7**, 22–44 (2013).

[161] A. Selimis, V. Mironov, and M. Farsari, “Direct laser writing: Principles and materials for scaffold 3D printing”, Microelectronic Engineering **132**, Micro and Nanofabrication Breakthroughs for Electronics, MEMS and Life Sciences, 83–89 (2015).

[162] Y. Li, Y. Yu, L. Guo, S. Wu, C. Chen, L. Niu, A. Li, and H. Yang, “High efficiency multilevel phase-type Fresnel zone plates produced by two-photon polymerization of SU-8”, Journal of Optics **12**, 035203 (2010).

[163] S. Thiele, T. Gissibl, H. Giessen, and A. M. Herkommer, “Ultra-compact on-chip LED collimation optics by 3D femtosecond direct laser writing”, Opt. Lett. **41**, 3029–3032 (2016).

[164] R. L. Sutherland, *Handbook of nonlinear optics* (CRC press, 2003).

[165] C. Yuan, K. Kowsari, S. Panjwani, Z. Chen, D. Wang, B. Zhang, C. J.-X. Ng, P. V. y. Alvarado, and Q. Ge, “Ultrafast Three-Dimensional Printing of Optically Smooth Microlens Arrays by Oscillation-Assisted Digital Light Processing”, ACS Applied Materials & Interfaces **11**, 40662–40668 (2019).

[166] M. Schmid, S. Thiele, A. Herkommer, and H. Giessen, “Three-dimensional direct laser written achromatic axicons and multi-component microlenses”, Opt. Lett. **43**, 5837–5840 (2018).

[167] M. D. Perrin, R. Soummer, E. M. Elliott, M. D. Lallo, and A. Sivaramakrishnan, “Simulating point spread functions for the James Webb Space Telescope with WebbPSF”, Proc. SPIE 8442, Space Telescopes and Instrumentation 2012: Optical, Infrared, and Millimeter Wave **8442**, 1193–1203 (2012).

[168] M. R. Sturm, M. Schlosser, R. Walser, and G. Birkl, “Quantum simulators by design: Many-body physics in reconfigurable arrays of tunnel-coupled traps”, Phys. Rev. A **95**, 063625 (2017).

[169] M. Schlosser, J. Kruse, and G. Birkl, “Synchronization of atomic quantum systems in multi-site optical trapping potentials”, arXiv (2019).

[170] J. Küber, “Dynamics of Bose-Einstein condensates in novel optical potentials”, PhD thesis (TU Darmstadt, 2014).

[171] D. Schäffner, “Micromirror-Based Addressing of Microlens Arrays”, Bachelor thesis (TU Darmstadt, 2013).

[172] X. Wang, Y. Qin, H. Hua, Y.-H. Lee, and S.-T. Wu, “Digitally switchable multi-focal lens using freeform optics”, Opt. Express **26**, 11007–11017 (2018).

[173] M. Schlosser, S. Tichelmann, J. Kruse, and G. Birkl, “Scalable architecture for quantum information processing with atoms in optical micro-structures”, Quantum Information Processing **10**, 907 (2011).

Acknowledgments

Dies ist die Stelle, um Danke zu sagen. Danke an all diejenigen, ohne die diese Arbeit in der vorliegenden Form nicht möglich gewesen wäre. Danke für die großartige Unterstützung, welche ich nicht nur, aber gerade auch in den letzten Monaten, in vielerlei Hinsicht erfahren durfte.
Allen voran möchte ich mich bei meinem Doktorvater Prof. Dr. Gerhard Birkl bedanken für das entgegengebrachte Vertrauen über all die Jahre, die vorzügliche Betreuung, die kontinuierliche Rückmeldung und Abstimmung sowie den Freiraum, viele eigene Ideen ausprobieren und umsetzen zu dürfen.
Ferner möchte ich mich bei Prof. Dr. Thomas Walther für die freundliche Übernahme des Zweitgutachtens bedanken. Mein großer Dank gilt außerdem Prof. Dr. Harald Giessen, für die erfolgreiche Zusammenarbeit im Rahmen der in dieser Arbeit vorgestellten Kooperation.
Die Jahre der Forschung am QUIPS-Experiment waren für mich eine unschätzbar lehrreiche Zeit, mit der Möglichkeit, täglich Quantenphysik hautnah zu erleben. Sie hätten aber lange nicht so viel Freude bereitet und wären auch sicher nicht gleichermaßen erfolgreich gewesen ohne die Arbeit im Team und gegenseitige Unterstützung in der gesamten Arbeitsgruppe. Malte, all die Jahre, seit den Anfängen meiner Tätigkeit in der AG, konnte ich mich immer an dich wenden und du hattest jederzeit ein offenes Ohr. Vielen Dank. Besonders bedanken möchte ich mich bei dir, Daniel. Als mein langjähriger Kollege am Experiment haben wir echt viel erlebt in den unzähligen Stunden im Labor, aber auch abseits der Uni. Ebenso gilt mein Dank Tobias, gerade auch für die großartige Unterstützung in den letzten Monaten. Ich wünsch dir viel Erfolg bei der zukünftigen Arbeit an einem sehr spannenden Experiment!
Des Weiteren möchte ich mich bei euch, Lars und Tilman, bedanken. Ihr habt durch eure Tätigkeit am Experiment selbst und gerade auch durch Weiterentwicklungen unter anderem am Rydberglasersystem das Experiment deutlich vorangebracht. Ich wünsche euch gutes Gelingen bei den nächsten Projekten. An Tilman sowie Simon Ristok geht mein besonderer Dank für die sehr gute Zusammenarbeit hinsichtlich der Entwicklung des hybriden DMD- und 3D-gedrucken Mikrolinsensystem-Aufbaus.
Auch die experimentübergreifende Zusammenarbeit habe ich immer sehr geschätzt und mein Dank gilt hier Felix und Dominik vom ATOMICS-Experiment und Patrick für seine große Hilfsbereitschaft und Unterstützung insbesondere bei Elektronik-Problemstellungen.
Die Entwicklung des Experiments wurde gerade auch durch die engagierte Arbeit vieler Bachelor- und Masterstudenten enorm vorangebracht. Hier möchte ich mich bei Fabian, Lukas, René, Jan-Niklas, Jan, Max, Pascal und Stefan vielmals bedanken. Mein Dank gilt ferner Gabi und Nathalie dafür, dass ich mich bei allen Verwaltungsangelegenheiten und Aufgaben jenseits der Labortätigkeit jederzeit an euch wenden konnte. Ferner danke ich den Teams der Feinmechanik- und Elektronikwerkstatt für die tolle Zusammenarbeit über all die Jahre. Außerdem möchte ich mich bei meiner Familie sowie Freunden für den stetigen Rückhalt während der Arbeit an dieser Dissertation von Herzen bedanken.

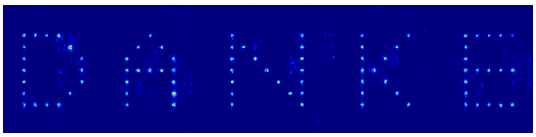

Curriculum Vitae

The CV is not included in the online version for reasons of data protection.

Erklärungen laut Promotionsordnung

§8 Abs. 1 lit. c PromO

Ich versichere hiermit, dass die elektronische Version meiner Dissertation mit der schriftlichen Version übereinstimmt.

§8 Abs. 1 lit. d PromO

Ich versichere hiermit, dass zu einem vorherigen Zeitpunkt noch keine Promotion versucht wurde. In diesem Fall sind nähere Angaben über Zeitpunkt, Hochschule, Dissertationsthema und Ergebnis dieses Versuchs mitzuteilen.

§9 Abs. 1 PromO

Ich versichere hiermit, dass die vorliegende Dissertation selbstständig und nur unter Verwendung der angegebenen Quellen verfasst wurde.

§9 Abs. 2 PromO

Die Arbeit hat bisher noch nicht zu Prüfungszwecken gedient.

Darmstadt, 11. Mai 2021

D. Schäffner